UNIVERSITÀ DEGLI STUDI DI PADOVA

Sede amministrativa: Università degli studi di Padova

Dipartimento di Astronomia

Dottorato di ricerca in Astronomia

CICLO XX

Component separation for all-sky CMB temperature maps

Coordinatore	Prof. G. Piotto
Supervisori	Prof. G. De Zotti Prof. G. Tormen Prof. E. Salerno

Dottorando Anna Valentina Bonaldi

Data consegna Tesi: 31 Gennaio 2008

Contents

Summary

The work described in this Thesis is related to the PLANCK mission, scheduled for launch in 2008, which will observe the microwave sky with unprecedent resolution and sensitivity. The PLANCK collaboration involves hundreds of scientists and profits from the contributions of research groups in many countries. Among them, an Italian collaboration has a key role on component separation. This is a crucial step of the data reduction process, aimed at disentangling the Cosmic Microwave Background (CMB) and all the astrophysical components which are mixed in the nine observational channels of PLANCK. The most important diffuse components are, besides the CMB, synchrotron, free-free and thermal dust emissions due to our own Galaxy. Moreover, the PLANCK maps will contain radio and infrared extragalactic sources as well as the Sunyaev-Zel'dovich effects from clusters of galaxies. All the components which mix with the CMB are referred to as "foregrounds", as they are placed between the CMB and the observer.

The main goal of component separation is to provide a map of the CMB, from which the relevant cosmological information will be derived, clean from foreground contamination. On the other hand, maps of astrophysical components are of great interest per se. The accuracy of the component separation process will ultimately set that of the final results PLANCK will provide.

Our work was mainly focused on the development and testing of a new method for the separation of diffuse foregrounds, the Correlated Component Analysis (CCA), proposed by Bedini et al. (2005). This technique exploits second-order statistics to estimate the "mixing matrix", which contains the frequency behavior of the components mixed in the data. It is necessary to adopt a model for such components, i.e. to parametrize their frequency scaling in a suitable way. Our approach is to estimate the mixing matrix separately in different regions of the sky, where the spectral dependencies of foregrounds can be assumed to be constant. Once the mixing matrix is known, several methods are available to perform component separation, such as Wiener Filtering (WF), Maximum Entropy Method (MEM) or other Bayesian inversion techniques.

After having suitably implemented the CCA method, we tested its performances on simulated PLANCK data. In Bonaldi et al. (2006) we applied the method to different sets of simulated PLANCK channels and estimated the errors on the mixing matrix with a Monte Carlo approach. The simulations included realistic diffuse foregrounds, with spatially varying spectral properties, and Gaussian noise at the nominal level for the PLANCK satellite. This test showed that the method is efficient and that the errors on the mixing ma-

trix estimation produce a minor contribution to the errors on the CMB power spectrum. We then partecipated in a blind comparative test of component separation methods coordinated by the PLANCK working group on "component separation". The test used a more sophisticated simulation of PLANCK data, which included, besides diffuse foreground emissions, also point sources and extragalactic background and a more realistic treatment of the noise. On these data, we tested CCA combined with harmonic Wiener Filtering. We focused on the reconstruction of the CMB map and on the power spectrum estimation, and obtained in both cases very good results, highly competitive with those provided with the best methods developed so far. We also got satisfactory reconstructions of Galactic dust emission, which is the dominant foreground in the highest resolution (high frequency) PLANCK channels.

In Bonaldi et al. (2007b) we tested the same strategy on real data i.e. the first three years of WMAP data. Our results are generally compatible with the result published by the WMAP team. We investigated the presence in the data of the so-called "microwave anomalous emission", an additional foreground component which could dominate in the lowest frequency WMAP channel (23 GHz). This component, revealed by cross correlations of microwave data with IR maps, appears to be correlated with thermal dust emission and has been interpreted as emission due to spinning dust grains (Draine & Lazarian 1998) or, alternatively, as synchrotron emission from dusty active star-forming regions (Hinshaw et al. 2006). We adopted various models for the frequency scaling of such component, whose properties are still poorly known. We then applied several quality tests to the maps reconstructed for each model and selected a subset of models having a good compatibility with the data. We also managed to get the first, albeit preliminary, template of the anomalous emission over about 90% of the sky.

We then estimated how our imperfect knowledge of the foreground components affects the CMB power spectrum. To this end we compared the CMB power spectra obtained adopting different foreground models that passed our quality tests. A significant spread has been found for the largest scales, where anomalies of the WMAP power spectrum compared to the expectations from the best fit cosmological model have been reported. Taking into account modelization errors, we find no large scale power spectrum anomalies significant at $\geq 1.5\sigma$, except for the excess power at $\ell \simeq 40$, which is significant at around the 4σ level.

A minor part of this Thesis was devoted to the study of the Sunyaev-Zel'dovich (SZ) effect, due to inverse Compton scattering of CMB photons by hot electrons in the astrophysical plasmas bound to the cosmic structures. PLANCK is expected to provide a big sample of galaxy clusters observed through the SZ effect. One exploitation of the PLANCK cluster sample is related to the study of the physics of the intra-cluster (IC) gas. In Bonaldi et al. (2007a) we investigated the observable effects of different modeling of the physics of the IC gas. Another research field related to the SZ effect concerns the study of the Large Scale Structure of the Universe. In Dolag et al. (2006) we analysed the SZ emission due to the so-called cosmic web, the network of filamentary structures which is now believed to connect galaxy clusters. The signal is too weak to be

detected but its presence may bias the observed properties of galaxy clusters both in the X-ray band and in the microwaves.

The outline of the Thesis is the following: Chapter 1 summarizes the theory of the CMB fluctuations and their information content. In Chapter 2 we discuss the foreground components. In Chapter 3 we state the component separation problem and we review the main component separation techniques, from the most traditional ones to those recently developed for the PLANCK mission. In Chapter 4 and Chapter 5 we report on the work on the CCA method we performed respectively on simulated PLANCK data and on the WMAP data. Finally, in Chapter 6 we present our conclusions, together with the most recent developments of our work.

8

Sommario

Il lavoro esposto in questa Tesi riguarda la missione PLANCK, il cui lancio è previsto per il 2008, che osserverà il cielo nelle microonde con risoluzione e sensibilità senza precedenti. Alla missione PLANCK collaborano centinaia di scienziati, facenti parte di gruppi di ricerca in molti paesi. Tra di essi, una collaborazione italiana ha un ruolo chiave nella separazione delle componenti. Si tratta di un passo cruciale della riduzione dati, che ha lo scopo di separare il fondo cosmico di microonde (CMB) da tutte le altre componenti astrofisiche che sono presenti nei nove canali osservativi di PLANCK. Le componenti diffuse più importanti sono, a parte il CMB, sincrotrone, free-free ed emissione termica delle polveri dovuti alla nostra Galassia. In aggiunta, le mappe di PLANCK conterranno sorgenti extragalattiche radio ed infrarosse come pure l'effetto Sunyaev-Zel'dovich da ammassi di galassie. Tutte le componenti che si sovrappongono al CMB vengono dette "foregrounds", in quanto si collocano tra l'osservatore ed il fondo cosmico.

Lo scopo principale della separazione delle componenti è fornire una mappa del CMB non contaminata dalla presenza dei foregrounds, da cui derivare tutte le informazioni di carattere cosmologico. D'altra parte, le mappe delle altre componenti astrofisiche sono di grande interesse scientifico di per sè. L'accuratezza del processo di separazione delle componenti costituirà il limite ultimo a quella dei risultati finali che PLANCK fornirà.

In nostro lavoro è incentrato sullo sviluppo ed il test di un nuovo metodo di separazione delle componenti, la Correlated Component Analysis (CCA), proposta da Bedini et al. (2005). Questa tecnica si serve di statistica del secondo ordine per stimare la "matrice di mixing", che contiene il comportamento in frequenza delle componenti presenti nei dati. È necessario adottare un modello per le componenti, ovvero parametrizzare la loro dipendenza dalla frequenza in modo opportuno. Il nostro approccio è di stimare la matrice di mixing separatamente in diverse regioni di cielo, il modo tale da poter assumere costante l'andamento spettrale dei foregrounds. Una volta che la matrice di mixing sia nota, sono disponibili diversi metodi per separare le componenti, come il Wiener Filtering (WF) ed in Maximum Entropy Method (MEM), o altri metodi Bayesiani.

Dopo aver implementato CCA in modo opportuno, l'abbiamo testato su dati simulati di PLANCK. In Bonaldi et al. (2006) abbiamo applicato il metodo a diversi set di canali simulati di PLANCK ed abbiamo stimato gli errori nella stima della matrice di mixing con un approccio Monte Carlo. Le simulazioni includevano foreground diffusi realistici, con proprietà spettrali variabili nel

cielo, e rumore Gaussiano al livello nominale. Questo test ha dimostrato che il metodo è efficiente e che gli errori nella matrice di mixing contribuiscono in modo marginale agli errori sullo spettro del CMB.

Abbiamo quindi partecipato ad un test comparativo cieco di metodi di separazione delle componenti coordinato dal working group di PLANCK sulla separazione delle componenti. Il test utilizzava una simulazione dei dati di PLANCK più sofisticata, che includeva, oltre alle emissioni diffuse, anche le sorgenti puntiformi, il background extragalattico ed una trattazione più realistica del rumore. Abbiamo testato CCA su questi dati in combinazione con filtro di Wiener armonico. Ci siamo concentrati sulla ricostruzione della mappa del CMB e sulla stima dello spettro di potenza, ottenendo in entrambi i casi risultati molto buoni, altamente competitivi con quelli dei migliori metodi sviluppati finora. Abbiamo anche ottenuto risultati soddisfacenti per quanto riguarda la ricostruzione della componente di polvere galattica, che è il foreground dominante nei canali di PLANCK ad alta risoluzione (alta frequenza).

In Bonaldi et al. (2007b) abbiamo testato lo stesso approccio su dati reali, ovvero i primi tre anni di dati della missione WMAP. I nostri risultati sono in generale compatibili con quelli pubblicati dal team di WMAP. Abbiamo indagato la presenza nei dati della cosiddetta "emissione anomala", una ulteriore componente di foreground che potrebbe dominare nel canale di WMAP a frequenza minore (23 GHz). Questa componente, rivelata da cross-correlazioni di dati nelle microonde e mappe infrarosse, è apparentemente correlata con l'emissione da polvere termica ed è stata interpretata come emissione dovuta alla rotazione dei grani di polvere (Draine & Lazarian 1998) o, in alternativa, come emissione di sincrotrone da regioni polverose con formazione stellare attiva (Hinshaw et al. 2006). Abbiamo adottato vari modelli per la dipendenza dalla frequenca di questa componente, le cui proprietà sono ancora poco note. Abbiamo quindi applicato una serie di test di qualità alle mappe ricostruite per ogni modello e selezionato una sottoclasse di modelli aventi una buona compatibilità coi dati. Siamo anche riusciti ad ottenere la prima, ancorché preliminare, mappa della componente anomala su circa il 90% del cielo.

Abbiamo quindi stimato in che modo una imperfetta conoscenza delle componenti di foreground influisca sullo spettro di potenza del CMB. A questo scopo abbiamo confrontato gli spettri di potenza ottenuti adottando diversi modelli di foreground, risultati validi in base ai nostri test di qualità. È risultata una discrepanza significativa fra i diversi modelli alle scale più grandi, dove sono state riscontrate anomalie dello spettro di potenza di WMAP rispetto alle predizioni del modello cosmologico di best fit. Una volta presi in considerazine gli errori di modelizzazione, non si riscontrano anomalie nello spettro di potenza significative più di 1.5σ, ad eccezione di quella ad $\ell \simeq 40$, significativa a 4σ.

Una parte minore della Tesi è stata dedicata allo studio dell'effetto Sunyaev-Zel'dovich (SZ), dovuto a scattering Compton inverso dei fotoni del CMB con elettroni energetici nel plasma astrofisico legato alle strutture cosmiche. Ci si aspetta che PLANCK fornisca un campione ragguardevole di ammassi di galassie osservati in SZ. Uno dei possibili utilizzi di tale campione è legato allo studio della fisica del gas intra-cluster (IC). In Bonaldi et al. (2007a) abbiamo studiato l'effetto osservabile di diversi modelli per la fisica del gas IC. Un altro

campo di ricerca legato all'effetto SZ riguarda lo studio della struttura a grande scala dell'Universo. In Dolag et al. (2006) abbiamo analizzato l'emissione SZ dovuta alla cosiddetta "ragnatela cosmica", la rete di strutture filamentari che connettono gli ammassi di galassie come mostrato dalle simulazioni numeriche. Il segnale è troppo debole per essere misurato, ma la sua presenza può costituire un bias per le proprietà osservative degli ammassi di galassie sia nell'X che nelle microonde.

Lo schema della Tesi è il seguente: il Capitolo 1 riassume la teoria delle fluttuazioni del fondo cosmico ed il loro contenuto informativo. Nel Capitolo 2 discutiamo le componenti di foreground. Nel Capitolo 3 definiamo il problema della separazione delle componenti e facciamo una panoramica delle principali tecniche, dalle più tradizionale a quelle sviluppate recentemente per la missione PLANCK. Nel Capitolo 4 e nel Capitolo 5 descriviamo il lavoro su CCA svolto rispettivamente su dati simulati di PLANCK e su dati WMAP. Infine, il Capitolo 6 contiene le nostre conclusioni, insieme agli sviluppi più recenti del nostro lavoro.

Chapter 1

CMB theory

1.1 Introduction

For over forty years, observations of the Cosmic Microwave Background (CMB) have had a profound influence on our knowledge of the Universe. The discovery of the CMB in 1965 established beyond reasonable doubt the paradigm of Hot Big Bang cosmology and provided firm observational evidence for an evolving Universe. The discovery of the CMB also provided the first link between particle physics and cosmology, namely the theory of Big Bang nucleosynthesis. The discovery of the CMB also has important implications for fundamental physics. According to General Relativity, a singularity at early times was unavoidable. Evidently, classical General Relativity must break down at the Hot Big Bang, but in this case there is a real possibility of finding observational signatures of quantum cosmology and of learning about entirely new physics.

After the discovery of the CMB, cosmologists realized that the fluctuations in the early universe responsible for the structures that we see today (galaxies, clusters and superclusters) must have imprinted small differences in the temperature of the CMB (anisotropies) coming from different directions of the sky. A long series of experiments searched for these tiny variations (of order one thousandths percent of the CMB temperature). They were finally discovered with the NASA's Cosmic Background Explorer (COBE), and this has opened a new way of studying the early Universe. CMB anisotropies can be used to determine the values of many of the key parameters that define our Universe, in particular its geometry, age, and composition. Following COBE, a remarkable series of experiments culminating with the NASA's Wilkinson Microwave Anisotropy Probe (WMAP) established that our Universe is very close to being flat. Furthermore, these experiments have provided compelling evidence that our Universe is dominated by dark energy and dark matter, and that present-day structures grew from nearly scale invariant primordial fluctuations. Nevertheless, much more information about the Universe remains to be extracted from the CMB, especially from its polarization. For this reason, other experiments are planned, first of all ESA's PLANCK satellite, whose launch is scheduled for 2008.

1.2 Statistics of the CMB

The basic observable of the CMB is its intensity as a function of frequency and direction on the sky (θ, ϕ). Because the CMB spectrum is an extremely accurate blackbody, with a nearly constant temperature across the sky T, this observable is usually described in terms of its temperature fluctuations, or anisotropies, $\Delta T/T$. The temperature anisotropies of the sky can be expanded in spherical harmonics,

$$\Delta T = \sum_{\ell m} a_{\ell m} Y_{\ell m}(\theta, \phi). \tag{1.1}$$

According to the inflationary models, which are the current reference ones, the temperature anisotropies should obey Gaussian statistics to high accuracy. If this is the case, then all the statistical properties of the temperature anisotropies can be computed from a single function of multipole ℓ, the temperature power spectrum

$$C_\ell = \langle |a_{\ell m}|^2 \rangle. \tag{1.2}$$

The electron-photon coupling in the cosmological plasma in the relevant epochs is ensured by Thomson scattering which produces linear polarization. This gives two other measurable quantities, the Stokes parameters Q and U, over all the sky. The Q and U parameters form the components of a second rank, symmetric and trace-free linear polarization tensor P_{ab}. In general, the polarization tensor can be expanded in terms of two scalar fields P_E and P_B, the electric (or gradient) and magnetic (or curl) polarization respectively. The decomposition is unique on the full sphere and is analogous to the decomposition of a vector field into a gradient and a divergence-free vector. The decomposition into spherical harmonics is:

$$P_E = \sum_{\ell \geq 2} \sum_{|m| \leq \ell} \sqrt{\frac{(\ell-2)!}{(\ell+2)!}} a^E_{\ell m} Y_{\ell m} \tag{1.3}$$

$$P_B = \sum_{\ell \geq 2} \sum_{|m| \leq \ell} \sqrt{\frac{(\ell-2)!}{(\ell+2)!}} a^B_{\ell m} Y_{\ell m}, \tag{1.4}$$

which defines the E and B multipole coefficients, $a^E_{\ell m}$ and $a^B_{\ell m}$ respectively, analogous to $a_{\ell m}$ introduced for the total intensity. Then, we can in general define the power spectrum C^{XY}_ℓ, where X and Y can be either T, E or B, as:

$$C^{XY}_\ell = \langle a^X_{\ell m} a^{*Y}_{\ell m} \rangle. \tag{1.5}$$

If the initial fluctuations are Gaussian, the temperature and polarization anisotropies can be described completely by four power spectra: using the notation $C^X_\ell \equiv C^{XX}_\ell$ these are C^T, C^E, C^B and C^{TE}. These spectra are thus related to temperature, polarization E and B modes, and temperature-polarization cross correlation, the other correlations being equal to zero.

1.3 CMB primary anisotropies

In the standard Hot Big Bang model, the primordial Universe is fully ionized. Photons are tightly coupled to electrons by the Thomson scattering, so that matter and radiation constitute a single fluid, which cools as the expansion of the Universe proceeds. When the Universe reached a temperature around 3000 K, electrons and ions combined to form hydrogen atoms. This is the so-called recombination epoch, at a redshift $z \sim 1000$. Once the recombination was complete the Universe became transparent to radiation and the photons propagated towards us along geodesics. Maps of the microwave background radiation therefore provide us a picture of the Universe at the "last scattering surface" (LSS). These are the so-called primary CMB anisotropies, which can be explained completely by analyzing the behavior of this prerecombination fluid. In particular, their properties depend on the initial conditions, i.e. on the physical mechanism that generated the primordial small perturbations, and on the energy contents of the Universe before recombination. There are also several mechanisms which generate anisotropies after the recombination epoch: these are the secondary anisotropies, which will be discussed in the next section.

1.3.1 Primordial perturbations

Initial or primordial perturbations are defined deep in the radiation era but typically after nucleosynthesis, so that the main cosmological components reduce to the usual photons, baryons, neutrinos and dark matter. The above various cosmological species can be characterized by their number density, n_X, and their energy density ρ_X. Linear perturbations of these quantities are defined as

$$\delta n_X = n_X - \bar{n}_X, \quad \delta\rho_X = \rho_X - \bar{\rho}_X, \tag{1.6}$$

where the bar corresponds to the homogeneous (unperturbed) quantity. An initial density perturbation may be decomposed into a sum of an adiabatic and an isocurvature perturbation. The adiabatic mode is defined as a perturbation affecting all the cosmological species such that the relative ratios in the number densities remain unperturbed, i.e, such that

$$\delta(n_X/n_\gamma) = 0. \tag{1.7}$$

It is associated with a curvature perturbation, via Einstein's equations. In terms of the energy density contrast, defined by $\delta\rho/\rho$, the adiabatic perturbation is characterized by the relation

$$\frac{\Delta T}{T} = \frac{1}{4}\frac{\delta\rho_\gamma}{\rho_\gamma} = \frac{1}{3}\frac{\delta\rho}{\rho}. \tag{1.8}$$

Isocurvature perturbations are characterized by the fact that the total energy density is conserved, as matter perturbations compensate those of radiation.

For an admixture of an adiabatic and a single isocurvature mode, the power spectrum of the CMB anisotropies can be written as:

$$C_\ell = (1-\alpha)C_\ell^{ad} + \alpha C_\ell^{iso} + 2\beta\sqrt{\alpha(1-\alpha)C_\ell^{corr}}, \tag{1.9}$$

where C_ℓ^{ad} and C_ℓ^{iso} are the power spectra of the adiabatic and isocurvature modes and C_ℓ^{corr} is the power spectrum of their cross-correlation (e.g., Amendola et al. 2002). The spectra C_ℓ^{ad} and C_ℓ^{iso} have very distinctive features, and this can be used to estimate the importance of their contribution to the total spectrum C_ℓ. The relative amplitude of the two modes and their correlation depend on the model, for example on the initial conditions which generated the anisotropies, as we will discuss in the next section. The observed CMB is compatible with an initial perturbation which is at least mainly adiabatic. As adiabatic perturbations are naturally generated by an inflationary period, all these observations gave strong support to the inflationary models. However, this does not exclude the presence of a sub-dominant isocurvature contribution, which could be detected in future with high precision experiments such as PLANCK.

1.3.2 Initial conditions: the inflationary theory

The name inflation refers to a phase of rapid (exponential) expansion undergone by the early Universe. According to the usual Friedman equation for the evolution of the cosmological factor, this phase is possible if the early Universe went through a period with equation of state $p = -\rho$, where p and ρ are the pressure and mean density of the Universe respectively. During inflation, regions which were in causal contact can be inflated in scale by many orders of magnitude.

An early period of inflation offers solutions to many fundamental problems (Guth 1981). First of all, it explains why the CMB is statistically uniform on scale larger than about one degree, which is the distance that light could have traveled from the Big Bang to the recombination epoch, and thus the maximum dimension which could have been in causal contact. It can also explain why our Universe is nearly spatially flat without the need of fine-tuning. Moreover, inflation also offers an explanation for the origin of fluctuations.

Single-field inflation

In the simplest inflationary models, the accelerated expansion is driven by a single scalar field, ϕ, sometimes known as the inflaton. Its energy and pressure are given by:

$$\rho = \frac{1}{2}\dot{\phi}^2 + V(\phi) \tag{1.10}$$

$$p = \frac{1}{2}\dot{\phi}^2 - V(\phi), \tag{1.11}$$

where $V(\phi)$ is the potential of the scalar field ϕ. Thus, if the field evolves slowly (slow-roll conditions, $\dot{\phi} \ll V(\phi)$), then $p \simeq -\rho$ and the inflationary phase is possible.

Any scalar field would have quantum fluctuations $\delta\phi$ which would oscillate while the physical size of the fluctuation is smaller than the Hubble radius ct. Because an exponential expansion is self-similar in time, the fluctuations are scale-invariant, i.e. the contribution to the variance of fluctuations is equal in

each logarithmic interval in scale. During the inflationary phase, fluctuations are increased in scale to sizes many orders of magnitude larger than the Hubble radius. Over that radius, they become classical perturbations described by General Relativity rather than by quantum field theory.

According to these ideas, all the anisotropies originated as quantum fluctuations in the very early Universe. In particular, fluctuations in the inflaton scalar field turns into temperature fluctuations via the intermediacy of gravity. Because the scalar field carries the energy density of the Universe during the inflation, its fluctuations induce variations in the spatial curvature, Φ, and in the Newtonian potential, Ψ. It is approximatively $\Psi \approx -\Phi$. This results in density and, thus, temperature perturbations of the adiabatic type.

Some alternative models

The one we just described is called single-field inflation, which generates exclusively adiabatic perturbations. However, multiple-field inflation is also possible, which involves more than one scalar field. Multiple-field inflation can generate, in addition to the dominant adiabatic component, an isocurvature contribution.

Another scenario related to isocurvature perturbations which has been recently explored is the curvaton scenario. It is based on the fact that a pure isocurvature primordial perturbation can be converted in an adiabatic perturbation at later times. The curvaton is a scalar field that is very light during inflation and acquires Gaussian fluctuations, which will give isocurvature fluctuations. If the curvaton decays sufficiently late, isocurvature perturbations are transformed into adiabatic ones. In the simplest version, the curvaton perturbations are totally converted into adiabatic perturbations. One can, however, have scenarios where an isocurvature component adds to the adiabatic one. If this is the case the adiabatic and isocurvature perturbations are fully correlated (or anti-correlated) since they are produced by the same field.

The detection of an isocurvature component in the primordial fluctuations thus can help to constraint which of the above scenarios is responsible for the initial perturbations. Another observable useful to this respect is the presence of non-Gaussianities in the primordial perturbation. In fact, such non-Gaussianities are generated in some multi-field inflation models as well as in the curvaton scenario, in contrast with single-field inflation.

1.3.3 Acoustic oscillations

In the previous section we discussed the initial conditions that generated the CMB anisotropies. As we will see, anisotropies on scales $\theta > 1^\circ$ are mainly unaffected by subsequent evolution, so they directly probe the initial conditions. This is often called the Sachs-Wolfe effect (Sachs & Wolfe 1967); temperature anisotropies are proportional to the fluctuations of Gravitational potential along the line if sight:

$$\Theta \equiv \frac{\Delta T}{T_0} \simeq \frac{1}{3}\frac{\Delta \Psi}{c^2}. \tag{1.12}$$

On scales smaller than one degree, the matter-radiation fluid oscillates like

sound waves, causally connecting small scale fluctuations. This mechanism is responsible for the generation of a distinctive feature in the CMB power spectrum, the acoustic peaks, which retain information of the geometry and the matter content of the Universe.

To discuss the formation and the dynamics of the acoustic oscillation, we start with an idealization of a perfect photon-baryon fluid, where we initially neglect the dynamical effects of gravity and of the baryons. Temperature perturbations in Fourier space for the wave number k obey

$$\dot{\Theta} = -\frac{1}{3}kv_\gamma, \tag{1.13}$$

where the dot indicates the first derivative with respect to the conformal time $\eta \equiv \int dt/a(t)$, and v_γ is the photon fluid velocity. The Euler equation is

$$\dot{v}_\gamma = k\Theta. \tag{1.14}$$

Differentiating eq. (1.13) and inserting in eq. (1.14) yields the most basic form of the oscillator equation

$$\ddot{\Theta} + c_s^2 k^2 \Theta = 0, \tag{1.15}$$

where $c_s \equiv \sqrt{\dot{p}/\dot{\rho}} = 1/\sqrt{3}$ is the sound speed in the dynamically baryon-free fluid. This equation says that pressure gradients act as a restoring force to any initial perturbation in the system, which thereafter oscillates at the speed of sound. Physically these temperature oscillations represent the heating and cooling of a fluid that is compressed and rarefied by an acoustic wave. This behavior continues until recombination. Assuming negligible initial velocity perturbations, we have a temperature distribution at recombination of

$$\Theta_{rec} = \Theta_0 \cos(ks_{rec}), \tag{1.16}$$

where $s_{rec} = \int c_s d\eta_{rec} \approx \eta_{rec}/\sqrt{3}$ is the distance that sound can travel by the recombination usually called the sound horizon at recombination. Thus, the maximum distance that can be traveled by a sound wave by the time of recombination is the characteristic scale of the oscillation. For scales having bigger dimension the oscillations had no time to propagate: the perturbation is frozen into its initial conditions. Modes that are caught at maxima or minima of their oscillation at recombination correspond to peaks in the power spectrum, i.e., the variance of $\Theta_{rek}(k)$. Modes corresponding to peaks follow an harmonic relationship $k_n = n\pi/s_{rec}$ with n integer.

Today, a spatial inhomogeneity in the CMB temperature of wavelength λ appears as angular anisotropy of scale $\theta \approx \lambda/D$, where $D(z)$ is the comoving angular diameter distance from the observer to redshift z. Thus, the actual angular size of fluctuations both depends on the linear scale of the perturbation and our distance to the LSS, which depends on the curvature of the Universe. In a flat, matter-dominated universe $\theta \approx 2^\circ$ or, equivalently, $\ell \approx 200$. In a closed universe the angle subtended to the same linear dimension would be bigger (lower ℓ), in an open universe it would be smaller (higher ℓ). The fact that

first acoustic peak is located at $\ell \approx 200$ indicates that the geometry is nearly spatially flat, as predicted by inflationary models.

So far we neglected the effect of gravity in the photon-baryon fluid. However, the Newtonian potential Ψ and the spatial curvature Φ alter the acoustic oscillations by providing a gravitational force on the oscillator. The oscillator eq. (1.15) becomes

$$\ddot{\Theta} + c_s^2 k^2 \Theta = -\frac{k^2}{3}\Psi - \ddot{\Phi}. \tag{1.17}$$

In a flat universe and in the absence of pressure Ψ and Φ are constant. Also, in the absence of baryons, $c_s^2 = 1/3$, so the new oscillator is identical to eq. (1.15) with Θ replaced by $\Theta + \Phi$. This quantity thus can be thought as an effective temperature, which actually corresponds to the observed temperature fluctuations. The solution in the matter-dominated epoch is:

$$[\theta + \Psi](\eta) = [\theta + \Psi](\eta_{md})\cos(ks) = \frac{1}{3}\Psi(\eta_{md})\cos(ks), \tag{1.18}$$

where η_{md} represents the start of the matter-dominated epoch. We note that this solution under the large scale limit corresponds to the Sachs-Wolfe result [eq. (1.12)].

We now want to include also the effect of baryons on the dynamics of the acoustic oscillations. The effect of baryons is to provide extra inertia in the joint Euler equation for pressure and potential gradients to overcome. All terms in the Euler equation except the pressure gradient are multiplied by $1 + R$, where R is the photon-baryon momentum density ratio $R = (p_b + \rho_b)/(p_\gamma + \rho_\gamma)$.The oscillator equation becomes (Hu & Sugiyama 1995):

$$K c_s^2 \frac{d}{d\eta}(c_s^{-2}\dot{\Theta}) + c_s^2 k^2 \Theta = -\frac{k^2}{3}\Psi - c_s^2 \frac{d}{d\eta}(c_s^{-2}\dot{\Phi}) \tag{1.19}$$

where we have used the fact that the sound speed is reduced by the baryons to $c_s = 1/\sqrt{3(1+R)}$. If R, Φ and Ψ are constant, then the equation can be again put in the form of eq. (1.15) with $\Theta \to \Theta + (1+R)\Psi$. Thus, aside from the lowering of the sound speed, baryons have two distinguishable effects: they enhance the amplitude of the oscillations and shift the equilibrium point to $\theta = -(1+R)\Psi$. Because it is still the effective temperature $\theta+\Psi$ that is observed, the zero-point shift breaks the symmetry of the oscillations. The baryons enhance only the compressional phase, i.e., even peaks of the power spectrum. Physically, the extra gravity provided by the baryons enhances compression into potential wells.

1.3.4 The smallest scales: damping and diffusion

At the smallest scales, the acoustic oscillations are progressively suppressed by different phenomena, causing an exponential damping in the power spectrum. The two main effects responsible for damping are both due to the fact that the recombination is not an istantaneous process. In fact, the ionization fraction decreases progressively, thus increasing the mean free path of the electrons.

In other words, the Last Scattering Surface has a finite thickness, which is around 100 in redshift. This dimension provides the characteristic scale for the considered effects ($\ell \sim 2500$) and is sensitive to the baryon content and the thermal history of the Universe.

The first effect is called photon diffusion or Silk damping (Silk 1968): while random walking through the baryons, the photons destroy the perturbations having size smaller than their mean free path. The second effect is due to the fact that along any given line of sight we see a time average of the fluctuations through the recombination process. Thus, on scales smaller than the thickness of the LSS we have many hot and cold perturbations, which statistically tend to cancel once averaged.

There is a final effect concurring to damping, which is related to the amount and nature of the Hot Dark Matter (HDM) in the Universe. It is now established that dark matter, the principal matter constituent of the Universe, is mainly non-baryonic and cold (the hot/cold classification depending on the velocity dispersion of the particle being close to relativistic or not at the epoch of equal densities of matter and radiation). Nevertheless, HDM, whose candidate particle is massive neutrino, could be present in a sub-dominant fraction. The presence of such component can be probed through its damping effect on the CMB anisotropies. In fact, free streaming associated with a non-zero neutrino mass suppresses the amplitude of the matter fluctuations at wavenumber greater than $k \sim 0.03(m_\nu/eV)\Omega_m^{1/2} hMpc^{-1}$ (Bond et al. 1980, Doroskevich et al. 1980).

1.4 Secondary anisotropies

After the LSS, the mean free path of CMB photons is high, so they mostly reach unimpeded the observer. Nevertheless, some of them have further interactions with matter while they travel from the LSS to us: this imprints the so-called secondary anisotropies. Secondary anisotropies are often non-Gaussian, so they do not only show up in the power spectrum, but in higher point correlation functions as well. Secondary anisotropies are mainly caused by gravitational effects and scattering processes.

1.4.1 Integrated Sachs-Wolfe effect

As photons propagate to the observer, they keep passing fluctuations in the gravitational potential. If the potential remains static on time scales comparable to the time the photons require to cross the fluctuation, the blueshift acquired running into the potential well is canceled by the redshift acquired climbing out, and no effect remains. Conversely, traveling through an evolving potential, CMB photons can experience a cumulative change in energy

$$\frac{\delta T}{T} = 2 \int \frac{\dot{\phi}}{c^2} \frac{dl}{c}. \tag{1.20}$$

This is called late, or integrated, Sachs-Wolfe (ISW) effect, and which can contribute significantly to the CMB fluctuations on large angular scales. In gen-

eral this effect depends on the cosmological model, which affects the evolution of the gravitational potential at late stages of structure formation. Current measurements of high-redshift supernovae suggest that the Universe is undergoing a period of accelerated expansion, supporting the notion of a non-zero cosmological constant. In such models, the ISW effect is confined to angular scales of order ten degrees and larger. Since part of the observed anisotropy is associated with the gravitational potential at low redshifts, it must be at least in part correlated with the matter distribution in our vicinity. One may therefore attempt to disentangle the ISW effect from other sources of CMB anisotropy by cross-correlating the CMB emission maps with those tracing the large-scale matter distribution. Such cross-correlation techniques have previously been applied to COBE-DMR and various extragalactic data sets (Aghanim et al. 2007).

1.4.2 Rees-Sciama effect

The Rees-Sciama effect is usually associated to the non-linear contribution to the late Sachs-Wolfe effect. It is caused by time-dependent gravitational potential during the non-linear stages of evolution (Rees & Sciama 1968, Seliak 1996). The amplitude of the Rees-Sciama fluctuations peaks at $\ell \sim 100 - 300$, where it gives $\Delta T/T \sim 10^{-6} - 10^{-7}$ for a wide range of models.

1.4.3 Gravitational waves

Imprints in the temperature anisotropy are also left by a time-variable tensor metric perturbation, which can be viewed as a standing gravitational wave (Sachs & Wolfe 1967). Inflation predicts nearly scale-invariant spectrum of gravitational waves, whose energy depends strongly on the energy scale of inflation and whose relationship to the curvature fluctuations discriminates between inflationary models. Gravitational waves mainly produce a quadrupolar distortion in the CMB temperature distribution (Polnarev 1985). Thus, the contribution to the power spectrum is enhanced at $\ell = 2$ and sharply suppressed at multipole larger than that of the first peak.

1.4.4 Gravitational lensing

While CMB photons propagate towards us, they can be deflected by the presence of matter distributions. Light deflection itself is not an observable effect. Thus, any lensing effect on the CMB is caused by differential deflections: light paths starting in neighboring directions which experience slightly different deflections. The deflection angle due to gravitational lensing can be expressed as the gradient of the Newtonian potential of the lensing matter perturbations. Differential deflection is therefore determined by second derivatives of the potential, which can be related by Poisson's equations to the density contrast of the matter perturbations, projected along the line of sight.

A significative lensing signal is due to virialized cosmic structures, as galaxy clusters, but there is also an important contribution from large scale matter distributions. The effects of lensing is essentially a redistribution of power in the CMB which leads to a creation of fluctuations on angular scales where the

amplitude of the primordial CMB is well suppressed by damping. The lensed CMB should therefore exhibit structure on scales where the primordial CMB would otherwise be featureless (Cole & Efstathiou 1989, Metcalf & Silk 1997). The effect of lensing on the polarization of the CMB is to mix E-type modes with B-type modes. Finally, as we will discuss in the following, the lensed CMB exhibits deviations from Gaussian statistics which are characteristic for the late stages of structure growth.

1.4.5 Reionization

Some time between the epoch of recombination and $z \sim 6$, when quasar spectra show that intergalactic hydrogen is highly ionized, the Universe must have undergone a reionization process. As a consequence, some CMB photons must have suffered Thomson scattering as they traveled from the LSS to us. In addition, the anisotropy of Thomson scattering means that the CMB polarization must have been affected as well. Therefore, a detailed knowledge of the ionization history of the Universe is crucial for the interpretation of the power spectrum in terms of cosmological parameters. Reionization is a highly complicated and poorly understood process, related to the UV light emitted by massive stars and active galactic nuclei hosted by the first cosmic structures.

Reionization mainly suppresses the amplitude of the acoustic peaks by the fractions of photons rescattered, approximatively the optical depth τ. The effect of the optical depth is degenerate with that of other parameters, however polarization measurements can give a reasonably accurate estimate of τ, as we will discuss in the following section.

1.4.6 Vishniac effect

The Vishniac Effect is a small scale secondary anisotropy which arises as a result of Doppler shifting after reionization. In particular, a photon scattering off a free electron with peculiar velocity away from the observer will be slightly redshifted. Conversely, a photon scattering off a free electron with peculiar velocity toward the observer will be slightly blueshifted. Since the length scale of density fluctuations is typically small compared to the size of the visible universe, photons will cross many density perturbations between the surface of last scattering and us. Over the great distance that the photons travel towards the observer the Doppler shift tends to cancel. In particular, the first-order terms vanish. However, there is a second-order term, given by the product of velocity and density fluctuation, which can be non-null. This happens when the peculiar velocity of a bulk flow lies along the line of sight, but its density fluctuation is oriented perpendicular to the line of sight. This second order Doppler shifting is called the Vishniac effect.

1.4.7 Thermal Sunyaev-Zel'dovich effect

The thermal Sunyaev-Zel'dovich effect (SZ, Sunyaev & Zel'dovich 1972) arise whenever the CMB photons travel across a concentration of hot plasma. Some of the photons are scattered off the hot electrons, which are by orders of magnitude

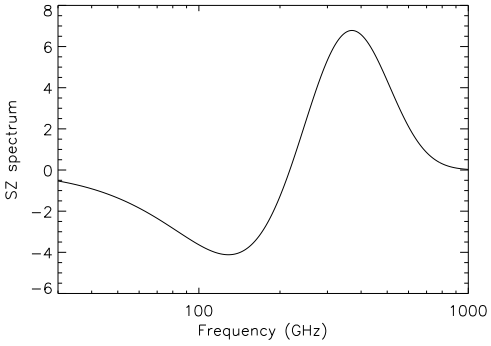

Figure 1.1: frequency dependence of the thermal SZ effect

more energetic than the photons. The latter ones are therefore inverse Compton scattered to higher energies. The SZ effect has the important property of being independent on the redshift of the plasma concentration. The intensity of the interaction is given by the Compton-y parameter:

$$y = \frac{kT_e}{m_e c^2} \sigma_T \int n_e dl, \tag{1.21}$$

where k is the Planck constant, σ_T the Thomson cross-section, and T_e, m_e, n_e the electron temperature, rest mass and number density respectively. Thus, the y parameter is proportional to the electron pressure of the hot medium integrated along the line of sight.

Another important characteristic of the SZ effect is that it has a typical spectral signature, which allows us to identify this signal among others. In absence of relativistic effects - i.e. when the thermal energy of the electrons is negligible compared to the electron rest mass - the spectral shape of the SZ effect is given by the function shown in Fig. 1.1. For frequencies lower than 217 GHz the photon density is decreased as they move to higher frequencies. For a very hot plasma, a small number of electrons reach relativistic energies, which slightly modify the SZ spectrum.

Since Compton scattering is anisotropic, unpolarized infalling radiation can acquire a net linear polarization, so the SZ effect also modifies the polarization patterns of the CMB.

As already theorized by Sunyaev & Zel'dovich, the main responsible for SZ signal in the sky are galaxy clusters. These are the most massive virialized objects in the Universe, and their dark matter potential well contains, besides hundreds of galaxies, hot IC medium ($T_e \sim 10^8$ K) which is highly ionized. Typically the thermal SZ effect from galaxy clusters is of the order of a few mK on arcminute size, and should provide the most substantial contribution to temperature anisotropies beyond the damping tail.

Given the peculiar spectral signature a multifrequency experiment should be able to separate the thermal SZ from primary CMB maps to good accuracy. For this reason, thermal SZ effect can be treated as a foreground component, i.e. a signal superimposed to the CMB which must be extracted in order to

analyze both components separately. We will come back to this subject in the next Chapter, where foreground components are discussed.

1.4.8 Kinetic Sunyaev-Zel'dovich effect

Another effect discovered by Sunyaev & Zel'dovich, weaker compared to thermal SZ, is the kinetic SZ effect. It is caused by the relative motion of clusters with respect to the rest frame of the CMB. This motion imparts a Doppler effect on the CMB photons and thus leads to an energy shift in the photon spectrum. The amplitude of the distortion is proportional to the factor v/c, where v is the peculiar velocity of the object and c the speed of light. Typical peculiar cluster velocities are of order of a few hundred kms^{-1}, so the relative frequency shift is of order of 10^{-4}.

1.5 CMB power spectra

In the above sections we discussed the main mechanisms which generate CMB anisotropies. Now we review the main results in terms of measurable features in the CMB power spectra. This would give an idea of how in practice the measured CMB temperature and polarization power spectra can be exploited to derive the cosmological parameters. As we will see, very different processes may act on the same angular scales, in particular the effects of primary anisotropies mix with those of secondary anisotropies, so that the understanding of the early Universe becomes connected to that of complex late-time physics.

1.5.1 Temperature

By now, the temperature power spectrum is the only one which has been accurately measured at least on certain angular scales. It is usually described in terms of

$$\Delta T_\ell = \sqrt{\frac{\ell(\ell+1)}{2\pi} C_\ell}. \tag{1.22}$$

In this form, it exhibits a flat behavior at low multipoles and a series of oscillations, the acoustic peaks, starting from $\ell \sim 200$, which corresponds to an angular scale around 1 degree. As mentioned above, the position of the first acoustic peak corresponds to the physical scale of the sound horizon at the recombination epoch. In fact, fluctuations in the radiation-matter fluid having dimension smaller than the horizon ($\ell > 200$) oscillate like sound waves, while for those having bigger dimension ($\ell < 200$) the oscillations had no time to propagate. Thus, the accurate measurement of the position of the first acoustic peak, linking physical distance to angular separation on the sky, allows us to measure the curvature of the Universe.

In general, position and amplitude of the acoustic peaks contain a lot of cosmological information. First of all, the presence of the oscillations depends on the mode of perturbations. As we mentioned in § 1.3.1, the CMB proves that the perturbations are (at least mainly) adiabatic, thus giving another important confirmation to the inflationary model. The simplest single-field models of

inflation predict the primordial perturbations to be strictly adiabatic. However, multiple scalar field inflationary models generically lead to a mixture of adiabatic and isocurvature perturbations. Thus, revealing a component of entropy perturbation would be a test for inflationary models.

As explained in § 1.3.3, the dynamics of the acoustic oscillations depends on the gravity of dark matter, which opposes to the radiation pressure maintaining the oscillation, and on the baryon content, which contributes to the potential well during compression phases. Dark matter density and baryon density thus have an effect on the height of the acoustic peaks. The effects are different in the two cases: while DM enhances all the peaks, baryons enhance only even peaks. Thus, the cosmic densities of dark matter and baryons can be constrained by measuring several (at least three) peaks.

The power spectrum at scales bigger than the horizon is due to the Sachs-Wolfe effect (SW), which measures the interaction between photons and the gravitational field and allows to directly constraint the initial conditions. Also the late ISW is present, which causes a rising of the power depending on the value of the cosmological constant.

On small angular scales the spectrum is determined by the damping effects, due to the thickness of the LSS ($\Delta z \simeq 100$). Damping can be thought as the result of the random walk in the baryons that takes photons from hot regions into cold ones and vice versa (Silk 1968). Detailed numerical integration of the equations of motions are required to track the rapid growth of the mean free path and damping length through recombination itself. These calculations show that damping leads to a substantial suppression of the oscillations beyond the third acoustic peak. This suppression depends on the cosmological parameters, in particular Ω_m and Ω_b. More matter density translates in more damping at a fixed multipole moment and in slightly less damping at a fixed peak number. The dependence on baryons is controlled by the free electron density. The net result under Saha approximation is that the damping length scales approximately as $(\Omega_b h^2)^{-1/4}$ (see Hu & White 1997 for an accurate fitting).

Beyond the damping tail, the primary CMB is featureless; however, fluctuations can be present, due to secondary anisotropies active at the smallest scales. The most important effects that can be probed are SZ effect and gravitational lensing.

1.5.2 Polarization

The polarization power spectra contain information which are to some extent complementary to those encoded in the temperature power spectrum. Cosmologically, the CMB polarization can be only due to Thomson scattering, active only before the recombination epoch and after the reionization of the Universe. This is a clear advantage with respect to total intensity, whose anisotropies may be generated at any moment from recombination to the present epoch, thus leading to the superposition of many effects which can be difficult to disentangle. This advantage is however balanced by the fact that the polarized signal is very weak, at least one order of magnitude lower than the temperature one. Since in this Thesis we will only deal with temperature data we will only briefly

mention the characteristics of the polarization power spectra.

The information on the LSS is encoded in the peaks of the polarization power spectra. Their position depend on the horizon scale at the recombination and their amplitude on the thickness of the LSS. The information on the reionization is contained in the spectrum at large scales: a peak is present whose position depend on the redshift of reionization and whose amplitude depends on the optical depth for Thomson scattering during the reionization.

Another important diagnostic instrument related to polarization is the relative intensity of the polarization modes. In fact E-modes and total intensity T are activated by all the cosmological perturbations, while B-modes only depend on vectorial and tensorial perturbations. In particular, the intensity of B-modes compared to the others allow to measure the contribution of gravitational waves, which depends on the potential of the inflation.

1.5.3 Cosmic variance and parameter degeneracies

So far we described the potentialities of the CMB to constrain cosmological parameters through the measurement of its temperature and polarization power spectra. Before proceeding with the description of the results achieved so far and of the goals of the forthcoming CMB experiments, however, we have to mention two important factors which constitute an intrinsic limit to what can be done with CMB data alone: cosmic variance and parameter degeneracies.

Cosmic variance is due to the fact that we only have one realization of Universe to observe, so it is difficult to make statistical statements about cosmology on the scale of the entire Universe. The statistics of small scale fluctuations over all the sky is rich, so the power spectrum at high multipoles is safely representative of the underlying cosmological model. However, the sampling of large scales is poor, so that the actual realization can differ from the model prediction just because of poor statistics. In other words, for each multipole we measure the expectation value of the power spectrum on a certain number of samples, which is small at large scales and big at small scales. Since the power spectrum is a quadratic quantity, it follows a χ^2 distribution, and we can thus exactly compute to which confidence we can measure each point given the number of samples we have. The resulting cosmic variance term (Knox 1995) is:

$$\Delta C_\ell = \sqrt{\frac{2C_\ell}{2\ell(\ell+1)Lf_{sky}}} \tag{1.23}$$

where f_{sky} is the fraction of the sky analysed and L is the width of the bin eventually adopted in ℓ. From this relation it is clear that the cosmic variance error increases as a smaller region of the sky is analysed.

Parameter degeneracies are due to the fact that models with different parameter sets can have nearly identical power spectra (e.g, Bond et al. 1997, Zaldarriaga et al. 1997, Efstathiou & Bond 1999). The best known example is the geometrical degeneracy between the matter density $h^2\Omega_m$, vacuum energy and curvature. This degeneracy is almost exact and precludes reliable estimates of the involved cosmological parameters from measurements of the CMB alone.

It can be broken by combining CMB data with other cosmological data sets, as direct estimates of Hubble's constant, determination of the magnitude-redshift relation for Type Ia supernovae or measurements of the power spectrum of the galaxy distribution determined from large galaxy redshift survey.

There are many more partial degeneracies, for example between the scalar mode spectral index n_S, baryon density ω_b and optical depth of reionization τ, which is very unfortunate because the latter depends on complex late time physics and is therefore poorly known. As a consequence of parameter degeneracies, accurate estimates of the cosmological parameters require the addition of astrophysical constraints. However, the latter are usually much more complex than observations of the CMB and often have unclear systematic errors, which can lead to serious biases in cosmological parameters (e.g, Seliak et al. 2003). These problems can be largely solved by making higher sensitivity measurements of the CMB temperature and polarization anisotropies.

1.5.4 Current knowledge of CMB anisotropies

In figure 1.2 we show the temperature power spectrum determined from the three year's data from the WMAP satellite (Spergel et al. 2006) combined with determinations from other experiments. The first and second acoustic peaks are measured with good precision, though the errors become large at $\ell \geq 500$ because of the limited angular resolution and sensitivity of WMAP. The red solid line shows the predictions of the best-fit ΛCDM model, while the shaded area accounts for cosmic variance. The best fit model is spatially flat, with Ω_Λ=0.73, ω_c=0.110, $\omega_b = 0.022$, $h = 0.70$, and has scale-invariant adiabatic fluctuations. The parameters of this model are consistent with many other astronomical data sets, including the 2dF and SDSS galaxy redshift surveys, the magnitude-redshift relation for Type Ia supernovae, measurements of the Hubble constant, and primordial Big Bang nucleosynthesis. For these reasons, this model is often referred to as the "concordance" ΛCDM model (see, e.g, Bahcall et al. 1999).

Despite the tremendous success of this model, however, some values of its parameters are surprising. Ordinary baryons, the only major constituent that has been directly detected in the laboratory, account for only 4% of the mass-density budget of the Universe. Only about a tenth have condensed into stars, the rest are in the diffuse intergalactic medium and in the central regions of clusters and group of galaxies. Cold dark matter, some other form of weakly interacting matter whose nature and history are unknown, accounts for the remaining clustered matter in the Universe. The largest contribution to the energy budget of the Universe is given by virtual particles that, according to quantum field theory, pervade the vacuum. This phenomenon is even less well understood than the weakly interacting dark matter. A calculation of the contributions of quantum zero-point fluctuations of fundamental fields gives a value for the cosmological constant which is 120 orders of magnitude higher than observed. This exceedingly small but non-zero value of the vacuum energy is one of the major unsolved problems in fundamental physics.

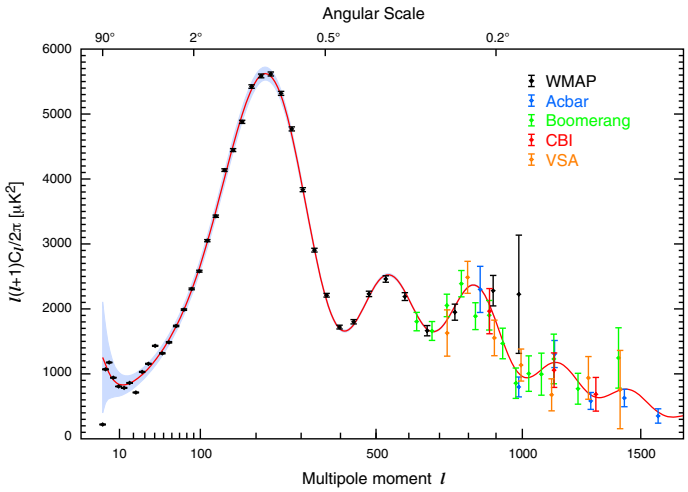

Figure 1.2: The WMAP three-year power spectrum (in black) compared to other recent measurements of the CMB angular power spectrum, including Boomerang, Acbar, CBI, and VSA. We aknowledge the WMAP Science Team for this figure.

Table 1.1: Comparison between the instrumental specifications of PLANCK and WMAP.

PLANCK									
Center frequency (GHz)	30	44	70	100	143	217	353	545	857
Angular resolution (arcmin)	33	24	14	9.5	7.1	5.0	5.0	5.0	5.0
RMS pixel noise $\Delta T^\star$	5.5	7.4	12.8	6.8	6.0	13.1	40.1	401	18291
WMAP									
Center frequency (GHz)	23	33	41	61	94				
Angular resolution (arcmin)	56	41	32	21	<14				
RMS pixel noise $\Delta T^\star$	70	70	70	90	100				

Noise levels are in μK thermodynamic. The conversion between thermodynamic temperature and the common units of flux are given in Appendix A.

1.6 Motivation of CMB experiments: the PLANCK mission

As we mentioned above, past CMB experiments have been extremely successful in measuring key parameters of the Universe. However, there are still a lot of open questions that should be answered. The investigation of these aspects requires higher precision measurements of the CMB anisotropies. To this end, other experiments have been designed, first of all the forthcoming PLANCK satellite.

In table 1.1 there is the comparison between the main specifications of the WMAP and the PLANCK satellites. We can see that PLANCK will have three times the angular resolution of WMAP, an order of magnitude lower noise at the same WMAP frequencies and a wider frequency range (30-857 GHz). The

effect of having better resolution essentially implies the possibility to recover the CMB power spectrum up to smaller scales. This is helpful to have better constraints on the cosmological parameters, as having a big number of accurately measured acoustic peaks allows us to reduce parameter degeneracy. Moreover, the resolution of PLANCK will allow us to look into the damping tail of the spectrum, where interesting effects appear.

The wide frequency range is important for component separation purposes. Even if the optimal frequency range for CMB measurements is 60-100 GHz, by mapping the microwave emission at lower and higher frequencies we increase the accuracy with which we detect the foreground components. As we will better discuss in Chapter 3, almost all component separation methods exploit informations on the foreground components, for example on their spatial structure, frequency dependence, or power spectra. Thus, a wider frequency coverage will allow substantial improvements in component separation, which is actually the major limiting factor to CMB experiments.

The most notable feature of PLANCK is however the very good signal to noise ratio. Thanks to the very low pixel noise, PLANCK will provide a reliable estimate of the CMB map, thus allowing us to go beyond the power spectrum estimation. As we already told, the CMB power spectra contain only the information related to the Gaussian component of the cosmological signal. Going beyond the power spectrum allows the search for non-Gaussianity in the CMB.

1.6.1 Beyond the power spectrum: non-Gaussianity

Non-Gaussianity in the CMB is a very active field of investigation. The search for primordial non-Gaussianity is mainly related to testing the inflationary models, as we will discuss in the next section. Moreover, non-Gaussianity is due to secondary anisotropies as well as to foreground emissions and instrument systematics.

The primary challenge in studies of non-Gaussianity is choosing the statistics that quantifies it: non-Gaussianity tells us what the distribution is not, not what it is. The secondary challenge is to optimize the statistics against the Gaussian noise of primary anisotropies and the non-Gaussian noise of foregrounds and systematics.

One of the non-Gaussian tests is the bispectrum, the harmonic analogue of the three-point correlation function. Theoretical work on the bispectrum showed that the inflationary contribution is not expected to be detectable in most models (Allen et al. 1987, Falk et al. 1993, Gangui et al. 1994). Conversely, signatures of secondary anisotropies turned out to be detectable.

The trispectrum, the harmonic analogue of the four-point function, also has advantages for the study of secondary anisotropies. It is also intimately related to the power spectra of quadratic combinations of the temperature field and has been applied to study gravitational lensing effects (Bernardeau 1997, Zaldarriaga 2000, Hu 2001).

Tests for non-Gaussianity localized in angular space include the Minkowsky functionals (Winitzki & Kosowsky 1998), the statistic of temperature extrema (Kogut et al. 1996), and wavelet coefficients (Aghanim & Forni 1999). These

may be more useful for examining foreground contamination and trace amounts of topological defects.

Non-Gaussian primordial models

According to the theory of inflation, the adiabatic perturbations originated by the quantum fluctuations are essentially Gaussian distributed. Thus, original non-Gaussianity is very small, although non-zero and calculable. Then, non-linear gravitational evolution on super-horizon scales after the inflation significantly enhances the original non-Gaussianity to an expected present level of order 10^{-5} of the RMS CMB temperature anisotropy. This level should be undetectable also by the forthcoming missions like PLANCK. However, other non-standard inflationary models, as the curvaton and the inhomogeneous reheating scenarios, may lead naturally to much higher levels of non-Gaussianity than standard single-field inflation. Thus, measuring a certain level of non-Gaussianity, or even posing an upper limit to it, would constraint inflationary models. There are also non inflationary models that can produce non-Gaussianity. In this case, models could be distinguished due to the different non-Gaussian signature they produce in the CMB.

A usual parametrization of non-Gaussianity expresses the primordial gravitational potential Φ like a linear Gaussian term ϕ_G plus a quadratic contribution (e.g, Verde et al. 2000):

$$\mathbf{\Phi}(\mathbf{x}) = \phi_G(\mathbf{x}) + f_{NL}\phi_G^2(\mathbf{x}), \tag{1.24}$$

where f_{NL} is a dimensionless parameter setting the strength of the non-Gaussian term. The primordial non-Gaussianities for standard inflationary models have $f_{NL} \sim 10^{-2}$, which is enhanced to $f_{NL} \sim 1$ by non-linear gravitational effects. According to other inflationary models, however, we may easily have $f_{NL} \gg 1$. There are, of course, more exotic pictures that can produce non-Gaussianity. For example, it is possible to closely mimic the CMB anisotropies of inflationary models by invoking a suitable source of stress energy. Topological defects could produce distinctive observational signatures in the cosmic microwave sky. For example, cosmic strings, whose production has some theoretical motivation in superstring-inspired brane inflation models, produce linear discontinuities. Cosmic textures produce hot and cold spots and global monopoles produce correlated pairs of hot spots. To detect these defects, it is necessary to develop a variety of custom statistics.

Large scale Geometry and Topology

The CMB sky provides an area for testing the assumption that on the largest scales space-time asymptotically approaches the Friedman-Robertson-Walker metric. Small deviations from this metric lead to observable signatures in the CMB. For example, open or flat models with global rotation or shear will exhibit a spiral pattern anisotropy. Additional geodesic focusing can also create hot spots in open models, while closed models exhibit a pure quadrupole pattern. The PLANCK CMB maps can be compared with templates generated for

non-maximally symmetric models (e.g., Bianchi models) to provide sensitive constraints. As the expected anisotropic patterns are on relatively large-scales, systematic limits are dominated by the ability to subtract Galactic foregrounds.

Because General Relativity is a local theory, the global topology of the Universe remains theoretically undetermined. The CMB offers a unique probe of a topologically compact Universe, since the compactness leads to fluctuations which are described by an anisotropic Gaussian random field. After averaging over an ensemble of observers, the net effect is that the CMB sky appears to be non-Gaussian. One can therefore hope to observe non-trivial topologies via their non-Gaussian signatures (Inoue 2001). In addition, a topology scale less than the horizon scale produces circles in the sky and the truncation in the angular power spectrum and correlation function of temperature fluctuations. The topological choices simplify in a flat universe where there are six physically allowed compact orientable topologies to consider, each of which leaves a distinct pattern on the CMB.

Non-Gaussianity from Secondary Anisotropies

It is important to be aware of the other sources of non-Gaussianity in real CMB maps, which could confuse the search for primordial non-Gaussianity. The temperature anisotropies of the CMB encompass both the primary cosmological signal, directly related to the initial density fluctuations, and the foreground contributions, amongst which are the secondary anisotropies. The latter are generated after matter-radiation decoupling and arise from the interaction of the CMB photons with the matter. The secondary fluctuations associated with cosmic structures induce non-Gaussian signatures in addition to those from the primary CMB anisotropies. The SZ effect due to galaxy clusters is one of the most important sources of secondary anisotropies. Owing to its peculiar spectral signature, the thermal effect will be separated to very good accuracy. However, the contribution from the kinetic SZ effect, which is spectrally indistinguishable from the primary anisotropies will not be easily subtracted.

Also, non-Gaussianity is imposed on the CMB by the lensing caused by non-linear structures along the line of sight. Non-linear evolution skews the lensing distribution by creating a tail of high magnification factors at the expense of magnification factor below unity. This leads, for example, to a non-Gaussian redistribution of hot-spots on the CMB (e.g., Takada & Futamase 2001).

Recent searches for non-Gaussianity

Searches of non-Gaussianity in CMB data have been performed on the whole-sky data sets presently available: the COBE and the WMAP data. Both have been found compatible with the Gaussian hypothesis by the majority of the statistical tests applied. Monte Carlo simulations, taking into account the instrumental and observational constraints of the data under analysis, are usually performed to estimate distributions of the testing statistic as well as confidence levels.

In the case of WMAP, Komatsu et al. (2003) analysed the temperature maps with angular bispectrum and Minkowsky functional techniques. They found

that the WMAP data are consistent with Gaussian primordial fluctuations, and established the most stringent limits on f_{NL} obtained so far, $-58 < f_{NL} < 134$, at the 95% confidence level. Both COBE and WMAP CMB maps show some weak evidence for non-Gaussianity, however all these effects resulted to be of systematic origin.

Also ground- and balloon-based experiments could shed more more light on the Gaussian hypothesis, however these experiments will suffer from their ability to cover only a small fraction of the sky over a restricted range of frequencies, and are therefore unlikely to make significant impact.

Thanks to the full sky coverage and the improved sensitivity compared to WMAP, PLANCK should give better constraints on non-Gaussianity. Of course, this will be possible only when non-Gaussian signals due to foreground emissions will be removed from the data, so component separation will be a crucial step.

Chapter 2

Foregrounds

2.1 Introduction

The primary objective of component separation is to provide a map of the Cosmic Microwave Background free from foreground contamination. However, in order to get a good foreground removal, we have to exploit known characteristics of foregrounds. In this Chapter, then, we are going to review the main foreground components.

The name "foregrounds" collectively refers to all emissions which mix with the CMB radiation. The name in particular suggests that those emissions are placed between the CMB and the observer. In fact, in a first approximation, the CMB anisotropies originate at the LSS ($z \simeq 1000$) and foregrounds are generated afterwards. However, this picture is complicated by the presence of secondary anisotropies, which also generate after the recombination epoch. To give a more correct definition, foregrounds are all the astrophysical processes which emit photons in the CMB frequency range. These photons add to the CMB ones, thus contaminating the cosmological signal.

Our present knowledge of foregrounds mainly comes from ancillary data: surveys from other experiments, mapping the emission of interest (or a certain tracer of it) at a frequency at which it is the dominant component. The extrapolation to the microwaves is then performed under certain hypotheses, which however are often only partially verified. The complementary approach is to exploit information obtained in the microwave range directly. In this case, as the foregrounds are mixed together, component maps must be products of component separation. Thus, we come to the second, but still crucial, objective of component separation: provide maps of the foreground components. As we will see throughout this Chapter, foreground components contain a lot of useful information still to be exploited. In particular, we will focus on what can be added to the science of foregrounds by data in the CMB frequency range, as those forthcoming with the PLANCK satellite.

2.2 Foreground classification

The main mechanisms which emit in the microwave are:

- synchrotron emission, which is due to electrons moving in a magnetic field,
- free-free emission, due to electron-ion scattering,
- thermal emission, due to dust grains. Dust grains are also supposed to emit through a non-thermal process, whose nature is still debated.

All foreground components emit through one - or a combination of - those emission processes. However, the same mechanism related to different objects in the sky gives rise to sources which are completely different from the morphological point of view and may have very different intensities. Thus, the classification of foregrounds must take into account which kind of objects are responsible of the emission.

A common classification divides foregrounds into "diffuse" and "point-like". This classification is very useful for component separation, as diffuse and point-like sources are dealt with different techniques, as we will discuss in Chapter 3. There are however intermediate situations, such as sources like SZ clusters, which have typical arcminute size. Depending on the resolution of the experiments, those sources can be treated as point-like or extended. Another classification, which we will adopt in this Chapter, distinguishes between Galactic and and extragalactic foregrounds, which are due to objects inside and outside our own Galaxy respectively. As we will see, the most relevant Galactic foregrounds are diffuse, while extragalactic ones are mainly point-like. Galactic foregrounds will be the topic of the next sections, while extragalactic ones will be discussed starting from § 2.4.

2.3 Galactic Foregrounds

The Milky Way is a spiral Galaxy. Thus, it is composed by a spheroidal component in the center (bulge), a flat component containing the spiral arms and defining the Galactic plane (disk), and another spherical component, much more extended and less dense than the bulge (halo). The bulge and the halo are relatively old: they contain old stellar populations and they are very poor of interstellar medium. Star-forming regions and phenomena related to young stars, like HII regions and SN explosions, are absent. Conversely, the disk component is young. It is filled by a dense ISM, composed by gas and dust grains. The local radiation field heats the medium, causing changes in the dust temperature and in the gas ionization.

The morphology of the Galaxy is important to understand Galactic foregrounds. The halo, which is poor of Galactic medium, does not emit in the microwaves, while the Galactic plane is a strong source of synchrotron, free-free, thermal and, possibly, non-thermal dust emission. Each emission has distinct morphology, as it traces a distinct component of the medium. However it is positively correlated with the other foregrounds, given the common structure of the Galaxy. While dust and free-free are more strictly confined in the Galactic disk, the synchrotron component is more extended in latitude, as the electrons are spread over the halo by the Galactic magnetic field.

In addition to large structures of gas and dust, the Galactic plane contains several classes of compact objects, representing different evolutionary stages of its young stellar population. The earliest phases of star formation are associated with dense cold cores of molecular clouds, deeply embedded in dust which have a color temperature $T_d < 20°$. Young hot stars are associated with HII regions, whose emission in the microwaves is due to both free-free and dust. Emission due to dust at temperatures of 100-200 K is associated to stars in the Asymptotic Giant Branch (AGB) phase. Finally, SN remnants are sources of both synchrotron and dust emission.

In the following sections, we will review the main characteristics of Galactic foregrounds, with special attention to the diffuse components. In fact, from the point of view of component separation, compact Galactic sources are not very interesting, as the usual way to deal with them is to adopt an appropriate sky masking.

2.3.1 Synchrotron emission

Synchrotron emission arises when relativistic electrons travel in a magnetic field. The spectral dependence of this emission is a power law, which, in antenna temperature [1], writes:

$$T_{A,synch} \propto \nu^{-\beta_s}. \tag{2.1}$$

The exponent β_s is called synchrotron spectral index. The value of the spectral index depends on the local energy spectrum of the electrons. Thus, it varies in the sky. It is also expected to steepen with frequency due to increasing energy losses of the electrons.

Synchrotron emission arise from two types of sources: electrons trapped in the magnetic field of discrete supernova remnants and diffuse emission from cosmic ray electrons spread throughout the Galaxy. The latter accounts for $\sim$90% of the emission.

If the spectral index varies wildly with the line of sight, the morphology of synchrotron maps would change substantially with frequency. The spectral index of diffuse synchrotron emission is generally assumed to lie in the range $2.5 < \beta_s < 3.1$. This is also confirmed by the study of external galaxies (Hummel et al. 1991).

Synchrotron emission can be highly polarized. Theoretically, the polarization degree can reach 75%. This is almost never observed, however, due to Faraday rotation and non-uniform magnetic field directions along the line of sight, which generally reduce the degree of polarization to $<$20%.

2.3.2 Free-free emission

This emission, which is also called "Bremsstrahlung", arises from the interaction of free electrons with ions in ionized media. The spectrum of free-free emission can be theoretically calculated assuming an electrically neutral medium

[1] The conversion between antenna temperature and the common units of flux are given in Appendix A.

consisting of ions and electrons. The result in antenna temperature is:

$$T_{A,ff} \propto \nu^{\beta}. \tag{2.2}$$

The spectral index β depends, objectively weakly, on the electron temperature and thus on the position in the sky. In the frequency range of interest here, is generally in the range from about 2.1 to 2.15.

Free-free emission, being due to incoherent emissions from individual electrons, is not polarized.

2.3.3 Thermal dust emission

Dust grains result from natural condensation in cool stellar atmospheres, supernovae, and in the interstellar medium of the heavy elements produced by nucleosynthesis in stars. The sizes of dust grains have a broad distribution ranging from a few nanometers to several hundred nanometers. The lightest grains are thought to be composed by polycyclic aromatic hydrocarbon (PAH) molecules, while the others are carbonaceous compounds and silicates. When the local radiation field heats a dust grain at a certain temperature T_d, it emits through the law:

$$T_{A,dust} \propto \nu^{\beta_d}/[\exp(h\nu/kT_d) - 1], \tag{2.3}$$

where the coefficient β_d, the dust emissivity index, is of the order of 2. The emissivity of a diffuse dust cloud is due to the superposition of the emissions due to all the grains, which have in general different T_d and β_d. The spread in temperature reflects the spread in size of the grains, as very small grains can reach very high temperatures, while big grains are normally cooler. Cool grains at the end of the size distribution dominate at long wavelengths ($\lambda > 100$ μm), hot grains dominate the 6-60 μm range.

According to the sub-millimeter data from PRONAOS (Dupac et al. 2003) the dust temperature ranges from 11 to 80 K and the emissivity index also exhibits large variations from 0.8 to 2.4. An anticorrelation between the temperature and the spectral index is also observed: cold regions have high spectral indices around 2, and warmer regions have spectral indices below 1.5. One possible interpretation for this effect is that the grain sizes changes in dense environments. Alternatively, the chemical composition of the grains could be different in different environments and this may correlate to the temperature. Finally, there could be an intrinsic dependence of the spectral index on the temperature due to quantum processes such as two-level tunneling effects.

In principle, thermal dust emission should not be strongly polarized, unless dust particles are significantly asymmetric and there exists an efficient process for aligning the dust grains. Preliminary dust observations with the Archeops instrument (Benoit et al. 2004; Ponthieu et al. 2005) seems to indicate polarization levels of order of few %, and as high as 15-20% in a few specific regions.

2.3.4 Anomalous dust emission

Cross-correlations studies of CMB and far-IR data have shown a microwave emission component with a spectral index suggestive of free-free emission. How-

ever, evidence from COBE, OVRO, Saskatoon, and the Tenerife experiments (de Oliveira-Costa et al. 2002; Mukherjee et al. 2001) indicates that this component is correlated with dust emission at a level unexpected from free-free. Theoretical work suggests that this emission may originate from very small spinning dust grains (Draine & Lazarian 1998). However, in diffuse regions it is difficult to reconcile the spectral index of the spinning dust emission with the observed one (Kogut 1999). Therefore, the source of the correlated emission is still an open question, and is often referred to as "anomalous emission".

New insights on the nature of the anomalous emission have been given by the WMAP experiment, which covers the 20-100 GHz range. The maximum entropy component separation performed by the WMAP team reveals a strong "synchrotron" component that is significantly different from the Haslam 408 MHz survey and is well correlated with dust. Thus, this component could include the anomalous emission. Evidences of the anomalous emission were uncovered combining WMAP data with other measurements, especially at lower frequencies (Lagache 2003; de Oliveirs-Costa et al. 2004; Finkbeiner 2004, Watson et al. 2005; Davies et al. 2006). Moreover, the polarization properties of the dust-correlated low-frequency component differ from those of the component well correlated with the Haslam template, suggesting a different emission mechanism (Page et al. 2006). Nevertheless, the exact nature, the spectral properties, and the spatial distribution of this foreground remain uncertain. There is not general agreement even on its existence; a combination of free-free emission and of strongly self absorbed synchrotron could also account for the data (Hinshaw et al. 2006).

2.3.5 Astrophysical interest of Galactic foregrounds

Diffuse emission from the Milky Way is particularly important to study the large-scale structure of our Galaxy. Combining maps of the Galactic emission it is possible to obtain a three-dimensional distribution of neutral gas, ionized gas, dust and magnetic fields throughout the Galaxy, providing important insights on its evolution. The three-dimensional distribution is particularly interesting for the solar neighborhood within 1 kpc. Some specific issues to be addressed are the relation of Gould's Belt to the nearest star-forming molecular clouds, the nature of the Local Bubble, and the fate of the clouds from which T-Tauri stars originate.

Another investigation is related to trace the evolutionary cycle of stars probing the various phases of the ISM, studying the morphology of star forming regions and determining the physical conditions of the circumstellar material.

The study of Galactic synchrotron is mainly related to the distribution of relativistic electrons and of the structure of the Galactic magnetic field. The distinctive synchrotron loops and spurs extending several tens of degrees from the Galactic plane are expected to provide important clues about the origin and evolution of the synchrotron disk and halo. Association with HI,Hα, and X-ray emission should help to clarify the origins of the synchrotron sky. Polarization observations of Galactic foregrounds is of great utility for the determination of magnetic field levels and directions. The underlying magnetic field can be

probed simultaneously via its effect on synchrotron and thermal dust emission. In fact synchrotron emission is sensitive to both the magnitude and direction of the magnetic field, while thermal dust emission can be polarized depending on the properties of the grains and their level alignment to the magnetic field.

A sensitive and homogeneous survey of the free-free emission of the HII regions in the Galactic disc will provide a reliable tool to study the global statistical properties of HII regions, with their relationship to the dust clouds. Since free-free emission is proportional to the number of ionizing photons only, whereas thermal dust is heated by both ionizing and non-ionizing photons, the dust to free-free luminosity ratio of star forming regions can be used as an indicator of the fraction of high mass stars in the complex.

Interesting developments are expected to come from the study of dust emission, in particular on the variation and composition of the grains. Also it is possible to derive the total dust masses in the structures of the ISM, from the high latitude cirrus to the nearby star forming molecular clouds. The relation between dust and gas is poorly investigated and only on large scales. Departures from gray body are also interesting, in particular temperature mixing due to the size distribution of large grains. The possible existence of very cold dust ($4K < T_d < 7K$) in the diffuse ISM remains to be tested.

Finally, the confirmation of the existence of the anomalous dust emission and the investigation of its physical mechanism is certainly a key aspect. This field is still largely unexplored, so results coming from CMB experiments are likely to greatly help in clarifying the situation. In § 5.5 we will discuss some original results obtained on the anomalous dust emission performing component separation of the three-year WMAP data.

2.4 Extragalactic foregrounds

Extragalactic foregrounds are due to different emission mechanisms related to objects outside our own Galaxy. As we are speaking of objects which are distant from us, they are generally not largely than a few arcminutes in size.

Extragalactic sources can be divided in two main categories: radio sources, which dominate at the lower CMB frequencies, and IR sources, dominating at the higher CMB frequencies.

In a first approximation, the sources have a Poissonian distribution over all the sky, which produces a typical "white noise" power spectrum. This means that C_ℓ does not depend on ℓ, so the power spectrum in terms of $T_\ell = \sqrt{\ell(\ell+1)C_\ell}$ increases with ℓ. In fact, selecting very small regions of the sky, the source count per area will be alternatively zero or one, which gives the maximum variance. Selecting wider regions, the number of sources per area tends to be more uniform, and the variance decreases.

This behavior is modified by the presence of source clustering, which introduces a non random component in the source distribution and modifies the power spectrum. In particular, clustering introduces another component in the power spectrum, important at multipoles corresponding to the typical cluster size.

The presence of clustering is relevant for IR sources, while it is low in the case of radio sources. This is however not related to the intrinsic propensity of those objects to cluster, but to the much broader luminosity function of radio sources, which strongly dilutes the angular correlation function.

2.4.1 Radio sources

The primary emission mechanism in virtually all radio sources is synchrotron emission from relativistic electrons. If the electrons have a power law spectrum, the synchrotron spectrum is also a power law $S_\nu \propto \nu^\alpha$. Depending on the spectral index α, radio sources are traditionally divided into two subclasses, "flat" ($\alpha > -0.5$) and "steep" ($\alpha > -0.5$) spectrum. Generally $\alpha < 0$, however sources with inverted spectra ($\alpha > 0$) are also present. Howevwr, we must keep in mind that the source spectra are complex, so that the effective spectral index varies with frequency.

Observations at mm/sub-mm wavelengths often reveal the transition from optically thick to optically thin radio emission in the most compact regions. The self absorption frequency carries information on the physical parameters. For example, it would be interesting to see if there is any systematic difference in the synchrotron turnover frequency between BL Lacs and quasars, as would be expected if BL Lac emission is angled closer to our line of sight. Correlation between turnover frequency and luminosity, which is boosted by relativistic beaming effects, would help confirm our current models.

Establishing the peak of synchrotron emission is also important to understand if the emission at higher energies is to be attributed to Compton scattering of the same synchrotron photons (synchrotron self-Compton) or of seed photons external to the synchrotron emitting region. The spectral break-frequency, ν_b, at which the synchrotron spectrum steepens due to electron energy losses is related to the magnetic field and to the "synchrotron age". The systematic multi-frequency study in the CMB range will thus provide a statistical estimate of the radiosource ages.

Another interesting field is the study of GHz Peaked Spectrum radio sources (GPS). It is now wildly agreed that these sources represent the early stage of evolution of powerful radio sources (Fanti et al. 1995; Readhead et al. 1996; Begelman 1996; Snellen et al. 2000). Conclusive evidence that these sources are young came from measurements of propagation velocities (Polatidis et al. 1999, Taylor et al. 2000; Tschager et al. 2000). The identification of these sources is therefore a key element in the study of the early evolution of radio-loud AGNs.

All these studies and much more would be allowed by a complete, uniform and unbiased sample such as that provided by Planck. Moreover, at present there are no high-resolution all-sky surveys of extragalactic discrete sources in the same frequency range of Planck, so it is likely that these data will also reveal new populations of sources as well as unexpected interrelations between known classes of sources.

2.4.2 IR sources

Thermal continuum emission in the infrared is due to dust present in external galaxies. These galaxies, which are referred to as "dusty" or "submillimetric" (see, e.g., Blain et al. 2002 for a review), are typically very faint in other wavebands, as most of their energetic output is absorbed and re-emitted by dust. In typical spiral galaxies the dust emission is known to be significantly extended, on the same scale as the stellar disk. The emission is certainly associated with molecular gas rich star-forming regions distributed throughout the galaxy, in which dust is heated by the hot, young OB stars. In the Ultra Luminous InfraRed Galaxies (ULIRGs) that are at sufficiently low redshift for their internal structure to be resolved, the great majority of the dust emission arises in a much smaller region within a merging system of galaxies. It is plausible that a significant fraction of the energy could be derived from an AGN surrounded by a very great column density of gas and dust. Alternatively, an ongoing centrally condensed burst of star-formation activity is an equally plausible power source.

Local Group galaxies and other nearby galaxies provide a convenient laboratory in which to study the properties of the interstellar medium on galactic scales. Extended cold dust ($6 \leq T \leq 15K$) has been detected with deep optical (e.g, Howk & Savage 1999) and submillimeter (SCUBA and ISOPHOT, e.g., Alton et al. 1998) observations. The dust is more extended in some cases than the starlight. Mapping of nearby galaxies provides an opportunity to explore fundamental questions related to this cold dust, for example how extended, massive and common are these cold components, and what is their nature and origin. If a massive cold dust component is found to be common in galaxies, it will be necessary to reassess their total mass content.

A systematic study of the luminosity function of star-forming galaxies will be the definitive analysis of the local submillimeter luminosity density, obscured volume-averaged star formation rate, and dust mass function, as well as of the newly discovered luminosity dependence of color temperature.

Besides those concerning low-redshift dusty galaxies, there are many fields of investigations related to distant dusty galaxies, which can provide new insights on galaxy formation and evolution. Discovering the process by which the dense, gravitationally bound galaxies formed in the Universe from an initially almost uniform gas, and understanding the way their constituent populations of stars were born is a key goal of modern physical cosmology.

To reproduce the galaxy counts obtained by SCUBA and the SED of the CIRB, an extraordinary evolution is required in the star formation rate. It has been proposed recently that the objects detected by SCUBA are elliptical galaxies during their primary and short episode of star formation at $z > 2$, before the onset of QSO activity in their centers takes place (Granato et al. 2000). A distinctive prediction of these models is that the galaxy counts in the far infrared and submillimeter bands should exhibit an extremely steep slope at fluxes $10 \leq S \leq 100$ mJy at 850 μm.

A study of clustering of these high redshift massive ellipticals will provide useful insights on properties such as the mass of the halo and the duration of the star-formation process (Magliocchetti et al. 2000) and test models for

the evolution of the bias factor with redshift (Moscardini et al. 1998). Strong clustering also affects the statistics of the intensity fluctuations due to non-resolved sources. The statistics of the fluctuations will be studied with particular attention to the autocorrelation function looking for the source clustering effect. The autocorrelation function is expected to change significantly with frequency, and is needed to correct CMB maps for the effects of these foreground sources.

2.5 Thermal SZ effect from galaxy clusters

The SZ effect, introduced in the previous Chapter (§ 1.4), is part of the CMB signal, so technically it is not a foreground emission. However, both diffuse and point-like component separation methods aim at extracting this component from primary CMB maps. This is possible thanks to the typical spectral signature of the SZ effect, so that in principle it can be distinguished from primary CMB anisotropies and other foregrounds using observations at several frequencies.

The SZ component begins to affect the CMB power spectrum at multipoles around 1000, however at these scales the foreground power spectrum is dominated by radio and IR point sources. Thus, removing SZ is of secondary importance to obtain a good determination of the CMB power spectrum. However, it is important for other applications, as studies of non-Gaussianity. Moreover, extracting this component is of primary importance, as this signal has great cosmological and astrophysical interest.

Galaxy clusters (GC) can be observed, besides in the microwaves through the SZ effect, also in the optical, through the starlight of their galaxies, and in the X-ray band, where the same IC medium responsible of the SZ effect strongly emits through bremsstrahlung. Therefore, one may wonder why it is worth to observe galaxy clusters in the microwaves, where the emission is weak and the detection complicated by a number of factors. This question has mainly two answers: first, both the optical and the X-ray emissions dim with redshift, so the SZ is the only way to make high redshift GC surveys. Second, the tSZ and the X-ray probe the IC medium in a different way. Combining the observation in both bands we have the unique opportunity of disentangling gas temperature and density, thus probing gas physics. As we will see, both motivations are of great importance from the cosmological and the astrophysical point of view.

2.5.1 GC surveys and the large scale structure of the Universe

The theory of structure formation from a Gaussian random field predicts that the number distribution of objects in mass is proportional to the mean cosmic matter density and falls off exponentially above the so-called non-linear mass scale, which is the typical mass which collapses at a given redshift (Press & Schechter 1974). The exponential decline in the number density of clusters with increasing mass implies that small changes in the dark matter power spectrum amplitude lead to large changes in the number density of massive clusters. Thus, determining the spatial cluster density allows one to calibrate sensitively the dark matter density fluctuations of the Universe (White et al. 1993; Viana & Liddle 1996; Eke et al. 1996)

Then, the evolution of the cluster population depends on the cosmological model, in particular on the density of matter and on the cosmological constant. In fact, the higher the matter density is, the more the expansion is decelerated and structures can grow against the expansion. Conversely, an higher value of the cosmological constant inhibits the structure formation, so GC need to form substantially earlier. Thus, mapping the number of GC as a function of redshift allows us to constraint the matter density and the cosmological constant.

Finally, GC trace the large scale structure of the Universe. It is now believed that gravitational collapse leads to highly anisotropic structures called sheets and filaments. From a dynamical point of view, this network of filaments represents the preferential directions along which the matter streams to build the massive and dense structures located at the nodes. This picture, first emerged from N-body experiments, was lately understood in a theoretical framework (Bond et al. 1996). The cosmic web corresponds to the density enhancements present in the primordial field that are sharpened by the following non-linear evolution. As clusters occur at the intersection between filaments, they are not randomly distributed, but highly correlated with each-other. The exact properties of the correlation depend on the cosmological model.

Important insights on structure formation, together with the confirmation of our theories, should come from the detection of the cosmic web itself, which however has proved to be challenging. So far, we have some indications coming from the galaxy distribution and cluster alignment (Geller & Huchra 1989; Plionis et al. 2003; Bardelli et al. 2000; Bharadwaj & Pandey 2004; Ebeling et al. 2004; Pimbblet et al. 2004; Pandey & Bharadwaj 2005; Porter & Raychaudhury 2005) and the study of the UV absorption line properties of active galactic nuclei (Bregman et al. 2004). An alternative approach is to try probing the gas present in the filaments which, according to hydrodynamical simulations, should have a temperature of $\sim 10^5$ K.

In Dolag et al. (2006) we investigated the possibility to detect the gas present in the filaments through its bremsstrahlung emission and the SZ effect, and to probe the mass distribution of the filament through measures of weak lensing. We carried out this analysis exploiting an high resolution hydro-dynamic simulation which follows the formation and evolution of a supercluster-like structure, containing 27 dark matter halos, of which four with virial mass around $10^{16} M_{\odot}$. We produced maps of the SZ effect, X-ray emission and shear amplitude due to weak lensing of the filamentary structure and discussed their physical and observational properties. The one- and two-dimensional structure is confirmed to produce X and SZ signal, however the level is low (10^{-16}erg/s/cm^2/arcmin^2 and $y = 10^{-6}$ respectively), so that a firm detection will be challenging also for future observations. Projection of the filamentary network however is found to bias the observational properties of galaxy clusters. In particular, the observed intensity of cluster can increase of 10% in the X-ray band and up to 30% in SZ. The weak lensing signal results to be rather difficult to observe.

2.5.2 SZ maps of nearby GC: probing the gas physics

According to the traditional picture, the IC gas is in hydrostatic equilibrium in the cluster potential. In this case, the temperature distribution is expected to be isothermal. However, recent high resolution X-ray imaging and spectroscopy by the Chandra and the XMM telescopes show regions of cool gas immersed in hot surroundings, thermal shocks, and other features indicative of a temperature distribution far from isothermal. Moreover, scaling relations between various cluster properties, like mass, temperature and X-ray luminosity, differ from the self-similar predictions, which hold in the hypothesis of hydrostatic equilibrium (see, e.g., the recent reviews by Rosati et al. 2002; Voit 2005; Borgani 2006 and the references therein).

In order to explain the ICM properties, many models have been developed so far, which consider the effect of radiative cooling and of non-gravitational heating (mainly feedback from supernovae and AGNs). As the complexity in the physical description of the ICM increased, hydrodynamic simulations have also improved to include such processes.

Even if cooling and heating are still too poorly understood to model them in detail in numerical simulations, nevertheless observed features like shocks and cool fronts can be reproduced.

As mentioned above, important improvements in the understanding of the physics of the IC gas are expected combining the existing X-ray data with SZ observations. An upcoming new generation of suitable instruments, like AMI, SPT, ACT, SZA, AMiBA, APEXand PLANCK, will allow accurate detections of the SZ effect in clusters. In order to correctly extract and utilize the information contained in these data it will be mandatory to keep under control both the dependence of the SZ signal on the ICM physics, and the possible biases induced on the intrinsic signal by the details of the observational process.

To this purpose, in Bonaldi et al. (2007b) we investigated how different choices for the physical modeling of the ICM affect the SZ radial profiles and the scaling relations between the SZ flux and other intrinsic properties of clusters. To this end, we used a set of high-resolution hydrodynamical simulations, where clusters were re-simulated including different physical processes, from radiative cooling, to star formation, energy feedback from supernovae, and thermal conduction. We found that the ICM physics has little effect on the slopes of the scaling relations, in agreement with previous studies (White et al. 2002; Nagai 2006). The main effect introduced in the scaling relations by radiative cooling is a lower normalization, in agreement with Nagai (2006).

We then performed mock observations of the most massive systems in our sample, in order to check whether our findings survive the observational procedure. In particular, we adopted the instrumental characteristics of the AMI interferometer, which is in its commissioning phase in Cambridge (UK) and has already obtained a first detection of a SZ decrement pointing towards the cluster A1914 (Barker et al. 2006) .

Given the arcminute resolution data from the current generation of SZE imaging experiments, the "observed" cluster maps do not allow us to appreciate the details present in the simulation. The maps appear to be smooth and regu-

lar; only structures due to an important merging event are still visible after the observation. Also the analysis of the cluster profiles will not be a sensitive probe of the different physics that is ongoing in the intracluster medium. However the information on the SZ flux integrated on a certain region of the sky, which can be used to analyze scaling relations, can be correctly reconstructed. Conversely, the peak SZ value exhibits large variations after the observational process, so that its interpretation is not straightforward.

2.6 Overview of diffuse foreground components

After having described the various foreground components in the previous sections, we can now discuss how they affect the CMB at the various frequencies and angular scales. In particular, we will focus on the diffuse components. For the following considerations and figures, we will exploit the Planck Sky Model (PSM, see § 4.3.1), which contains models for all the astrophysical emissions which are known to be mixed in the CMB frequency range.

In the upper panel of Fig. 2.1 we show the intensities of the Galactic foregrounds in the frequency range 10-1000 GHz. These intensities have been computed as the standard deviation of the full-sky component maps over all the sky.

As it can be seen, the lowest frequencies are contaminated by synchrotron, free-free and, possibly, anomalous emission, while the highest ones are dominated by thermal dust. The cleanest bands for the CMB are around 70-130 GHz. The lower panel of Fig. 2.1 shows the power spectra of all the components computed over all the sky; the intensities refer to a frequency of 100 GHz. Though 100 GHz is one of the optimal PLANCK bands for the CMB , it is clear that foregrounds contribute a relevant contamination. This contamination must be reduced in order to obtain good determinations of the CMB power spectrum.

Thus, the contamination due to foregrounds should be reduced exploiting a component separation method. The various techniques that can be adopted, and their advantages and shortcomings, are the subject of the next Chapter.

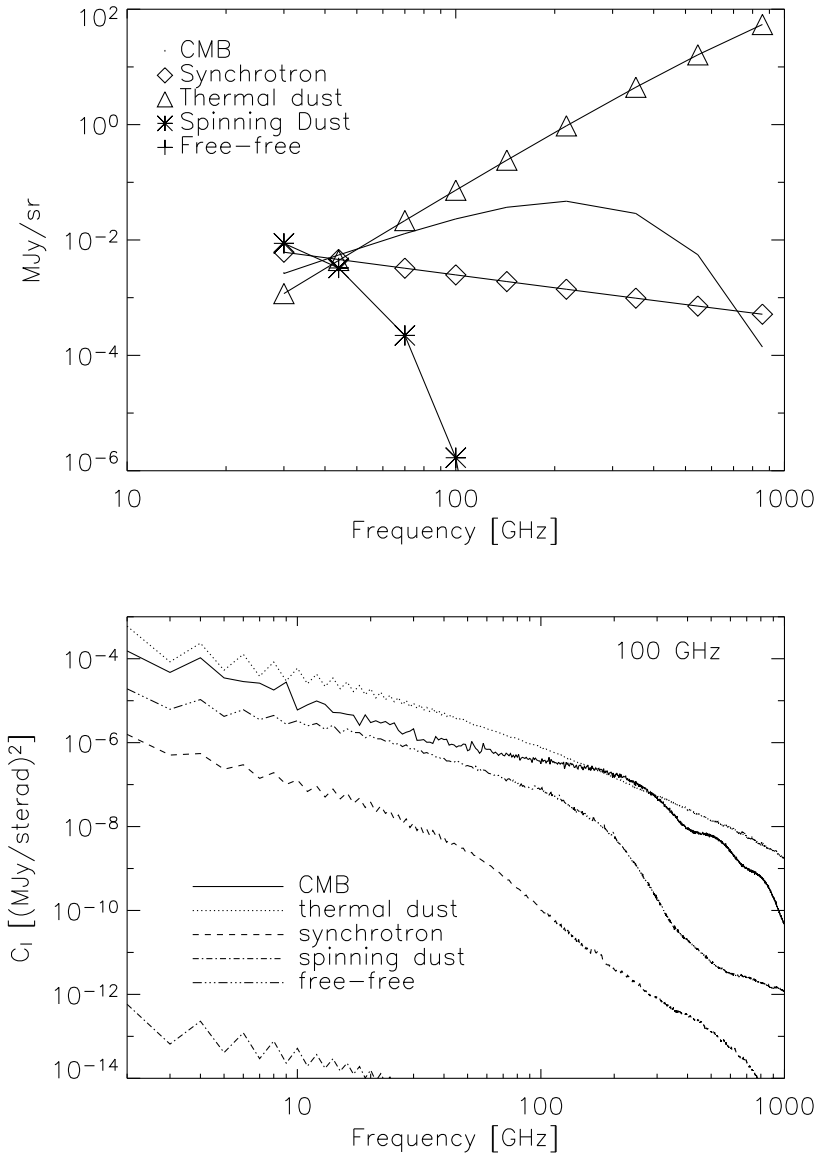

Figure 2.1: Galactic components compared to the CMB. Upper panel: frequency scalings; lower panel: power spectra at 100 GHz.

Chapter 3

Component separation

3.1 Introduction

In Chapter 1 we discussed the importance of the CMB radiation as a cosmological probe. This has motivated a series of missions aimed at accurately mapping it, which will culminate with the forthcoming PLANCK satellite. As experimental techniques improve rapidly, and new high-sensitivity missions are being planned and implemented, the main limitation for CMB measurement has changed from instrumental noise to separation of the cosmological CMB signal from foregrounds. As seen in Chapter 2, an accurate component separation is also crucial in order to exploit the astrophysical and cosmological information given by foreground components.

Since the CMB radiation has a virtually perfect blackbody spectrum (Mather et al. 1999), whereas all foreground signals have different spectra, it should be possible to disentangle the various contributions using spectral information. This fact motivated the use of multiple frequencies for the COBE-DMR experiment, for the current WMAP mission and for the future PLANCK mission. While the necessity of multi-frequency observations has been recognized within the cosmological community for a long time, there has been uncertainty about how those observations should be utilized. Many different component separation methods have been proposed, which make use of different concepts and techniques from signal processing science.

As explained in the previous Chapter, CMB maps are affected by contamination due to both diffuse components, mainly Galactic emissions, and point-like components, mainly extragalactic sources. Due to the different properties of those emissions, a component separation method which is able to extract both of them does not exists. Methods suited for diffuse and point-like component separation have very different frameworks and evolved independently. Thus, the description of the diffuse component separation problem is self-consistent, in the sense that it does not require to approach also the point-like one, and vice-versa, although obviously the two approaches must be combined when dealing with real data.

An introduction to the problem of separation of compact sources and of SZ clusters are briefly presented in the next sections. Then, we will focus on dif-

fuse component separation methods. After a review of the main techniques, we will present at the end of the Chapter a recently proposed technique for diffuse component separation, the Correlated Component Analysis (CCA), whose development for the PLANCK mission is the main objective of the work presented in this Thesis.

3.2 An introduction to source extraction methods

The main reason why point-like and diffuse foregrounds are generally approached with completely different methods is that point sources have an important distinctive feature: their projected angular shape is a Dirac's δ-like function convolved with the instrument beam response function. Thus, most methods for detection and extraction of point sources takes into account their specific angular shape through filtering techniques. Conversely, as we will see in the following sections, diffuse component separation methods mainly rely on the hypothesis that each component is characterized by a certain frequency behavior, almost uniform over all the sky.

A well-known result of signal-processing theory is that linear filters with translational invariance are devices which are frequency-selective in the Fourier sense. This means that a filter selects or removes some of the features of the image depending on their scale. We consider the detection of compact (point-like) sources in a 2-dimensional (2D) image with spatial coordinate $\mathbf{x}$, $x \equiv |\mathbf{x}|$. The observed flux of a source $s(x)$ of intrinsic flux density A filtered by a beam which we suppose to be circularly symmetric $\tau(x)$ is

$$s(x) = A\tau(x). \tag{3.1}$$

The 2D data image is given by the filtered source plus a background contribution:

$$y(\mathbf{x}) = s(x) + n(\mathbf{x}) \tag{3.2}$$

The background $n(\mathbf{x})$ is modeled by a homogeneous and isotropic random field with average value $\langle n(\mathbf{x})\rangle = 0$ and power spectrum

$$\langle n(\mathbf{q}) n\dagger(\mathbf{q}')\rangle = P(q)\delta_D^2(\mathbf{q}-\mathbf{q}'), \tag{3.3}$$

where $n(\mathbf{q})$ is the Fourier transform of $n(\mathbf{x})$, $q \equiv |\mathbf{q}|$ and δ_D^2 is the 2D Dirac delta.

A generic spherically symmetric 2D filter $\Psi(\mathbf{x}; R, \mathbf{b})$ is given by:

$$\Psi(\mathbf{x}; R, \mathbf{b}) \equiv \frac{1}{R^2}\psi(\frac{|\mathbf{x}-\mathbf{b}|}{R}), \tag{3.4}$$

where R and $\mathbf{b}$ define a scaling and a translation, respectively. This filter is characterized by covariance under $\mathbf{x} \rightarrow R(\mathbf{x}-\mathbf{b})$ transformation. Once filtered, the data $y(\mathbf{x})$ becomes:

$$w(R, \mathbf{b}) = \int d\mathbf{x} y(\mathbf{x})\Psi(\mathbf{x}; R, \mathbf{b}) \tag{3.5}$$

The idea under filtering is that in the filtered data $w(R, \mathbf{b})$ the sources are amplified, and thus can be detected with better S/N, compared to the original image $y(\mathbf{x})$.

3.2.1 Some example of filters

The matched filter and the scale-adaptive filter

The matched filter (MF, Tegmark & de-Oliveira-Costa 1998) and the scale-adaptive filter (Sanz et al. 2001; Herranz et al. 2002a) can be derived by imposing certain requirements on the filtered field $w(R, \mathbf{b})$. Let us assume that the filter satisfies the following conditions:

1. $w(R_0, \mathbf{0})$ is an unbiased estimator of the amplitude of the source:

$$w(R_0, \mathbf{0}) = s(0) \equiv A \tag{3.6}$$

2. The variance of $w(R, \mathbf{b})$ has a minimum at scale R_0, i.e. it is an efficient estimator of the amplitude of the source.

   With these two conditions, we have the MF, which is expressed in the Fourier domain by:

$$\tilde{\psi}_{MF}(q) = \frac{1}{2\pi a}\frac{\tau q}{P(q)},\ a \equiv \int dq\, q \frac{\tau^2(q)}{P(q)}, \tag{3.7}$$

   where $\tau(q)$ is the profile of the source in Fourier space. The scale-adaptive filter is obtained adding to the two previous conditions the following:

3. $w(R, \mathbf{b})$ has a maximum at $(R_0, \mathbf{0})$.

   The scale-adaptive filter is:

$$\begin{aligned} \tilde{\psi}_{SA}(q) &= \frac{1}{2\pi\Delta}\frac{\tau q}{P(q)}[2b + c - (2a+b)\frac{d\ln\tau}{d\ln q}], \\ \Delta &\equiv ac - b^2 \\ a \equiv \int dq\, q\frac{\tau^2(q)}{P(q)},\ b &\equiv \int dq\, q^2 \frac{\tau(q)}{P(q)}\frac{d\tau}{dq},\ c \equiv \int dq\, q^3 \frac{1}{P(q)}(\frac{d\tau}{dq})^2 \end{aligned} \tag{3.8}$$

In the case of the MF, one obtains a slightly higher gain, i.e. a larger amplification of sources in filtered space, but sources must be identified "a posteriori", looking for maxima in the S/N map. Conversely, the scale-adaptive filter allows us to get the sources in a straightforward manner, looking for maxima in the filtered map.

The Mexican Hat Wavelet Family (MHWF)

The MHWF has been discussed by Gonzalez-Nuevo et al. (2006). This is a family of filters $\psi_n(x)$ obtained by applying iteratively the Laplacian operator Δ to the Gaussian function:

$$\psi_{n,MH}(x) \propto \Delta^n \phi(x), \tag{3.9}$$

where ϕ is the 2D Gaussian $\phi(x) = 1/2\pi \exp[-x^2/2]$. Any member of this family can be written in Fourier space as:

$$\tilde{\psi}_{n,MH}(q) \propto q^{2n} \exp[-q^2/2]. \tag{3.10}$$

In particular, $\psi_1(x)$ is the usual Mexican Hat Wavelet, which has been extensively tested in the field of point detection with excellent results. The goal of the work by Gonzalez-Nuevo et al. (2006) was to compare the performance of some members of the MHWF and the main conclusion is that the second-level wavelet $\psi_2(x)$ (MHW2) performs better than $\psi_1(x)$ (MHW1) for the channels of the LFI of PLANCK. Lopez-Caniego et al. (2006) performed a comparison of the most used filters in all the PLANCK channels. They found that MHW2 and MF outperform the MHW1 in some aspects. In particular, the three methods detect the same number of objects; however, MHW1 presents a higher number of spurious detection respect to the other two.

3.3 An introduction to SZ extraction methods

Most of the methods designed for the extraction of SZ clusters rely on filtering techniques which are generalized to exploit also the known spectral signature of the SZ effect. There are two different approaches one can follow to include the frequency dependence of a signal in the filtering of multi-channel data. The first approach is to filter each channel separately, but carefully taking into account the cross-correlation between the different channels and the frequency dependence of the signal. In this way we obtain an output set of filtered maps that, when added to each other, is optimal for the detection. This philosophy is adopted by the multifilter methods. A second approach is to use the information about the correlations and frequency scaling before filtering in order to find the optimal combination of channels that maximizes the signal-to-noise ratio of the sources, and then use a filter on the optimally combined map. This leads to design a combination method with a single filter. We will briefly discuss both approaches in the next sub-sections, after the statement of the problem which follows.

The cluster signal is given by $A\tau(x)$, where A is the amplitude of the effect and $\tau(x)$ is the spatial template. One possible choice for $\tau(x)$ is:

$$\tau(x) = \frac{1}{\sqrt{1+(x/rc)^2}}, \tag{3.11}$$

where r_c is the core radius of the cluster. At each observing frequency this template is convolved with the corresponding antenna beam, to produce the convolved profile $\tau_\nu(x)$. Thus, we have

$$s_\nu(x) = A\tau_\nu(x). \tag{3.12}$$

We then consider a set of N 2D images with data values defined by

$$y_\nu(\mathbf{x}) = f_\nu s_\nu(x) + n_\nu(\mathbf{x}), \quad x \equiv |\mathbf{x}|, \tag{3.13}$$

where f_ν is the frequency dependence of the SZ effect and $n_\nu(\mathbf{x})$ is the generalized noise, which is again modeled as an homogeneous and isotropic random field with average $\langle n(\mathbf{x})\rangle = 0$ and power spectrum given by eq. (3.3).

3.3.1 The multifilter method

Multifilters can be constructed in several different ways. We consider here the two main possibilities, which are the scale-adaptive multifilter and the matched multifilter, obtained for generalization of the scale-adaptive filter and the matched filter introduced in § 3.2.1. The results which follow are obtained under the hypothesis that the backgrounds are white noise. For the scale-adaptive multifilter, one gets:

$$\begin{aligned} f_\nu \tilde{\psi}_{SA,\nu}(q) &= \frac{\tau}{N} \frac{f_\nu^2 P_\nu^{-1}}{\sum_\nu f_\nu^2 P_\nu^{-1}} [1 - \frac{b}{H}(2 + \frac{d \ln \tau}{d \ln q})], \\ N &= \int dq \tau^2 - \frac{b^2}{H},\ b = \int dq \tau^2 (2 + \frac{d \ln \tau}{d \ln q}), \\ H &= \int dq \tau^2 (2 + \frac{d \ln \tau}{d \ln q})^2, \end{aligned} \tag{3.14}$$

where P_ν^{-1} is the inverse of the noise power spectrum (which is a constant in our case) at the frequency ν. The matched multifilter is:

$$f_\nu \tilde{\psi}_{MF,\nu}(q) = \frac{\tau}{N} \frac{f_\nu^2 P_\nu^{-1}}{\sum_\nu f_\nu^2 P_\nu^{-1}},\ \ N = \int dq \tau^2. \tag{3.15}$$

For a recent evaluation of the performances of a matched multifilter for SZ extraction on PLANCK, AMI and SPT data see Melin et al. (2006).

3.3.2 The combination method

The linear combination of the original frequency maps is constructed so that it maximally boosts objects with a given spatial template and frequency dependence above the background. In general, the combination map is given by

$$y(\mathbf{x}) = \sum_\nu c_\nu y_\nu(\mathbf{x}), \tag{3.16}$$

where c_ν is some set of weights. This combined map can be written as

$$y(\mathbf{x}) = At(x) + \epsilon(x) \tag{3.17}$$

where the combined template $t(x)$ an background $\epsilon(x)$ are given simply by

$$t(x) = \sum_\nu c_\nu f_\nu \tau_\nu(x),\ \ \epsilon(\mathbf{x}) = \sum_\nu c_\nu n_\nu(\mathbf{x}). \tag{3.18}$$

The optimal values of the weights c_ν are found by maximizing the quotient $Q = at(\mathbf{0})/\sigma_\epsilon$, where σ_ϵ is the dispersion of the combined noise field $\epsilon(\mathbf{x})$. Thus, one is maximizing the 'detection level' of the object of interest above the background. Once we have constructed the combined template $t(x)$ we can apply either a scale-adaptive filter or a matched filter to the single combined image given by eq. (3.17).

3.3.3 Comparison of methods

The methods we just described are compared on simulated PLANCK data by Herranz et al. (2002b). From the methodological point of view, the main difference between the combination method plus a single filter and the multifilter method is that the first one uses the multifrequency information to give the optimal starting point for the filter, while multifilters produce the optimal ending point after filtering. In that sense, multifilters are more powerful than a single filter applied to an optimally combined map. The cost of this higher efficiency, however, is an increase of the complexity of the filters and therefore of the computational time required to perform the data analysis. For example, in the application to simulated PLANCK observation, the multifilter method requires $\sim$10 times more CPU time than the combination method, just because the latter filters only once.

Regarding the type of filter, as we already mentioned matched filters give an higher gain. Conversely, adaptive filters reduce the number of spurious sources, i.e. errors in the detections. This is due to the fact that the optimal scale-adaptive filter includes a constraint on the scale of the sources that is not present in matched filters design. This constraint characterizes the source with more precision but also restricts the minimization of the variance in the filtered maps.

The main results of the simulation performed by Herranz et al. (2002b) are the following:

- Single filtering of an optimally combined map is less sensitive than multifilters, producing around 20 per cent fewer detections at 3σ than the matched multifilter. Single matched and scale-adaptive filters perform very similarly.

- Multifrequency information reduce the number of spurious detections.

- The scale-adaptive multifilter perform worse than the matched multifilter because its main advantage, which is the removal of spurious sources, has already been accomplished by the multifrequency information included in the filter. Since the clusters one is trying to detect are very faint, it is the overall gain that is the most important. At 3σ, the scale-adaptive multifilter detects 40 per cent fewer clusters than the matched multifilter.

3.4 Diffuse component separation: generalities

3.4.1 Reduction of foreground contamination

Before starting with the review of the main diffuse component separation methods, in this section we will list some very simple techniques which can be used to reduce foreground contamination. Owing to their simplicity, all of these methods have been used widely in the context of CMB experiments, in some cases substituting a real component separation process. However, those techniques are not very efficient, in particular not enough for a modern full-sky mission like PLANCK. Moreover, the problem of extracting the astrophysical components

besides CMB is not addressed. Nevertheless, the simple techniques we are going to explain are still widely used in the context of the PLANCK mission, not in alternative but in combination with component separation methods. For the discussion which follows, we mainly refer to Delabrouille & Cardoso (2007).

Perhaps the most obvious solution to avoid contamination by foregrounds is to select the region of observation in such a way that the contamination is minimal. This sensible strategy has been adopted by ground-based and balloon-borne experiments observing only a part of the sky. In this case, CMB observations are made away from the Galactic plane, in regions where foreground contamination from the Galactic emissions is known to be small. For full-sky experiments, a strategy for keeping the contamination of CMB observations by foregrounds consists in masking regions suspected to comprise significant foreground emission, and deriving CMB properties in the "clean" region. For example Bennett et al. (2003) computed four Galactic masks of varying severity excluding from 4% to 20% of the sky. The shortcoming of adopting wide masks is that limiting the fraction of the sky exploited to compute the CMB power spectrum increases the cosmic variance and makes it impossible to constrain the lowest CMB multipoles. Moreover, when exploiting the spherical harmonics transforms, the basis is no longer orthonormal on the cut sky. This introduces a mode-mode coupling in the power spectrum which must be corrected for, as we will discuss in § 3.5.3.

In the context of diffuse component separation, sky masking is widely used. First of all, it is by now the safest way to reduce the contamination from point sources. Whenever possible, this masking is performed even before diffuse component separation, as the presence of point sources is nasty for most of the algorithms. Then, Galactic masks can be adopted to reduce the contamination from diffuse components both before and after the component separation process.

Another sensible option is the selection of the frequency of observation. For observing the CMB , it is convenient to exploit bands around 70-100 GHz, while to better trace the contribution of the foregrounds lower and higher frequency channels must be added. The observational channels of the PLANCK mission have been chosen to provide a good frequency coverage for all purposes. Besides three "clean" channels (70, 100, 143 GHz), there are two lower frequency channels to trace synchrotron, free-free, and other possible low-frequency emissions (30, 44 GHz) and four high frequency channels to accurately trace thermal dust emission and the far-IR background (217, 353, 545, 857 GHz). Note that 217 GHz is also the frequency at which the thermal SZ effect has null contribution. When performing component separation, depending on the method and on the objective, one can exploit all the channels or only a subset. For example, if the goal is to obtain a CMB map as clean as possible, often the highest and lowest frequencies are excluded from the analysis. Then, when trying to recover foreground maps, the configuration can be different.

3.4.2 Formalization of the diffuse source separation problem

Let us consider the sky radiation as a function of the direction $\hat{r}$ and the frequency ν, and assume that it results from the superposition of signals coming from N_c different physical processes:

$$\tilde{x}(\hat{r},\nu) = \sum_{j=1}^{N_c} \tilde{s}_j(\hat{r},\nu) \tag{3.19}$$

where $\tilde{x}$ is the total radiation from the direction $\hat{r}$ at frequency ν and $\tilde{s}_j$ are the individual physical processes that form the total radiation.

The signal $\tilde{x}$ is observed through a telescope, whose beam pattern can be modeled, at each frequency, as a shift-invariant point spread function $B(\hat{r},\nu)$. For each value of ν, the telescope de-focuses the physical radiation map by convolving it with the kernel B. The frequency-dependent convolved signal is input to an N_d-channel measuring instrument, which integrates the signal over frequency on each of its channels and adds some noise to its output. The final signal at the output of the measurement channel at frequency ν is given by

$$x_\nu(\hat{r}) = \int B(\hat{r}-\hat{r'},\nu') \sum_{j=1}^{N_c} t_\nu(\nu')\tilde{s_j}(\hat{r'},\nu')dr'd\nu' + n_\nu(\hat{r}), \tag{3.20}$$

where $t_\nu(\nu')$ is the frequency response of the channel and $n_\nu(\hat{r})$ is the related noise map. The realistic data model expressed by eq. (3.20) can be simplified making the following assumptions:

1. Each source signal is a separable function of location and frequency:

$$\tilde{s}_j(\hat{r},\nu) = \bar{s}_j(\hat{r})f_j(\nu) \tag{3.21}$$

2. $B(\hat{r},\nu)$ is constant within the passband. These two assumptions leads us to a new data model:

$$x_\nu(\hat{r}) = B_\nu(\hat{r}) * \sum_{j=1}^{N_c} h_{\nu j}\bar{s_j}(\hat{r}) + n_\nu(\hat{r}), \tag{3.22}$$

where $*$ denotes convolution and

$$h_{\nu j} = \int t_\nu(\nu')f_j(\nu')d\nu'. \tag{3.23}$$

This data model can be further simplified by doing another assumption:

3. The response function pattern of the telescope is the same for all measurement channels, that is:

$$B(\hat{r},\nu) = B(\hat{r}) \tag{3.24}$$

In this case, eq. (3.22) can be rewritten in vector form as:

$$\mathbf{x} = \mathbf{Hs} + \mathbf{n}. \tag{3.25}$$

The data vector $\mathbf{x}$ is a $N_d \times n_p$ vector, where N_d is the number of detectors and n_p the number of pixels, and contains the elements x_ν for each frequency. The $N_c \times n_p$ source vector $\mathbf{s}$ is given by the source functions $\bar{s}_j$, as defined in eq. (3.21), convolved with the frequency-independent radiation pattern B. The $N_d \times N_c$ matrix $\mathbf{H}$ is the mixing matrix whose elements are the $h_{\nu j}$ defined by eq. (3.23).

The one stated in eq. (3.25) is the linear mixture model, which is probably the most popular model of observations for source separation in the context of CMB observations. This model has been derived in pixel space, but it can be identically expressed also in Fourier or harmonic domain. It is worth noticing that in this case assumption 3 is not necessary. In the conjugate space, in fact, convolution becomes a multiplication and the effect of the kernel B can be easily incorporated for each wavenumber in the elements $h_{\nu j}$ of the mixing matrix. As we will better discuss in the following section, this has an important consequence for real experiments, for which assumption 3 is generally not satisfied. When working in pixel domain, higher resolution channels must be degraded to the worst one.

Under the above assumptions, the problem of component separation consists in inverting the linear system of equation (3.25). For linear inversion methods it means finding the best possible matrix $\mathbf{W}$ such that

$$\hat{\mathbf{s}} = \mathbf{W}\mathbf{x} \tag{3.26}$$

is an estimator of $\mathbf{s}$ as good as possible. The only element which is known in equation (3.25) is the data vector $\mathbf{x}$. The actual noise realization present in the data is unknown, however we in general know its statistics, i.e. the covariance in pixel domain or the power spectra in the harmonic domain. Both the source vector $\mathbf{s}$ and the mixing matrix are unknown. Given the number of unknowns, the system inversion is unsolvable unless additional information is provided. In other words, the problem is ill-conditioned. Component separation methods exploit additional constraints, reflecting our knowledge of the source and noise processes. However, each prior information also contains some further simplification or approximation of the problem. Depending on the different constraints adopted, the solution corresponding to different methods will have different advantages and drawbacks. In the following, we will give an overview of the main techniques, highlighting the peculiar characteristics of each method and its strengths and weaknesses.

3.4.3 Choice of the basis

Most of the algorithms we will describe in the following can in principle be implemented equivalently with any representation of the data: in pixel domain, Fourier of harmonic space, or on any decomposition of the observations on a set of functions. However, some of the algorithms are more efficient (in terms of computational time, goodness of the results or both) if a certain basis is adopted. Moreover, the use of a certain basis has some intrinsic implications, which translates into advantages and drawbacks. Thus, in absence of other

conditions, one should choose it according to the main objective he wants to achieve.

The problem of diffuse component separation on a set of data on the celestial sphere is mainly treated in real (pixel) space and in its conjugate space. This is the Fourier domain if we consider a plane sky patch, and the harmonic domain if we consider the celestial sphere.

The pixel space has the advantage that the use of sky masks and cuts is straightforward, as it corresponds to simply considering only a subset of all the pixels in the sky. Moreover, each pixel correspond to a certain position on the sky, so that position dependent information, like the spatial variability of the spectral dependencies, can be handled in a direct way. It is worth noticing that the spatial information can be in part exploited also when adopting the linear mixture model (3.25), which assumes a constant mixing matrix. In fact, when working in pixel space nothing prevents from selecting different regions on the sky and performing the analysis separately. For example, recent work suggest that the spectral index of synchrotron emission across the Galactic plane could be considerably flatter than at high latitudes. In this case, when a uniform mixing matrix is assumed, we can at least perform different analyses at high and low latitudes.

The main weakness of the approaches in pixel domain is that channel-dependent beams cannot be easily handled. When considering a set of channels having different instrumental beams, there is the need to equalize the resolution to the worst one. This is an unpleasant feature, as one would want to exploit the full instrumental resolution. For example, PLANCK contains nine channels, from 30 to 857 GHz, having resolution ranging from 30' to 5'. In this case, a component separation algorithm working with all the channels in pixel space requires to throw away the high multipole information.

Working in the Fourier and in the harmonic domain has the advantage that there is a simple way of taking into account different beams without the need of degrading the data to a common resolution. This allows us to exploit the full experimental resolution. The price to be paid is that the conjugate space does not retain the information on the spatial position, so spatially varying spectral indices cannot be easily treated anymore. Moreover, the procedure of masking part of the sky is also not straightforward, as it may introduce unpleasant features in the conjugate space.

The harmonic domain allows us to treat data on the sphere, thus it is the most natural conjugate space to be used in the context of a full-sky mission. However, there is a caveat: the spherical harmonics are a basis on the whole sphere, not on parts of the sphere. Thus, exploiting this basis in principle requires to perform strictly a full-sky analysis, without any Galactic mask or sky cut. Another problem is that when assuming a uniform mixing matrix we are forced to exploit it for all the sky, neglecting in principle any spatial variability.

The use of the Fourier domain does not have the problem of considering the whole sphere, however it is not straightforward for full-sky experiments. In fact, it requires to divide the sky in several square patches, so small that their curvature can be neglected, perform the analysis separately and then reconnect

the pieces. The latter step is particularly nasty, as it produces undesiderable features in the power spectra on the angular scale corresponding to the mean patch size. For this reason, this basis is not extensively used in the context of the PLANCK mission, even if it can be useful for particular applications.

3.5 Non blind methods

This is a class of traditional methods largely studied in the literature. The fundamental hypothesis of these methods is that the mixing matrix $\mathbf{H}$ is known. More in detail, the mixing matrix can be normalized such that we only need to know the frequency scaling of the components, not their relative intensities. Nevertheless, this is certainly a strong assumption, which constitutes the main limitation of this class of techniques.

The hypothesis of the known mixing matrix is based on the fact that, even if the actual frequency dependence of all the components is not known, we can formulate plausible guesses exploiting external data sets. For example, in the simple case of the mixture of four components, CMB and Galactic synchrotron, thermal dust and free-free, we can proceed as follows. The frequency scaling of the CMB is a blackbody with high accuracy:

$$T_{\mathrm{A,CMB}}(\nu) \propto \frac{(h\nu/kT_{\mathrm{CMB}})^2 \exp(h\nu/kT_{\mathrm{CMB}})}{(\exp(h\nu/kT_{\mathrm{CMB}})-1)^2}. \tag{3.27}$$

Similarly the frequency spectrum of the free-free emission is determined by fundamental physics and can be expressed by eq. (2.2). Then, we know that synchrotron and dust behave as in eqs. (2.1) and (2.3). The spectral indices of these components however are not known, and they are also known to vary with the position. To constrain these spectral indices we can exploit external data sets. This analysis requires maps of the emission of interest at least at two frequencies. This information in principle allows us to compute a map of spectral indices; however, often the information is averaged over the sky. A limitation of this analysis is that the external data refer to frequencies which are often far from the CMB range. Once extrapolated to the range of interest, the computed spectral indices could be not correct anymore.

Despite the difficulties, let us suppose that we finally have a plausible mixing matrix. Exploiting this and, in general, more information, we have various formulations for the reconstruction matrix $\mathbf{W}$, which allows us to solve the component separation problem through eq. (3.26). In the following, we are listing the main possible solutions. It is worth noticing that the relations we will derive for each of them are exact only if the mixing matrix is the "true" one. In particular, those relations constitute an upper limit to the quality of the reconstruction, which rapidly worsens with increasing errors in the mixing matrix; nevertheless, they allow us to discuss the main differences between the techniques.

If the mixing matrix $\mathbf{H}$ is square, i.e. we have as many detectors as components, and if it is non singular, $\mathbf{W}$ is simply obtained as:

$$\mathbf{W} = \mathbf{H}^{-1} \tag{3.28}$$

and we have:

$$\hat{\mathbf{s}} = \mathbf{H}^{-1}\mathbf{y} = \mathbf{s} + \mathbf{H}^{-1}\mathbf{n}. \tag{3.29}$$

This is the so-called simple inversion solution. Alternatively, if there are more observations than components, then the inversion can be obtained by the pseudo-inverse solution:

$$\mathbf{W} = [\mathbf{H}^{\dagger}\mathbf{H}]^{-1}\mathbf{H}^{\dagger} \tag{3.30}$$

so that

$$\hat{\mathbf{s}} = [\mathbf{H}^{\dagger}\mathbf{H}]^{-1}\mathbf{H}^{\dagger}\mathbf{y} = \mathbf{s} + [\mathbf{H}^{\dagger}\mathbf{H}]^{-1}\mathbf{H}^{\dagger}\mathbf{n}. \tag{3.31}$$

The two solutions we just presented contain the source vector $\mathbf{s}$ plus a noise contribution. Thus, they provide unbiased estimators of the components. However, because of the remaining noise terms, these inversions are not in general the best solutions in terms of residual error, in particular in the poor signal to noise regimes. To suppress the noise contribution other solutions exist, which however require to know something additional about the noise, namely, its second-order statistics. These are described by noise correlation matrices in real space, or alternatively by noise power spectra in Fourier or in harmonic space.

Let us now assume that we know the second-order statistics of the noise, which is contained in the matrix $\mathbf{C_n}$. If we assume that the noise for each detector is a realization of a Gaussian random field, the generalized least square solution of the system of equations (3.25) is:

$$\mathbf{W} = [\mathbf{H}^{\dagger}\mathbf{C_n^{-1}}\mathbf{H}]^{-1}\mathbf{H}^{\dagger}{\mathbf{C_n}}^{-1} \tag{3.32}$$

and we have:

$$\hat{\mathbf{s}} = [\mathbf{H}^{\dagger}\mathbf{C_n^{-1}}\mathbf{H}]^{-1}\mathbf{H}^{\dagger}{\mathbf{C_n}}^{-1}\mathbf{y} = \mathbf{s} + [\mathbf{H}^{\dagger}\mathbf{C_n^{-1}}\mathbf{H}]^{-1}\mathbf{H}^{\dagger}{\mathbf{C_n}}^{-1}\mathbf{n}. \tag{3.33}$$

Again, this solution is unbiased. Although a noise contribution remains, this is the solution yielding the minimum variance error map for a deterministic signal. It is also the best linear solution in the limit of large signal to noise ratio.

3.5.1 The Wiener solution

The Wiener filter (Wiener 1949) has originally been designed to filter time series in order to suppress noise, but has been extended to a large variety of applications since then. Wiener's solution requires additional information regarding the spectral content of the original signal and of the noise. Both the noise and the signal are considered as stochastic processes with known spectral statistics (or correlation properties), contrarily to the least square solution which considers the noise only to be stochastic, the signal being deterministic. The reconstruction matrix for the Wiener Filter is:

$$\mathbf{W} = [{\mathbf{H}^{\dagger}\mathbf{C_n}}^{-1}\mathbf{H} + {\mathbf{C_s}}^{-1}]^{-1}{\mathbf{H}^{\dagger}\mathbf{C_n}}^{-1}, \tag{3.34}$$

where $\mathbf{C_n}$, as before, is the second-order statistics of the noise and $\mathbf{C_s}$ of the signal. An interesting aspect of the Wiener filter is that:

$$\hat{\mathbf{s}} = [\mathbf{H}^\dagger {\mathbf{C_n}}^{-1} \mathbf{H} + {\mathbf{C_s}}^{-1}]^{-1} \mathbf{H}^\dagger {\mathbf{C_n}}^{-1} \mathbf{y} \quad (3.35)$$

$$= [\mathbf{H}^\dagger {\mathbf{C_n}}^{-1} \mathbf{H} + {\mathbf{C_s}}^{-1}]^{-1} \mathbf{H}^\dagger {\mathbf{C_n}}^{-1} \mathbf{H}\, \mathbf{s} \quad (3.36)$$

$$+ [\mathbf{H}^\dagger {\mathbf{C_n}}^{-1} \mathbf{H} + {\mathbf{C_s}}^{-1}]^{-1} \mathbf{H}^\dagger {\mathbf{C_n}}^{-1}\, \mathbf{n}. \quad (3.37)$$

The matrix in front of $\mathbf{s}$ is not the identity, and thus the Wiener filter does not give an unbiased estimate of the signals of interest. Diagonal terms may be different from unity. In addition, non-diagonal terms may be non-zero, which means that the Wiener filter allows some residual foreground to be present in the final CMB map. The objective of this filter is to minimize the variance of the residuals, irrespective of whether these residuals originate from instrumental noise or from astrophysical foregrounds.

As noted in Tegmark & Efstathiou (1996), the Wiener solution can be debiased by multiplying the Wiener matrix by a diagonal matrix removing the impact of the filtering. This debiasing is desiderable for subsequent power spectrum estimation on the reconstructed CMB map. This, however, destroys the the minimal variance property and can increase the noise considerably.

3.5.2 The Maximum Entropy Method

The Wiener filter provides the best (in terms of minimum-variance, or maximum likelihood) estimate of the component maps under the hypothesis that the components and the noise are Gaussian stationary random processes. However, the sky is known to be neither Gaussian, nor stationary, with the possible exception of the CMB. The Maximum Entropy Method (MEM) performs component separation exploiting the same prior information as the WF (mixing matrix, sources and noise second-order statistics). However, non-Gaussian probability distributions are assumed for the sources (Hobson et al. 1998). To discuss this aspect, it is convenient to treat both WF and MEM in a Bayesian framework.

Bayes' theorem states that, given an hypothesis H and some data D, the posterior probability $\Pr(H|D)$ is the product of the likelihood $\Pr(D|H)$ and the prior probability $\Pr(H)$, normalized by the evidence $\Pr(D)$. In the case of the component separation problem (3.25), both WF and MEM uses as estimator $\hat{\mathbf{s}}$ of the signal vector the one which maximizes the posterior probability

$$\Pr(\mathbf{s}|\mathbf{x}) \propto \Pr(\mathbf{x}|\mathbf{s}) \Pr(\mathbf{s}) \quad (3.38)$$

where $\Pr(\mathbf{x}|\mathbf{s})$ is the likelihood and $\Pr(\mathbf{s})$ is the prior. The two techniques exploit the same likelihood function but a different prior.

In the following let us suppose that we are working in Fourier space, so that we can consider each Fourier mode $\mathbf{k}$ separately (see § 3.5.3). If the instrumental noise on each frequency channel is Gaussian distributed, then for each Fourier mode the probability distribution of the N_d-component noise vector $\mathbf{n}$ is described by a N_d-dimensional multivariate Gaussian. Assuming the expectation value of the noise to be zero at each observing frequency, the likelihood is given by

$$\Pr(\mathbf{x}|\mathbf{s}) \propto \exp(\mathbf{n}^\dagger {\mathbf{C_n}}^{-1}\mathbf{n}) \propto \exp[-(\mathbf{x}-\mathbf{Hs})^\dagger {\mathbf{C_n}}^{-1}(\mathbf{x}-\mathbf{Hs})]. \tag{3.39}$$

We note that the argument of the exponential function in eq. (3.39) is simply the χ^2 misfit statistics. If we assume that the emission due to each physical component is well approximated by a Gaussian random field, the prior has the form

$$\Pr(\mathbf{s}) \propto \exp(-\mathbf{s}^\dagger {\mathbf{C_s}}^{-1}\mathbf{s}). \tag{3.40}$$

It can be shown that by maximizing the posterior probability (3.38) the estimate $\hat{\mathbf{s}}$ of the signal $\mathbf{s}$ is

$$\hat{\mathbf{s}} = [\mathbf{H}^\dagger {\mathbf{C_n}}^{-1}\mathbf{H} + {\mathbf{C_s}}^{-1}]^{-1}\mathbf{H}^\dagger {\mathbf{C_n}}^{-1}\mathbf{x}, \tag{3.41}$$

which is the Wiener solution.

Once we drop the Gaussian hypothesis, we have to find an appropriate form for the prior. Ideally, one would like to assign priors for the various physical components by measuring empirically the probability distribution of temperature fluctuations from numerous realizations of each component. However, this is not feasible in practice. An alternative possibility is to use the entropic prior, which is based on information theoretic considerations. The concept of entropy in information is based on the idea that whenever there is some choice to be made about the distribution function of a random variable, one should choose the least informative option possible, which corresponds to the one having maximum entropy. In this case the prior probability takes the form (Skilling 1989)

$$\Pr(\mathbf{h}) \propto \exp[\alpha \mathrm{S}(\mathbf{h}, \mathbf{m})], \tag{3.42}$$

where $\mathbf{h}$ is the signal to be reconstructed, which defaults to the model $\mathbf{m}$ in absence of any data. The function $S(\mathbf{h}, \mathbf{m})$ is the cross entropy of $\mathbf{h}$ and $\mathbf{m}$ and the dimensional constant α may be considered as a regularization parameter.

The reason why we have used the signal vector $\mathbf{h}$ instead of the source vector $\mathbf{s}$ is that one of the fundamental axioms of the MEM is that the individual elements of the images to be reconstructed should be uncorrelated. However, this is not in general true for the astrophysical components. Thus, it is convenient to work, instead of with the source vector $\mathbf{s}$, with a vector $\mathbf{h}$ given by

$$\mathbf{s} = \mathbf{L}\mathbf{h}, \tag{3.43}$$

where $\mathbf{L}$ is the $N_c \times N_c$ lower triangular matrix obtained by performing a Cholesky decomposition of the signal covariance matrix. It can be shown that the components of $\mathbf{h}$ we just defined are a priori uncorrelated, thus satisfying the MEM axiom.

In standard application of the MEM, the image $\mathbf{h}$ is taken to be a positive additive distribution. Nevertheless, the MEM approach can be extended to images that are both positive and negative values by considering them to be the differences of two positive additive distributions, so that

$$\mathbf{h} = \mathbf{u} - \mathbf{v}, \tag{3.44}$$

where $\mathbf{u}$ and $\mathbf{v}$ are the positive and negative part of $\mathbf{h}$ respectively. In this case, the cross entropy is given by (Hobson & Lasenby 1998)

$$S(\mathbf{h}, \mathbf{m}_u, \mathbf{m}_v) = \sum_{j=1}^{L} \{\psi_j - m_{uj} - m_{vj} - h_j \ln[\frac{\psi_j + h_j}{2m_{uj}}]\}, \tag{3.45}$$

where $\psi = [h_j^2 + 4m_{uj}m_{vj}]^{1/2}$ and $\mathbf{m}_u$ and $\mathbf{m}_v$ are separate models for each positive additive distribution. The global maximum of the cross entropy occurs at $\mathbf{h} = \mathbf{m}_u - \mathbf{m}_v$. Once also the likelihood function has been expressed as a function of $\mathbf{h}$, the posterior probability becomes

$$\Pr(\mathbf{h}|\mathbf{x}) \propto \exp\{-[(\mathbf{x} - \mathbf{HLh})^\dagger \mathbf{C_n}^{-1}(\mathbf{x} - \mathbf{HLh})] + \alpha \mathrm{S}(\mathbf{h}, \mathbf{m_u}, \mathbf{m_v})\}. \tag{3.46}$$

The MEM solution in terms of $\mathbf{h}$ is given by maximizing this posterior probability; the signal vector $\mathbf{s}$ is then obtained trough (3.43).

3.5.3 Implementation details

The simple inversion of $\mathbf{H}$ using the inverse or pseudo-inverse can be implemented equivalently with any representations of the maps. The result in terms of separation is independent on this choice, as far as the representation arises from a linear transformation.

WF and MEM approaches, such as the generalized least square solution, are almost always implemented in the Fourier or harmonic space. This has a big computational advantage. In fact, for these methods we need the second-order statistics $\mathbf{C}$ of noise and, for WF and MEM, signal. Those are given by $\mathbf{C} = \{C_{ij}(p_i, p_j)\}$ in pixel space and $\mathbf{C} = \{C_{ij}(l_i, m_i, l_j, m_j)\}$ in the harmonic domain. While in pixel space the elements C_{ij} are in general non null for $i \neq j$, in Fourier or harmonic domain the covariance between distinct modes vanishes. In this case, the full covariance matrix consists in a set of independent covariance matrices (one per mode) each of which is of size $N_d \times N_d$ for $\mathbf{C_n}$ and $N_c \times N_c$ for $\mathbf{C_s}$. This means that in the conjugate space the matrix inversion can be performed for each mode independently, without the need on inverting big systems. In the following, we assume a Fourier or harmonic implementation for WF and MEM, unless the contrary is explicitly stated.

3.5.4 Recent work

Recent work on non-blind component separation methods mainly aims at reducing the strength of the prior information which is required. In particular this work refers to MEM and can be extended to WF. As previously explained, those methods require the knowledge of the mixing matrix $\mathbf{H}$, and of the noise and source power spectra $\mathbf{C_n}$ and $\mathbf{C_s}$.

While the noise power spectra can be computed with simulations once the instrumental characteristics are known, the source covariance structure is very uncertain. As shown in Hobson et al. (1998) and Stolyarov et al. (2002), the algorithm can be iterated from some initial guess for the foreground covariance

structure until convergence is obtained for the separated component maps and their power spectra. The effectiveness of this method is illustrated in Hobson et al. (1998), in which the initial starting guess for the foreground covariance structure assumes no correlations between the components and white-noise power spectrum for each component scaled to give the correct rms. The accuracy of resulting separated maps and their power spectra were found to be only slightly poorer than for those obtained assuming full covariance information in advance.

The frequency behavior of the foregrounds is also a major factor influencing the separation results. In Hobson et al. (1998) and Stolyarov et al. (2002), uncertainties in the spectral indices are accomodated by the introduction of several components for each astrophysical source in the separation process. However the ultimate limit to the number of components which can be assumed in the data is given by the number of the experimental channels.

Stolyarov et al. (2005) address other two important issues in harmonic-space MEM component separation, namely, the anisotropy of noise and foreground spectral parameters. In this work a method is proposed and tested to take spatial variability of the noise properties into account. Moreover they suggest that incomplete maps containing cuts can be considered as an extreme case of varying noise rms. One approach is to assume that the noise RMS for pixels in the cut is formally infinite or, equivalently, that they have zero statistical weight. This technique can in principle be applied to analyse arbitrarily shaped regions on the celestial sphere.

Stolyarov et al. (2005) also find that, once the average value of the spectral parameters of a foreground component is known, the harmonic-space algorithm can be extended to take into account the effect of their spatial variation. In particular, the authors suggest to expand the emission law of the spatially varying component in series around the mean value of the parameter. Each term is then treated in the separation process as the spectral behavior of an additional component. This method proved to significantly reduce the reconstruction errors even when the spatial variations are accounted for only up to first order in the expansion.

3.6 Blind methods

This is a class of methods, recently developed, which allow us to recover the components without assuming the knowledge of the mixing matrix. In the last fifteen years, blind component separation has been a very active area of research in the signal processing community where it goes by the name of Blind Source Separation (BSS) and Independent Component Analysis (ICA). For these methods the constraint on the mixing matrix is replaced by a statistical constraint: in particular, the components are assumed to be statistically independent. Coming back to the linear inversion solution of eq. (3.26), the idea is to determine the reconstruction matrix $\mathbf{W}$ in such a way that the entries of vector $\hat{\mathbf{s}} = \mathbf{W}\mathbf{x}$ are independent (or as independent as possible). The main difficulty is to define a

measure of independence, as the simple decorrelation condition

$$\frac{1}{n_p}\sum_{p=1}^{n_p}\hat{s}_i(p)\hat{s}_j(p) = 0 \;\; ; 1 \leq i \neq j \leq N_c \tag{3.47}$$

is not sufficient. In fact, this relation is symmetric, so it provides only $n(n-1)/2$ constraints instead of the n^2 required to determine $\mathbf{W}$ uniquely. Thus, more expressive forms of independence must be used.

The historical approach to blind component separation has been to determine a separating matrix $\mathbf{W}$ in order to obtain non-linear decorrelations, which, for zero-mean signals, writes:

$$\frac{1}{n_p}\sum_{p=1}^{n_p}\psi_i(\hat{s}_i(p))\hat{s}_j(p) = 0 \;\; ; 1 \leq i \neq j \leq N_c, \tag{3.48}$$

where $\hat{s}_i$ and $\hat{s}_j$ are any two candidate components, p is the pixel index and the functions ψ_i are N_c non-linear functions.

Another approach is to look for localized decorrelation, in the sense of solving:

$$\frac{1}{n_p}\sum_{p=1}^{n_p}\frac{\hat{s}_i(p)\hat{s}_j(p)}{\sigma_{ip}^2} = 0 \;\; ; 1 \leq i \neq j \leq N_c, \tag{3.49}$$

where for each component i $\{\sigma_{ip}\}_{p=1}^{n_p}$ is a sequence of positive numbers.

In both cases the symmetry of the simple decorrelation condition is broken and the required number of constraints is obtained. The main reason why the conditions expressed above are exploited instead of any other form is that these two conditions actually characterize the maximum likelihood estimate of $\mathbf{W}$ in simple and well-understood models. This allows us to understand the algorithm and to have a guidance for choosing the the non-linear functions ψ_i in eq. (3.48) and the σ_{ip}^2 in eq. (3.49).

3.6.1 FastICA

One popular algorithm based on non-linear decorrelation is FastICA (Hyvarinen 1999), which has been developed for CMB data reduction by Baccigalupi et al. (2000) and Maino et al. (2002). This approach assumes that:

1. the components of vector $\mathbf{s}$ are independent random processes;
2. the components of vector $\mathbf{s}$, save at most one, have non-Gaussian distributions.

The latter is actually the case, because the distribution of CMB fluctuations is Gaussian, while foregrounds are highly non-Gaussian. Nevertheless, in the case of harmonic space implementation, performances may suffer from the fact that in this domain the sources tend to be more Gaussian than the original pixel-domain maps. For this reason, this method is conveniently implemented in pixel domain.

Given the hypothesis of independent sources, the algorithm maximizes a measure of independence among the components based on non-Gaussianity. As a result of the central limit theorem, a variable resulting from a mixture of independent variables is more Gaussian than the original variables themselves. This means that finding a transformation such that the Gaussianity of the variables is reduced is equivalent to finding a set of transformed variables that are more independent than the original ones.

A strategy to find maximally non-Gaussian transformed variables is to select a suitable measure of non-Gaussianity and then maximize it for the operator $\mathbf{W}$. This approach can be shown to be equivalent to finding components which cancel non-linear correlations in the sense of eq. (3.48). In principle the non-linear decorrelation do not take the noise into account; however, it is possible to find a measure of non-Gaussianity which allows us to adopt computing strategies that are robust against noise. For example, an approximation to the neg-entropy function has been proposed Hyvarinen (1999) which allow us to deal with noise, at least as long as it can be approximated by a Gaussian distribution with known covariance function and it is uniformly distributed over the sky.

The algorithm requires a preprocessing step (Hyvarinen 1999), where the data are "quasi whitened". In particular, the algorithm works, instead that with the data vector $\mathbf{x}$, with

$$\hat{\mathbf{x}} = \sqrt{\mathbf{C_x} - \mathbf{C_n}}\mathbf{x}, \tag{3.50}$$

where $\mathbf{C_n}$ is the covariance of noise (assumed to be known) and $\mathbf{C_x}$ the covariance of the zero mean data (computed over the sets of pixels).

To derive some property of the solution, with no loss of generality, we can assume $N_d = N_c$ and $\mathbf{W}$ as a robust estimate of $\mathbf{H^{-1}}$. In this case, we find the same results of the simple inversion solution [eq. (3.29)]: the noise term $\mathbf{H^{-1}n}$ can strongly affect the high spatial frequency components. This is due to the fact that no filtering of the noise is performed. However, nothing prevents to adopt some regularization strategy after the separation process.

Once the separation matrix $\mathbf{W}$ has been found, physical normalization, frequency scalings and offsets of each independent component in the data can in principle be reconstructed. Furthermore, it is possible to derive the signal-to-noise ratio in the reconstructed map. This is a useful tool when, for example, the number of underlying components is not known a priori. If a spurious component is still present in the final maps, this would result in a S/N or the order, or below, unity.

3.6.2 Spectral matching ICA (SMICA)

This technique, proposed by Belouchrani et al.(1997) and developed for CMB studies by Delabrouille et al. (2002), is based on spectral statistics, which are binned auto- and cross-spectra of the data. Thus, this method essentially exploits second-order statistics. This is a constraint weaker than imposing statistical independence, which in principle requires to nullify the non-diagonal terms of all statistical orders. Thus, solving the problem in general requires the use of other constraints, which can be chosen depending on the problem.

More specifically, if $\mathbf{x}(\ell, m)$ is the N_d vector of the harmonic coefficients of data for each mode (ℓ, m), its empirical covariance matrix is given by:

$$\hat{\mathbf{C}}_{\mathbf{x}}(\ell) = \frac{1}{2\ell+1} \sum_{m=-\ell}^{m=+\ell} \mathbf{x}(\ell, m)\mathbf{x}(\ell, m)\dagger \,. \tag{3.51}$$

These covariances are then binned. In the simplest case, we define Q top-hat bins, where the q-th frequency bin contains frequencies between ℓ_q^{min} and ℓ_q^{max}. We then consider the binned spectra:

$$\hat{\mathbf{C}}_{\mathbf{x}}(q) = \frac{1}{P_q} \sum_{\ell=\ell_q^{min}}^{\ell=\ell_q^{max}} (2\ell+1)\mathbf{C}_{\mathbf{x}}(\ell) \tag{3.52}$$

where $P_q = \sum_{\ell=\ell_q^{min}}^{\ell=\ell_q^{max}} (2\ell+1)$ is the number of modes summed together for a single q. The mixture model (3.25) predicts that the empirical spectra $\hat{\mathbf{C}}_{\mathbf{x}}(q)$ have an expected value

$$\mathbf{C}_{\mathbf{x}}(q) = \mathbf{H}\mathbf{C}_{\mathbf{s}}(q)\mathbf{H}\dagger + \mathbf{C}_{\mathbf{n}}(q), \tag{3.53}$$

where $\mathbf{C}_{\mathbf{s}}(q)$ is the binned covariance matrix for the components in bin q and $\mathbf{C}_{\mathbf{n}}(q)$ is the same for noise. The unknown parameters can be collected in a big vector θ

$$\theta = \{\mathbf{H}, \{\mathbf{C}_{\mathbf{s}}(q)\}, \{\mathbf{C}_{\mathbf{n}}(q)\}\}. \tag{3.54}$$

In practice, however, not all the elements of this vector are estimated: many constraints can be imposed on θ. A typical choice is to assume that the components are uncorrelated between themselves and that the noise is uncorrelated between channels. Such a choice would result in a smaller parameter set, as non-diagonal terms of $\mathbf{C}_{\mathbf{s}}(q)$ and $\mathbf{C}_{\mathbf{n}}(q)$ are null. Other options are possible, both more stringent (like assuming that the noise in each channel is a smooth function of the bin index q) or less stringent (like assuming that some components may not be uncorrelated).

SMICA determines the set of unknown parameters θ by minimizing the spectral mismatch between the empirical covariance matrices and the model (3.53)

$$\phi(\theta) = \sum_q P_q D(\hat{\mathbf{C}}_{\mathbf{x}})(q), \mathbf{C}_{\mathbf{x}})(q; \theta), \tag{3.55}$$

where $D(\cdot, \cdot)$ is a measure of divergence between the two matrices. The reason for choosing this particular form of mismatch is that it corresponds to maximum likelihood estimation in a stationary model, and thus it has good statistical properties. After the minimization, the solution is an estimate of the mixing matrix $\mathbf{H}$ and of the binned source and noise power spectra $\mathbf{C}_{\mathbf{s}}(q)$ and $\mathbf{C}_{\mathbf{n}}(q)$. Thus, we have not yet the recovered components; however, we note that the estimated quantities allow us to perform a component separation with a non-blind method like WF or MEM.

3.6.3 Parameter estimation

This method has been first proposed by Brandt et al. (1994) and developed by Eriksen et al. (2006). It is a blind method, in the sense that it does not require the prior knowledge of the frequency scaling of the components, nor of their power spectra. However, it is very different from the methods we described by now, as it does not use any information on the spatial correlation of sources. Indeed, this is a standard parameter estimation technique which assumes a parametric spectral model for each component and fit the corresponding parameters pixel by pixel. The pixel by pixel fit implies that both noise and sources are assumed to be uncorrelated between pixels. This is known to be not strictly valid, as sources has intrinsic spatial autocorrelation and noise can be considered to be uncorrelated between pixels only as far as no smoothing process has been applied. However, such a process is necessary in order to equalize the beam function between different channels. Nevertheless, the pixel by pixel fit has also the big advantage that no restrictions are made on the spatial variability of the spectral indices or of the noise variances.

In details, each of the components which are assumed to be mixed in the data is parametrized by a small number of free parameters θ. For instance, these can be an amplitude A and a spectral index β for the model $S = A(\nu/\nu_0)^\beta$. The total number of parameters cannot be higher than the number of frequencies, otherwise the problem is degenerate. For each pixel, the set of free parameters are determined performing a maximum likelihood, which, since the noise is assumed to be Gaussian distributed, reduces to χ^2. Thus, the results can be monitored by a goodness-of-fit test, and reliable error estimates can be derived.

The likelihood function can be computed with different numerical techniques, as grid computation, MCMC and non-linear searches. Whereas Brandt et al. (1994) relied exclusively on non-linear fitting, and was therefore quite unstable with respect to noise, Eriksen et al. (2006) exploits MCMC, which makes the algorithm both more robust and also produce accurate errors. The drawback is that MCMC is computationally demanding, as it requires around 100 seconds per pixel. However, a full MCMC analysis is required only for estimating non-linear parameters, such as spectral indices or dust temperatures. If all parameters are linear, like component amplitudes, an analytical computation is equally good. The proposed approach is then to perform the analysis is two steps:

1. Fit for all the parameters with MCMC on low-resolution maps. This allows us to reduce the number of pixels to save computational time.

2. Fit only for the component amplitudes with analytic computation or Gibbs sampling on high-resolution maps, while the non-linear parameters are fixed at the corresponding low-resolution values.

This strategy is based on the assumption that spectral indices vary more slowly on the sky than amplitudes.

3.6.4 The Correlated Component Analysis (CCA)

The CCA is a novel technique, proposed by Bedini et al. (2005). This method has been developed and tested for the PLANCK mission by Bonaldi et al. (2006) and applied to WMAP data by Bonaldi et al. (2007a). Work on this technique constitutes a major part of this Thesis, and will be described in details in the next Chapters. In this section, we present only a general description of the method.

As previously explained, the assumption that components are mutually independent, once conveniently formulated, is sufficient to determine the reconstruction matrix $\mathbf{W}$ and solve the component separation problem. This assumption is certainly satisfied for the CMB, which is statistically independent from foregrounds. However, Galactic emissions are tightly correlated to each other, so that the assumption of mutual independence breaks down. Bedini et al. (2005), like Belouchrani et al. (1997), exploited second-order statistics and the physically plausible assumption of a significant spatial autocorrelation of the individual sources. However, at variance with previous work, they gave up the assumption of mutually uncorrelated sources. By exploiting a parametric knowledge of the mixing matrix, they succeeded in estimating both the mixing matrix and the relevant cross-covariances.

The method proposed by Bedini et al. (2005) works in pixel domain. Given a generic signal $\mathbf{X}$, defined in a two dimensional space with coordinates (ξ, η), its covariance matrices are defined by:

$$\mathbf{C_x}(\tau, \psi) = \langle [\mathbf{X}(\xi, \eta) - \mu][\mathbf{x}(\xi + \tau, \eta + \psi) - \mu]^T \rangle, \tag{3.56}$$

where $\langle ... \rangle$ denotes expectation under the appropriate joint probability distribution, μ is the mean vector and the superscript T means transposition. Every covariance matrix is characterized by the shift pair (τ, ψ), where τ and ψ are increments in the ξ and η coordinates.

From eq. (3.25) we can easily derive a relation between the data covariance matrix $\mathbf{C_x}$ at a certain lag, the source covariance matrix $\mathbf{C_s}$ at the same lag, the mixing matrix $\mathbf{H}$, and the noise covariance matrix $\mathbf{C_n}$:

$$\mathbf{C_x}(\tau, \psi) = \mathbf{H}\mathbf{C_s}(\tau, \psi)\mathbf{H}^T + \mathbf{C_n}(\tau, \psi). \tag{3.57}$$

This relation allows us to estimate the mixing operator $\mathbf{H}$ from the covariance matrix $\mathbf{C_x}$ of the data. Note that it implicitly assumes that the source and the noise processes are stationary. This is true all across the sky for the CMB, but only within small sky regions for the foregrounds. For this reason, it is convenient to section the sky into patches within which foregrounds have approximately uniform properties, and apply the method to each patch individually.

If the noise process can be assumed to be signal-independent, white and zero-mean, for $(\tau, \psi) = (0, 0)$ $\mathbf{C_n}$ is a diagonal matrix whose elements are the noise variances in the frequency channels of the instrument, while for $(\tau, \psi) \neq (0, 0)$ $\mathbf{C_n}$ is the null $M \times M$ matrix. Anyway, if $\mathbf{C_n}$ deviates significantly from this ideal model, various methods are available to estimate the noise covariance

function: for example it can be empirically determined using noise maps from Monte Carlo simulations.

Once we have a model for $\mathbf{C_n}$, we only have to calculate $\mathbf{C_x}$ for a large enough number of nonzero shift pairs (τ, ψ) to estimate both $\mathbf{H}$ and $\mathbf{C_s}$. As already mentioned, this method exploits a parametrization of the mixing matrix to reduce the number of unknowns. We note that because of the scaling ambiguity we can normalize our mixing matrix to have all elements of a reference row equal to 1. Thus, the amplitudes of the components does not need to be estimated. Then, the models for the frequency scalings of the components may be chosen freely, and the method is therefore completely general.

The main product of CCA is an estimate of the mixing matrix. Hence this can be considered a "model learning" algorithm. Once the mixing matrix has been recovered, source separation can be performed with traditional non-blind methods, such as WF or MEM, or other Bayesian inversion techniques. Details on the implementation of the code and results of the tests with simulated data having the PLANCK specifications will be presented in Chapter 4. In Chapter 5 we will discuss our application to the three-year WMAP data.

Chapter 4

CCA: method and tests

4.1 Introduction

In this Chapter we will go in more details on the CCA component separation technique, whose basic concepts were presented in § 3.6.4.

When CCA was first proposed by Bedini et al. (2005) for component separation of PLANCK data, a lot of different techniques had been already studied and developed for the same purpose. However, as mentioned in the previous Chapter, there is not an optimal technique to solve the component separation problem. Each method exploits different characteristics of the data and has its advantages and its shortcomings. The algorithms referred to as "non-blind", like WF and MEM, assume a perfect knowledge of the frequency dependence of sources. On the other hand, the emission spectra are generally poorly known. "Blind" approaches exploiting Independent Component Analysis (ICA) techniques proved to be very effective in extracting the CMB, which is independent of all other sources. However, Galactic emissions are tightly correlated to each other, so those algorithms in general do not allow a good reconstruction of the foreground components. Another drawback is that those methods in general do not exploit some useful prior information on the components. This is an unpleasant feature, as the optimum would be to use all the information we have and blindly recover the unknowns.

CCA has been proposed as a trade-off between blind and non-blind methods, and in fact it is sometimes referred to as a semi-blind technique. It is flexible, as it assumes a parametric representation of the emission spectra but recovers the relevant foreground properties. Foregrounds are realistically treated as correlated components. The main product is an estimate of the mixing matrix, so this method can be also considered as a "model learning" algorithm. The recovered mixing matrix can be used to perform component separation with traditional non-blind methods, which have been extensively studied and in principle allow very low reconstruction errors.

After presenting the method, Bedini et al. (2006) performed extensive tests with a prototype MATLAB code working on plane sky patches. These preliminary tests proved the new approach to be successful, so we dedicated systematic work to its development and testing. In this Chapter we first describe the al-

gorithm and its FORTRAN implementation we have produced, which is suited to work with data in the standard format of the PLANCK mission. Then, we will focus on different tests of the method we performed on simulated PLANCK data.

4.2 Algorithm and code

In § 3.6.4, starting from the data model

$$\mathbf{x} = \mathbf{H}\mathbf{s} + \mathbf{n}, \tag{4.1}$$

we derived the following relation between the data covariance matrix $\mathbf{C_x}$ at a certain lag, the source covariance matrix $\mathbf{C_s}$ at the same lag, the mixing matrix $\mathbf{H}$, and the noise covariance matrix $\mathbf{C_n}$:

$$\mathbf{C_x}(\tau,\psi) = \mathbf{H}\mathbf{C_s}(\tau,\psi)\mathbf{H}^T + \mathbf{C_n}(\tau,\psi). \tag{4.2}$$

This relation is exploited by CCA to estimate the mixing operator $\mathbf{H}$ and the relevant source covariance from the covariance matrix of the data $\mathbf{C_x}$. In practice, however, we need to parameterize the mixing matrix to reduce the number of unknowns. To choose a suitable parameterization for $\mathbf{H}$ we use the fact that its elements are proportional to the spectra of astrophysical sources, of which we have some knowledge coming from the theory or from complementary observations. The main diffuse components present in the PLANCK channels are, in addition to the CMB, the Galactic dust, synchrotron and free-free emissions. The frequency dependencies of CMB and free-free are known [eqs (3.27) and (2.2)]. Conversely, the frequency scalings of synchrotron and dust are not known a priori. The simplest model compatible with observations involves only one parameter for each source, the spectral index β_s or the emissivity index β_d, respectively:

$$T_{\mathrm{A,synch}}(\nu) \propto \nu^{-\beta_s} \ , \tag{4.3}$$

$$T_{\mathrm{A,dust}}(\nu) \propto \frac{\nu^{\beta_d+1}}{\exp(h\nu/kT_{\mathrm{dust}})-1}. \tag{4.4}$$

The mixing matrix accounting for all these sources is then of four columns and of as many rows as the number of channels. We are able to parameterize the matrix $\mathbf{H}$ by exploiting eq. (3.23), where we replace f_j with the emission spectra of all the components. The free parameters of our model are β_s and β_d. Since they vary across the sky, our strategy will be to apply CCA to sky patches small enough for these indices can be assumed to be approximately constant (see § 4.4).

4.2.1 Computation of the data covariance matrix

The data covariance matrix defined by eq. (3.56) is the fundamental tool used to identify the mixing operator. If our data are sampled in P pixels, labeled with coordinates (ξ,η), we can compute an estimate of $\mathbf{C_x}$ as:

$$\hat{\mathbf{C}}_{\mathbf{x}}(\tau,\psi) = \frac{1}{P}\sum_{\xi,\eta}[\mathbf{x}(\xi,\eta)-\mu_x][\mathbf{x}(\xi+\tau,\eta+\psi)-\mu_x]^T. \tag{4.5}$$

The shift pair (τ, ψ) defines a vector that links each pixel to a shifted one. In the case of a uniformly sampled rectangular sky patch we have a very easy way to define the shift pairs (τ, ψ). We choose (ξ, η) as cartesian coordinates whose axes are parallel to the sides of the rectangle, and define a collection of N_p shifts, each of p pixels, labeled by an index n ($n = 0, 1, ..N_p - 1$): $\{\tau_n = np\mathbf{u}_\xi\}$ and $\{\psi_n = np\mathbf{u}_\eta\}$. From all the combinations of τ_n and ψ_n we get $N_p \times N_p$ shift pairs.

The data we are working with are very different from this simple case: they are patches extracted from Healpix (Górski et al. 2005) all sky maps, so they are sampled in a sphere rather than in a plane and also the grid is not regular. We note that even in the simplest case the selected region is not exactly rectangular because of the diamond shape of pixels and of the surface curvature.

To apply the method we need to map the selected patch into a geometrically identical one, shifted by (τ, ψ). This can be done only in an approximate way with the Healpix pixelization, and is easier in the equatorial region. As we will see, however, in the following we study Galactic foregrounds where they are more intense, i.e. at not too high Galactic latitudes. We therefore use Galactic coordinates and refer to the grid defined by Galactic parallels and meridians to calculate shifts.

With the Healpix ring ordering scheme, pixels with subsequent indices are subsequent in longitude, so that, for any integer p, a set of pixels $i_{\min} \leq i \leq i_{\max}$ simply map into the set $i_{\min} + p \leq i \leq i_{\max} + p$, shifted by p pixels in the longitudinal direction. The shift in latitude is trickier. We proceeded associating to each pixel the shifted one closest to having the same longitude and the latitude increased by $\Delta b = p \cdot ds$, where ds is the mean pixel size. Clearly, in this case Δb is not exactly equal for all shifted pixels. However, as we will see, our shifts are rather small, so that, if we are not too close to the Galactic poles, the approximation is sufficiently good.

To choose convenient values for the number of shifts N_p and the step p, we should care both about efficiency and conditioning. It is obvious that, if N_p is large, the method becomes computationally demanding. On the other hand, a too small N_p can make the problem ill conditioned, thus leading to a lack of convergence. The step p should be chosen in order to avoid both redundancy (if p is too small, some of the covariance matrices are nearly equal) and degeneracy (if p is too large, some covariance matrices vanish). In practice, the choice can be made empirically, for any p, by increasing N_p progressively until convergence is reached.

4.2.2 The minimization procedure

To solve eq. (4.2) and estimate the parameters that identify the mixing matrix and the source covariance matrices, we minimize the residual between the theoretical quantities based on the proposed solution and the corresponding quantities evaluated empirically from the available data. Our solution is given

by:

$$(\Gamma, \Sigma(:,:)) = \text{argmin} \sum_{\tau,\psi} \parallel \mathbf{H}(\Gamma)\mathbf{C_s}[\Sigma(\tau,\psi)]\mathbf{H}^T(\Gamma) - \hat{\mathbf{C}}_\mathbf{x}(\tau,\psi) + \mathbf{C_n}(\tau,\psi) \parallel, \tag{4.6}$$

where Γ is the vector of all parameters defining $\mathbf{H}$, and $\Sigma(:,:)$ is the vector containing all the unknown elements of the matrices $\mathbf{C_s}$ for every shift pair.

To perform the minimization, we used simulated annealing (SA, Aarts & Korst, 1989), which exploits an analogy between the way in which a metal cools and freezes into a minimum energy crystalline structure and the search for a minimum in a more general system.

The major advantage of SA over other methods is its ability to avoid becoming trapped at local minima, which can be very nasty in our case. The algorithm employs a random search which not only accepts changes that decrease the objective function f, but also some changes that increase it. The latter are accepted with a probability:

$$p = \exp(-\delta f/T), \tag{4.7}$$

where δf is an increment in f and T is a control parameter, known as the system "temperature".

Avoidance of local minima is anyway dependent on the "annealing schedule": the choice of the initial temperature, how many iterations are performed at each temperature, and how much the temperature is decreased at each step as cooling proceeds.

4.3 Tests on simulated PLANCK data

In this section we will discuss how we can characterize the performances that a certain component separation method is expected to have on PLANCK data. The concept is to perform the analysis on a data set having specific characteristics.

First, every detail of these data should be under control. In particular, we have to know the "true answers" (mixing matrix, component maps, component spectra and so on) to the problem our component separation method tries to solve. In this way, after the component separation, we can simply compute the actual errors.

Second, the data should be as similar as possible to the real data PLANCK will provide. In this way the derived performances are representative of those we will obtain with PLANCK.

We therefore need a sky simulation tool capable of generating sufficiently realistic simulated data. Such a tool has been developed within the PLANCK group and it is referred to as the "Planck sky model" (PSM). In particular, the PSM is a package to simulate the true emission of the sky at several frequencies.

4.3.1 The Planck sky model

The process of producing fake sky emissions is somewhat inverse to component separation. Given the linear mixture model of eq. (4.1) the data are obtained by

a linear combination of a certain set of components, each of which is described by a spatial template and a frequency dependence (either spatially varying or constant over the sky). The CMB is the easiest component to simulate. The frequency scaling is well known and a CMB map can be obtained by generating a Gaussian random field having a certain power spectrum, which can be constrained by the available measurements. If however we are interested also in primordial non-Gaussianity, a CMB map containing a non-Gaussian component can be simulated as explained in Liguori et al. (2007). In general the techniques exploited to generate CMB maps allow us to have different CMB realizations with identical statistical properties, which can be used to evaluate errors through Monte Carlo approaches. Alternatively, when the objective is to mimic the true CMB map observed in the sky, one can generate a constrained realization.

Unfortunately, the simulation of foreground emissions is more difficult and affected by bigger errors. In this case it is not possible to generate at random foreground maps with reliable characteristics. For the spatial template we have to rely on ancillary data mapping the emission of interest (or a certain tracer of it) at a frequency at which it is the dominant component. This map is provided with a certain recipe to scale it in frequency, which is also derived from observational constraints. Template maps have in general various problems. As we will see, they are limited on small scales by the resolution of the experiments. Moreover, some of them are obtained by a mosaic of observations, so that they have spurious structure at low multipoles. Moreover, the frequency at which the observations are made are often far from the CMB range. Assuming a spatially varying frequency scaling, the morphology of the emission can significantly change with frequency. Finally, the lack of information, especially at the frequencies of interest, often forces us to assume a constant frequency scaling which underestimates the true spatial variability. In the following we will review the models currently adopted in the PSM for the main foreground components, with special attention to diffuse ones.

Synchrotron

As synchrotron is the dominant signal at frequencies below ~ 5 GHz (at least away from the Galactic plane region), it has become standard practice to use low frequency surveys as synchrotron templates. The most commonly used template is the Haslam et al. (1998) 408 MHz map. The comparison with the Reich & Reich (1988) survey at 1420 GHz can be used to estimate the synchrotron spectral index which allows the extrapolation of the map to the frequency of interest through eq. (4.3). This was done by Giardino et al. (2002), who provided a full-sky map of synchrotron spectral indices. This synchrotron model has two main shortcomings. First, the spatial information is limited by the finite resolution of the surveys: 0.85° FWHM in the case of the 408 MHz map and 0.6° FWHM in the case of the 1420 MHz one. Then, uncertainties on the zero-level of the maps and lack of information on the spectrum at higher frequencies reduce the accuracy that can be reached in the extrapolation at CMB frequencies.

Free-free

As we already mentioned, the spectral dependence of free-free is well known. Conversely, the map of this emission is poorly known: as this astrophysical component never dominates over the other ones, it cannot be observed directly. It can be traced with hydrogen recombination emission lines, and particularly Hα emission, as both are emitted by the same ionized medium. The connection between Hα and free-free has been discussed by a number of authors (Smoot 1998; Valls-Gabaud 1998; McCullough et al. 1999). The use of Hα maps as free-free templates however is complicated by a number of factors. The most important one is that Hα emission, at variance with free-free at radio/microwave frequencies, is affected by the extinction due to dust grains. Finkbeiner (2003) assembled a full sky Hα map using data from several surveys. This map, coupled with the Schlegel et al. (1998) extinction map, is used to compute a best guess map of free-free emission (Dickinson et al. 2003)

Thermal dust

A full sky template for thermal dust is provided by the Schlegel et al. (1998) map, obtained exploiting IRAS and DIRBE data in the 1250-3000 GHz range. By comparing this data with the FIRAS data from 100 to 2100 GHz, Finkbeiner et al. (1999) provided an extrapolation of the map to microwave frequencies. Spatial variations of the infrared color have been observed, indicating that the composition of the dust in the ISM is not fixed but varies according to the changes in the size distribution. The preferred model of Finkbeiner et al. (1999) is a two-component model with fixed spectral indices and temperatures varying in the sky. The dominant component has $\langle T_d \rangle \simeq 16K$ and $\beta_d = 2.7$; the other component, whose intensity is $\sim 1/2$ of the other, has $\langle T_d \rangle \simeq 9.5K$ and $\beta_d = 1.7$. The tentative interpretation is that the first component is constituted by carbonaceous grains, the second by amorphous silicates. Over limited frequency ranges, however, also a one temperature model, having $\langle T_d \rangle \simeq 18K, \beta_d = 1.67$, can be a good fit of the data.

Anomalous dust emission

This component is still poorly known and it has been included in the PSM only recently. Given the lack of observational information on the anomalous emission, the model is essentially based on theoretical models. However, the available observational constraints are exploited to validate the theoretical results.

The model exploits the Schlegel et al. (1998) thermal dust map, which is expected to be highly correlated with the anomalous component. This map is then modulated by the temperature of the dust, which is proportional to the dust reddening, to obtain a template for the anomalous emission. For the frequency scaling it uses a Draine & Lazarian (1998) model with an amplitude scaled to fit the results on the anomalous emission by Davies et al. (2006). Also the results of the analysis on the WMAP data performed by Bonaldi et al. (2007a) were taken into account, as we will better explain in the next Chapter.

Extragalactic foregrounds

The simulation of point sources and SZ signals exploits all the available catalogs of the considered class of sources, together with a recipe to scale each source in frequency. The latter is not an issue for SZ clusters, whose frequency behavior is well known. Conversely, in the other cases the extrapolation in frequency can be very uncertain. Radio sources are particularly nasty: as we already mentioned, they can have steep, flat, peaked or inverted spectra. Even if a spectral index can be obtained by comparing the flux emitted at two frequencies, there is no guarantee that it is still reproducing the spectral behavior of the source in another frequency range. For an explanation on how this problem is addressed in the PSM, see Massardi (2006).

4.3.2 Predicting the instrumental response

When constructing a simulated data set, besides the simulation of the sky emission, described in the previous section, we have also to mimic the instrumental response. This step is easier in principle, as the instrumental characteristics should be known to higher accuracy than foregrounds emission properties. However, a detailed simulation of the instrumental response requires highly demanding in computational time. Thus, in most cases only a simplified simulation is performed, which however is not able to reproduce all the characteristics or real data.

For a satellite mission like PLANCK, the observation is a stream of measurements as a function of time (time ordered data, TOD) taken by the detectors as the instrument moves along its orbit. After the satellite has completed a full scanning of the sky, the data can be arranged in a sky map through a process called mapmaking. The simulation of the TOD and of the effect of mapmaking is very difficult to do, so generally the simulated data for component separation purposes are directly generated in the map domain. This of course does not allow the inclusion of a lot of systematic effects which are actually present in real data.

The simulation in the image domain is much easier to do, as one simply considers a set of fake sky maps obtained as described previously and processes them to simulate the instrumental response. In this case, there are mainly three steps to be performed:

1. Each detector integrates the information over a frequency band, so that the final map is a superposition of different images weighted by the frequency response function;

2. The image received by each detector is convolved by the instrumental beam, setting the resolution of the observed map;

3. Each detector adds noise to the observation. The variance of the noise for each pixel is proportional to N_{obs}^{-1}, where N_{obs} is the number of independent observations made by the satellite on a certain direction of the sky.

Depending on the purpose of the simulation, various approximations of the previous steps are adopted. In particular, most of the simulations for testing

component separation methods assume Gaussian (or at least circularly symmetric) beams instead of realistic beams. The frequency response of each detector is often approximated as a Dirac delta or a top-hat function. Finally, sometimes we assume Gaussian noise with uniform variance over all the sky.

In sections 4.4 and 4.5 we will describe the characteristics and the results of two different tests we performed on the CCA method. As we will see, these tests have different purposes, implying a different level of sophistication in the simulations.

4.4 CCA quality tests

In the following we describe the first tests of the CCA method. The aim was to evaluate the performances of the method and define suitable strategies for its exploitation in the data analysis of PLANCK. We considered simulated observations of the microwave sky with angular resolution and white stationary noise at the nominal levels for the PLANCK satellite, and realistic foreground emissions, with a position dependent synchrotron spectral index. Point sources were not considered in this work, hence this test holds only on relatively large scales ($\ell \leq 400$) where point sources have a minor effect.

4.4.1 Data set

For this set of tests we used the specifications of the PLANCK mission reported in Table 4.1. The simulated sky contains: a) synchrotron emission as modeled by Giardino et al. (2002), allowing for a spatially varying spectral index; b) thermal dust emission (Finkbeiner et al. 1999), with dust at two temperatures and two emissivity indices; c) free-free traced by the $H\alpha$ emission (Dickinson et al. 2003) and corrected for dust absorption based on the 100 μm maps from Schlegel et al. (1998); d) a CMB Gaussian realization corresponding to the best fit WMAP theoretical power spectrum from first year data. We produced 100 sets of Monte Carlo simulated maps in the PLANCK channels, with different realizations of the CMB and of Gaussian noise.

To test the CCA ability to recover the spectral parameters of foregrounds, we used the PLANCK channels from 30 to 143 GHz. The resolution of all the maps had to be degraded to that of the 30 GHz channel ($33'$). To test the performances achievable with the full PLANCK resolution of $5'$, we repeated the analysis with the high frequency channels from 217 to 545 GHz, where the sources to account for are only CMB and dust.

The noise maps we initially added to each channel were Gaussian (with the RMS levels reported in Table 4.1) and uncorrelated: in this case, the only noise term in eq. (4.2) is $\mathbf{C_n}(0,0)$, which is a diagonal matrix whose elements are the noise variances for each channel. The smoothing process applied to degrade the channels to the 30 GHz resolution not only changes the noise variances, but also introduces noise correlation, so in principle the terms $\mathbf{C_n}(\tau,\psi)$ do not vanish for $(\tau,\psi) \neq (0,0)$. Nevertheless, we carried out our tests assuming uncorrelated Gaussian noise: we then consider only the diagonal matrix $\mathbf{C_n}(0,0)$, whose elements are the variances measured after smoothing each noise map to the $33'$

Table 4.1: PLANCK specifications. We assume spatially uniform Gaussian noise at the mean level expected for the nominal mission (14 months).

Center frequency (GHz)	30	44	70	100	143	217	353	545	857
Angular resolution (arcmin)	33	24	14	9.5	7.1	5.0	5.0	5.0	5.0
Rms pixel noise $\Delta T^\star$	5.5	7.4	12.8	6.8	6.0	13.1	40.1	401	18291

$\star$ Noise levels are in μK thermodynamic

resolution. This approximation is not the best we could do in dealing with noise, but it was purposely adopted to investigate the effect of errors on noise modeling.

The low frequency channels (LF) set

The LF set includes 5 PLANCK channels, centered at 30, 44, 70, 100, and 143 GHz. Since we have 4 sources (CMB, synchrotron, free-free, and thermal dust) the mixing matrix has 4 columns and we want to recover the synchrotron and the dust spectral indices. Since all the maps have been degraded to a resolution of $33'$, we operate with the Healpix parameter NSIDE=512, corresponding to a pixel size of about 7'.

The number of shifts allowing a good conditioning of the problem is found to be $N_p = 5$. The value of N_p and the pixel size constrain the amplitude of the shifts that can be used to calculate the covariance matrices: the minimum shift must correspond to one pixel ($\sim 0.1°$); the maximum one cannot generally exceed $1°$ to ensure that all covariance matrices are non-null. We chose $p = 4$, which corresponds roughly to our beam size.

As mentioned above, we apply our method to sky patches in order to neglect the spatial variations of the synchrotron spectral index. To have sufficient statistics, the number of pixels per patch has to be at least $\simeq 10^5$. With the adopted pixel size, this corresponds to a patch area of $1500\,\mathrm{deg}^2$, which is not optimal for the reconstruction of the spectral indices that may vary widely with the position. In the synchrotron template we use here (Giardino et al. 2002), 10% variations occur on scales of about 10 degrees.

We used patches of $(\Delta l, \Delta b) = (50°, 30°)$ for the lowest latitudes and increased the longitudinal dimension for higher latitudes to roughly preserve the patch area. We sectioned the sky with patches centered at longitudes $l_c = \{0°, 40°, 80°, ...320°\}$ and increasing latitudes. In total we analyzed the $\sim 80\%$ of the sky with $|b| < 55°$.

From the first tests we learned that to get a good spectral index reconstruction we need a broad frequency range. This can be achieved by taking into account additional information from other surveys. To this end, we included in our analysis the 857 GHz PLANCK map and the Haslam et al. (1982) 408 MHz map, taken as dust and synchrotron templates, setting to 0 all the elements of the mixing matrix except the synchrotron one at 408 MHz, and the dust one at 857 GHz.

The high frequency channels (HF) set

In the PLANCK 217, 353 and 545 GHz channels we can neglect the synchrotron and free-free emissions, so that we are left with CMB and dust, and the only parameter to recover is the dust emissivity index β_d. These channels allow us to work at the best PLANCK resolution: the beam is of $5'$, so we can use NSIDE=2048, corresponding to a pixel size of about 1'.7. We dissected the sky into patches of size $(\Delta l, \Delta b) = (20°, 20°)$, centered at longitudes $l_c = \{0°, 20°, 40°, ...340°\}$ and latitudes $b_c = \{0°, \pm 10°, \pm 20°, \pm 40°, \pm 60°\}$. In total, we then analyzed $\sim 85\%$ of the sky.

In this case, we did not need to include other channels to help reconstructing the mixing matrix. We used a shift step $p = 5$, corresponding to an angular size of 0.14°, and $N_p = 3$.

4.4.2 Estimation of the mixing matrix

Since, on purpose, the parameters to be determined do not directly reflect those defining the sky model, the errors on our estimates cannot be simply derived comparing our results with the "true" values, simply because the latter in general do not exist. In particular, the synchrotron spectral index is varying in the sky, and the dust emission is modeled by a two-component spectrum, so they need to be treated as we describe below.

The output of our method is the estimated mixing matrix normalized at a reference frequency ν_0. The elements of the mixing matrix corresponding to synchrotron and dust at frequency ν_d are:

$$h_{\rm out}({\rm syn}, \nu_d) = \left(\frac{\nu_d}{\nu_0}\right)^{-\beta_s}, \tag{4.8}$$

$$h_{\rm out}({\rm dust}, \nu_d) = \left(\frac{\nu_d}{\nu_0}\right)^{\beta_d+1} \frac{\exp(h\nu_0/kT_{\rm dust}) - 1}{\exp(h\nu_d/kT_{\rm dust}) - 1}, \tag{4.9}$$

which were derived from eqs. (4.3) and (4.4). These quantities correspond to the mean ratios of synchrotron and dust intensities at frequencies ν_0 and ν_d, within the considered patch in the simulated sky:

$$h_{\rm in}({\rm syn}, \nu_d) = \left(\frac{\nu_d}{\nu_0}\right)^{-\overline{\beta}_s}, \tag{4.10}$$

$$h_{\rm in}({\rm dust}, \nu_d) = \left(\frac{\nu_d}{\nu_0}\right)^{\overline{\beta}_d+1} \frac{\exp(h\nu_0/kT_{\rm dust}) - 1}{\exp(h\nu_d/kT_{\rm dust}) - 1}. \tag{4.11}$$

The "observed" indices $\overline{\beta}_s$ and $\overline{\beta}_d$ are now directly comparable with the derived indices β_s and β_d. We then define our errors as:

$$\Delta\beta_s = \left| \frac{\log(h_{\rm out}({\rm syn}, \nu_d)/h_{\rm in}({\rm syn}, \nu_d))}{\log(\nu_d/\nu_0)} \right|, \tag{4.12}$$

$$\Delta\beta_d = \left| \frac{\log(h_{\rm out}({\rm dust}, \nu_d)/h_{\rm in}({\rm dust}, \nu_d)}{\log(\nu_d/\nu_0)} \right|. \tag{4.13}$$

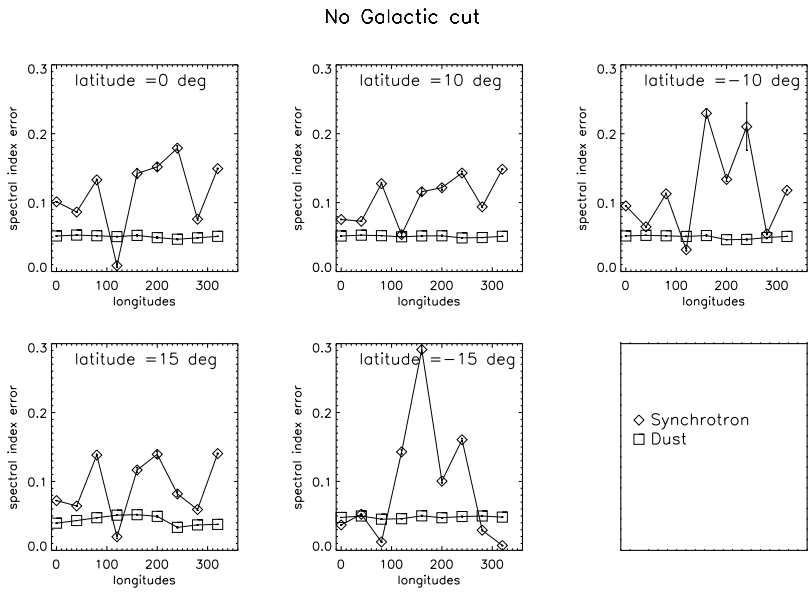

Figure 4.1: Absolute errors in the spectral index reconstruction for the LF channels without cuts

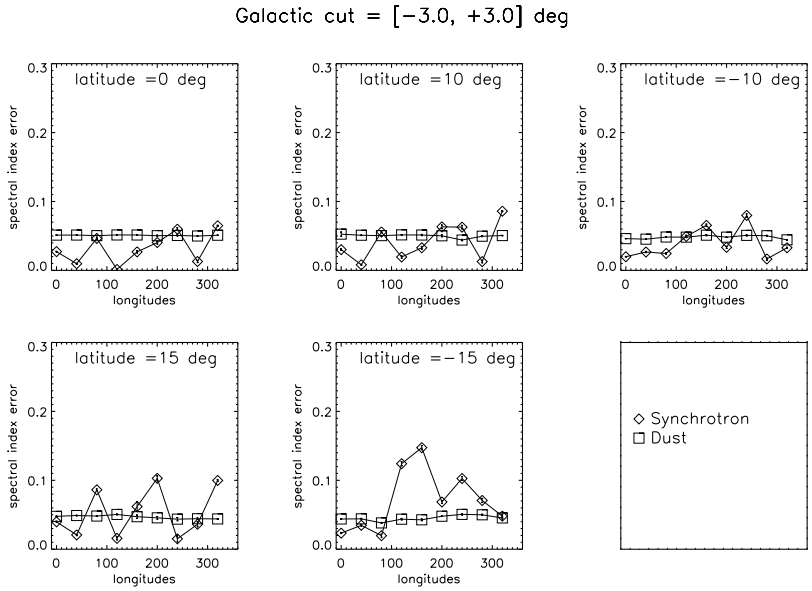

Figure 4.2: Absolute errors in the spectral index reconstruction for LF channels cutting out the Galactic plane region $|b| \leq 3°$

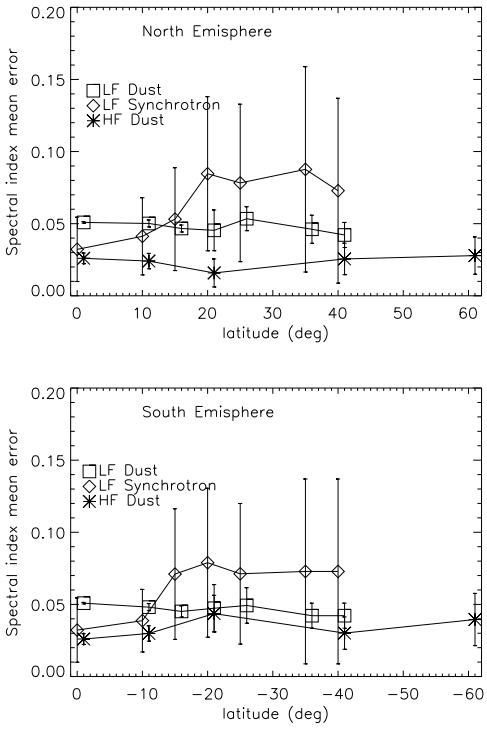

Figure 4.3: Mean absolute spectral index errors versus Galactic latitude for the analysis of LF and HF channels with the Galactic cut of $\pm 3^{\circ}$

Figure 4.1 refers to the analysis of the LF set and shows the mean values of $\Delta\beta_s$ and $\Delta\beta_d$, over 100 simulations of the sky, as a function of longitude for latitudes $b = \{0°, \pm 10°, \pm 15°\}$. The error bars, generally very small and barely visible in the figure, are the standard deviations of $\Delta\beta_s$ and $\Delta\beta_d$ from the mean. Their small values imply that the errors in the spectral index recovery are mainly systematic; for both spectral indices, part of the systematic error comes from the fact that the models we assume for the analysis differ from those defining the sky model. We clearly have problems with the estimation of the synchrotron spectral index, while the errors on β_d are generally small.

We have checked that this effect is due to confusion between synchrotron and free-free. The free-free emission is highly concentrated on the Galactic plane but depresses the mean spectral index of the combined emission over entire patches, thus biasing the estimate of the synchrotron spectral index. A better recovery of the latter would be possible with high spatial resolution maps, so that we have a sufficient number of pixels within a much smaller range of Galactic latitudes.

With the angular resolution adopted here, this effect can be minimized by cutting out a strip of a few degrees around the Galactic plane. The situation is substantially better even with a cut of $\pm 1°$ around the Galactic equator, and improves further if we enlarge the cut to $\pm 3°$ (Fig. 4.2). All the tests described below are performed by applying this cut, even though its effects are modest when working with the HF channels.

Figure 4.3 summarizes the results obtained over all the analyzed region of the sky with both the LF and HF sets. We computed the mean errors on synchrotron and dust indices over 100 Monte Carlo iterations for each patch, and the mean and standard deviation of errors obtained for patches at the same latitude. The bars are the standard deviations around the mean over longitudes.

For the LF set, while the dust index is always reconstructed with an error of $\simeq 0.05$, the error on the synchrotron spectral index increases with latitude. This is due to the fact that the substantial spatial variability of the synchrotron spectral index, implied by the Giardino et al. (2002) model, is increasingly difficult to recover as the synchrotron signal weakens with increasing Galactic latitude.

Thanks to the higher angular resolution of the HF set and to the lack of other relevant diffuse components besides CMB and dust in this frequency range, CCA allows us to reconstruct the dust spectral index with an error ~ 0.03 over the full latitude range analyzed.

4.4.3 Estimation of errors in the CMB power spectrum

As already mentioned, the CCA procedure can be viewed as the first step in component separation. In a further step, the mixing matrix estimated by this approach can be input to non-blind separation techniques. The performances of non-blind techniques are normally evaluated as functions of the system noise, assuming perfectly known mixing matrices. In this section, we estimate the uncertainties on the CMB power spectrum induced by the errors in the mixing matrix resulting from our simulations. Since at the moment the optimal component separation method exploiting the information recovered by CCA has

still to be developed, we try to estimate the errors in the CMB spectrum under conservative hypotheses. Clearly, the errors will depend on the approach adopted to separate the individual components. We investigated the general case where component separation is performed by a generic linear filter and, in particular, by a Wiener filter, and a pseudo-inverse reconstruction. The data model we assume provides a space-invariant mixing matrix $\mathbf{H}$, obtained with spectral indices $\overline{\beta}_s$ and $\overline{\beta}_d$ as defined in § 4.4.2. To evaluate the errors caused by an approximated estimate of the mixing matrix, we assumed the estimated matrix, $\hat{\mathbf{H}}$, to be generated by a distribution of the spectral indices such as the one described in the above sections. Following a theoretical derivation, the errors are evaluated in terms of quantities that are known for our simulation, thus allowing the estimation to be made without actually separating the components.

For simplicity, we are going to derive the equations in spherical harmonics. In the harmonic space, the problem stated in eq. (4.1) simply becomes:

$$\mathbf{x}_{\ell m} = \mathbf{H}\mathbf{s}_{\ell m} + \mathbf{n}_{\ell m}, \tag{4.14}$$

where the vectors $\mathbf{x}_{\ell m}$, $\mathbf{s}_{\ell m}$, and $\mathbf{n}_{\ell m}$ contain the harmonic coefficients of channels, sources and instrumental noise, respectively. As explained in Chapter 3, using a linear approach to component separation, an estimate $\hat{\mathbf{s}}_{\ell m}$ of the vector $\mathbf{s}_{\ell m}$ can be obtained as:

$$\hat{\mathbf{s}}_{\ell m} = \mathbf{W}_{\hat{H}}^{(\ell)} \mathbf{x}_{\ell m}, \tag{4.15}$$

where the reconstruction matrix $\mathbf{W}_{\hat{H}}^{(\ell)}$ depends on the estimate $\hat{\mathbf{H}}$ of the mixing matrix, which is a function of the estimated spectral indices. Following Tegmark & Efstathiou (1996) and Bouchet & Gispert (1999), the estimation error on the source spectra, in matrix notation, can be expressed as:

$$\Delta\mathbf{C}_{\hat{H}}^{(\ell)} = \frac{1}{2\ell+1} \sum_{m=-\ell}^{\ell} \langle (\hat{\mathbf{s}}_{\ell m} - \mathbf{s}_{\ell m}) (\hat{\mathbf{s}}_{\ell m} - \mathbf{s}_{\ell m})^{\dagger} \rangle, \tag{4.16}$$

where $\langle ... \rangle$ indicates expectation and $\dagger$ indicates conjugate transposition. By using eqs. (4.14) and (4.15), after a straightforward calculation, we have:

$$\begin{aligned} \Delta\mathbf{C}_{\hat{H}}^{(\ell)} &= (\mathbf{W}_{\hat{H}}^{(\ell)}\mathbf{H} - \mathbf{I})\mathbf{C_s}^{(\ell)}(\mathbf{W}_{\hat{H}}^{(\ell)}\mathbf{H} - \mathbf{I})^{\dagger} + \\ &+ \mathbf{W}_{\hat{H}}^{(\ell)}\mathbf{C_n}^{(\ell)}(\mathbf{W}_{\hat{H}}^{(\ell)})^{\dagger}, \end{aligned} \tag{4.17}$$

where $\mathbf{I}$ is the identity matrix, and $\mathbf{C_s}$ and $\mathbf{C_n}$ are, respectively, the source and the noise power spectra.

Eq. (4.17) can be simplified by assuming that the source and the noise processes are mutually uncorrelated: in this case $\mathbf{C_s}$, $\mathbf{C_n}$ and $\Delta\mathbf{C}_{\hat{H}}^{(\ell)}$ are diagonal matrices. If we define:

$$C_s^{(\ell)}(i) \equiv \mathbf{C_s}^{(\ell)}(i,i)\ , \tag{4.18}$$

$$C_n^{(\ell)}(i) \equiv \mathbf{C_n}^{(\ell)}(i,i), \tag{4.19}$$

the estimation error on the i-th source is:

$$\Delta C_{\hat{H}}^{(\ell)}(i) \equiv \Delta \mathbf{C}_{\hat{H}}^{(\ell)}(i,i) = \sum_{j=1}^{N} |(\mathbf{W}_{\hat{H}}^{(\ell)}\mathbf{H} - \mathbf{I})_{ij}|^2 C_s^{(\ell)}(j) + \\ + \sum_{j=1}^{M} |W_{\hat{H}}^{(\ell)}(i,j)|^2 C_n^{(\ell)}(j), \tag{4.20}$$

where N is the number of sources and M the number of channels. The error $\Delta C_{\hat{H}}^{(\ell)}(i)$ refers to the frequency at which the mixing matrix has all its elements equal to 1. Eq. (4.20) highlights how the different terms affect the estimation error: the first term accounts for the contamination due to the other sources, while the second one accounts for the effect of the instrumental noise. Note that in the first term of eq. (4.20) there is the product of the reconstruction matrix $\mathbf{W}_{\hat{H}}^{(\ell)}$, depending on the estimated mixing matrix $\hat{\mathbf{H}}$, with the true mixing matrix $\mathbf{H}$. As we will see, this term is minimum when $\hat{\mathbf{H}} = \mathbf{H}$ and increases as the estimated mixing matrix differs from the true one. From eq. (4.20), we can approximately evaluate the error on the spectrum of any component, provided that the source and noise spectra are known, without explicitly reconstructing that component. In particular, we considered two exemplicative cases for the reconstruction matrix $\mathbf{W}_{\hat{H}}^{(\ell)}$, the Wiener filter solution and the pseudo-inverse solution, described by eqs. (3.34) and (3.30) respectively.

To evaluate the uncertainties on the estimated CMB spectrum when the mixing matrix is not known exactly, we used a Monte Carlo approach: we generated 100 mixing matrices $\hat{\mathbf{H}}$ drawn from the probability distribution for the spectral indices described below. For each matrix we computed the $\Delta C_{\hat{H}}^{(\ell)}(cmb)$ from eq. (4.20). For the LF set, these errors have been evaluated at the reference frequency of 100 GHz using four sources (CMB, synchrotron, dust and free-free) and five channels (30, 44, 70, 100, 143 GHz). For the HF set we used two sources (CMB and dust) and three channels (217, 353, 545 GHz), with the reference frequency at 217 GHz. For each channel set, we used the all-sky power spectra of the reference source templates as the input spectra $C_s^{(\ell)}(i)$. The $C_n^{(\ell)}(i)$ for each channel have been calculated as:

$$C_n^{(\ell)}(i) = 4\pi\sigma_i^2/N_i, \tag{4.21}$$

where N_i is the number of pixels, and the RMS pixel noise values σ_i have been taken from Table 4.1.

As we have been working with sky patches, we should perform Monte Carlo simulations patch by patch, using the appropriate basis, and then combine the information over the whole sky. However, since we only want to get an indicative amplitude for $\Delta C_{\hat{H}}^{(\ell)}(cmb)$, we only performed our trials on a single set of all-sky simulations, decomposed into spherical harmonics. On the other hand, since an adequate strategy to combine the results obtained on patches to achieve a coordinated all-sky component separation has yet to be developed, we will confine ourselves to the multipole range constrained by the patch size.

For each iteration of our Monte Carlo simulations, we generated the mixing matrix from synchrotron and dust spectral indices that are Gaussian-distributed around their true values $\overline{\beta}_s$ and $\overline{\beta}_d$. In particular, we used standard deviations of 0.1 and 0.05, respectively, for the distributions of synchrotron and dust indices in the LF channels, and a standard deviation of 0.03 for the dust index in the HF channels. These values are upper limits to the ones shown in Fig. 4.3. We then exploited eq. (4.20) to compute the error on the CMB power spectrum for both the Wiener filter and the pseudo-inverse filter. From our Monte Carlo simulations, we computed the average value of $\Delta C_{\hat{H}}^{(\ell)}(cmb)$, which is the total error on the CMB power spectrum estimation. We also estimated the standard deviation $\sigma_{\Delta C}$ of the random variable:

$$\Delta C_{\hat{H}}^{(\ell)}(cmb) - \Delta C_{H}^{(\ell)}(cmb), \tag{4.22}$$

where $\Delta C_{H}^{(\ell)}(cmb)$ is obtained for $\hat{\mathbf{H}} = \mathbf{H}$, and assumed it as the error on the CMB spectrum due to the estimation of the mixing matrix.

The results are shown in Fig. 4.4. In the upper panel we show the errors for both the Wiener filter and the pseudo-inverse filter from the LF channel data, as functions of the multipole ℓ, together with the original CMB power spectrum. The lower panel displays the corresponding results for the HF channels. All the errors are computed without correction for the noise contribution; cosmic variance is not included. Note that the Wiener filters are more accurate, but the differences with the pseudo-inverse solutions decrease once corrections for noise are applied. This is particularly true for the HF set, where the noise level is higher. The total error on the CMB power spectrum $\Delta C_{\hat{H}}^{(\ell)}(cmb)$ turns out to be of the order of 1% for both the channels sets, and decreases from lower to higher multipoles. In both cases the contribution of the errors in the estimation of the mixing matrix is subdominant.

In conclusion, the tests described above demonstrate that CCA applied to simulated data with Planck specifications is a promising tool to estimate the mixing matrix parameterizing the frequency scaling of different astrophysical signals in CMB observations. We find that the most accurate results are obtained in the latitude range $[-30°, +30°]$, where the foregrounds we aim to recover are relatively strong. However, the cut of a narrow strip (a few degrees wide) around the Galactic equator improves the recovery of the synchrotron spectral index, which is biased by the strong concentration of free-free emission in the Galactic plane. We have shown that, exploiting non-optimized component separation techniques, such as Wiener filter and pseudo-inverse filter, the errors in the mixing matrix determination allow us to estimate the CMB power spectrum with an uncertainty of the order of 1% on the angular scales constrained by our patch size.

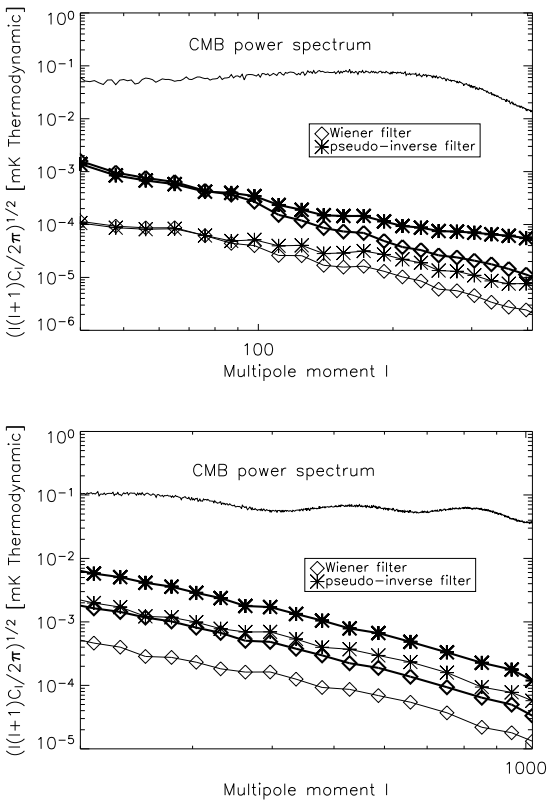

Figure 4.4: Estimated errors on the CMB power spectrum for Wiener filter and pseudo-inverse filter. For each filter, the thicker (upper) line shows the total error, the lighter (lower) one is the contribution due to errors in the mixing matrix estimation. Upper panel: LF data set, reference frequency 100 GHz. Lower panel: HF data set, reference frequency 217 GHz.

4.5 Blind comparison of component separation methods

The test described in the following were proposed and coordinated by the PLANCK component separation working group. The purpose was to evaluate the performances of the various component separation methods developed for PLANCK on a uniform data set, in order to make the results directly comparable. Another important feature of this test is that it was performed blindly by the partecipating teams, i.e. without the possibility to check the results with true inputs after the first release of the products. Then, true inputs were circulated and all teams had the possibility to check their procedure and, eventually, upgrade some products. The idea was to face a problem as close as possible to the real situation with actual PLANCK data. For the same reason, the simulation has been designed to reach the highest possible level of sophistication in terms of input components.

In particular, the simulation contains, besides the CMB, Galactic synchrotron, dust and free-free, as well as the thermal SZ effect and IR and radio point sources. The adopted sky model is similar to the PSM described in § 4.3.1, but changes were introduced both in the templates and in the frequency scaling in order to preserve the blind characteristic of the test. Both synchrotron and thermal dust had a spatially varying spectral dependence.

The simulation of the instrumental response comprises spatially varying noise with realistic hit-count maps, Gaussian beams and Dirac delta frequency response functions. The data set consisted in one simulated PLANCK temperature map per frequency channel plus ancillary data including a template for each diffuse component, catalogs of known radio and IR sources with extrapolated fluxes, and a catalog of known galaxy clusters. It is worth to note that this data set was not what used to generate the simulations. The ancillary data just reflected what our knowledge of foregrounds may be from other sources of information at the time we analyse PLANCK data. Small scale data were missing, point source spectra were not exactly those used to generate the simulations, and the catalogs were incomplete, especially with regard to faint sources.

The test consisted in analysing a single realization of the data, and providing, after a period of four months, the results of each method, within a list of deliverables. In particular, this list comprises, together with other products, the following:

- CMB map and its estimated error;
- Binned CMB temperature power spectrum, with a given binning scheme, and estimated errors, decomposed into contribution from noise and measurement errors, and cosmic variance;
- Maps of all the components identified in the data, at all the frequencies needed for a complete description.
- Catalogs of detected IR and radio point sources;
- A catalog of clusters of galaxies seen in SZ.

4.5.1 Analysis

The analysis we performed consists basically of two steps: the estimation of the mixing matrix with CCA and the source reconstruction with harmonic Wiener filtering. As already mentioned, CCA is applied on sky patches, while the harmonic WF essentially performs a full-sky analysis. Thus, the idea is to estimate the spectral dependences of the components on a sky patch and then exploit this information to perform a full-sky source reconstruction. This strategy presents some problems, which however we tried to solve as explained in the following. The first issue is that to obtain a good result with the WF the mixing matrix should be representative of the full-sky frequency scaling of the components. We then choose to work with a big patch (around 2000 square degrees) at low Galactic latitude. In fact, regions across the Galactic plane contain most of the foreground contribution and hence are better suited to estimate their spectral behavior. Then, to avoid problems related to the particular choice of the patch, we performed the analysis for nine of such patches. For each patch we estimated the mixing matrix and we got the reconstructed components through WF. This allowed us to get nine versions of the same product, and to get the final result and its error as mean and standard deviation of the nine trials. In the following we describe in details the two steps performed for each sky patch.

Mixing matrix estimation

For the estimation of the mixing matrix we worked with all the PLANCK channels plus the ancillary synchrotron template (the Haslam 408 MHz map). As in the previous test, the latter were considered as a pure synchrotron map as we previously described. The resolution of all channels has to be degraded to 33', so we worked with the Healpix parameter NSIDE=512. We adopted a Galactic cut of $\pm 3^\circ$ as suggested by the results of the previous test (Bonaldi et al. 2006). This cut is also useful to exclude a region of strong concentration of point sources, whose presence could bias the mixing matrix determination. We estimated that the remaining sources present in the patch could not significantly modify its total flux at the various frequencies, and thus they were not masked. As we did previously, the noise was assumed to be Gaussian and uncorrelated between pixels. To derive the noise covariance term $C_n(0,0)$ for each channel we computed the standard deviation within the pixels of the considered patch of a set of simulated noise maps. For this simulation we exploited the provided hit count maps to generate a noise map and then performed the 33' smoothing.

We assumed a mixing matrix of four sources (CMB, synchrotron, dust and free-free) and three free parameters (synchrotron spectral index, dust spectral index, dust temperature). The estimated parameters were used to compute the mixing matrix for WF. In particular, the latter is not identical to the one estimated with CCA. Besides the fact that for the WF we used a different channel set (see below), the WF matrix has an additional component, which also depends on the parameters estimated by CCA. This component accounts for the second-order in the dust temperature field as suggested by Stolyarov et al. (2005) (see § 3.5.4). This is done in order to account for the spatial variations

of the frequency dependence of thermal dust from the considered patch to the rest of the sky. As argued by Stolyarov et al. (2005), the variations in the synchrotron spectral index induce minor errors in the CMB reconstruction for the PLANCK mission and thus have not been considered.

Source reconstruction

For the source reconstruction we used a subset of the channels exploited above in order to minimize foreground contamination. In particular, we used all the PLANCK channels with no ancillary template to recover the foreground maps, and only channels from 44 to 353 GHz to reconstruct the CMB. Since we now work in the harmonic domain, each input channel is exploited at its original resolution. Nevertheless, some preprocessing on maps was required in order to obtain satisfactory separations. In particular, we had the need to mask some highly contaminated regions of the sky, namely, CenA, ρ Oph, the Large Magellanic Cloud, and the Orion/Eridanus complex. These regions appeared as very noisy spots in the reconstructed maps, showing that the presence of such strong emissions with peculiar frequency scaling was an issue for the component separation method. We checked that, once these regions were excluded from the analysis, the separation is considerably improved over all the sky.

As explained in Chapter 3, the standard procedure of masking is in principle not allowed when working in the harmonic domain. As suggested by Stolyarov et al. (2005), a suitable way is to work with full-sky maps where the regions to be masked have been given zero weight when computing the harmonic coefficients. In practice, this can be done by modifying the input maps replacing the regions to be masked with a fake signal. In our case we used the mean full-sky signal plus a noise realization. In this way the transition from the "masked" to the unmasked region is smooth and strong sources hampering the reconstruction are removed.

As mentioned in § 5.3, the WF solution requires to know, besides the mixing matrix, estimated as described above, the power spectra of noise and of sources. The noise power spectra were computed through a MC simulation exploiting the known hit count maps and nominal RMS levels for each channel. For the power spectra of sources, we relied on the iterative process described in § 3.5.4. To derive the initial power spectra we first performed a low-resolution reconstruction with the Generalized Least Square solution [eq.(3.32)], which only requires the prior knowledge of the noise power spectra. We then used as our starting guess the power spectra of these reconstructed sources extrapolated to small scales assuming ℓ^{-3} scaling behavior (Zavarise, degree thesis).

Preparation of final products

The maps recovered as we previously described are still affected by the presence of point sources. We then computed a mask for those sources exploiting the provided ancillary catalogs and the predicted fluxes. We considered the channels from 44 to 353 GHz and we excluded all sources having predicted flux higher than a certain limit, as specified in Table 4.2. The mask we obtained excludes

Table 4.2: Flux limits adopted for computing the point source mask

Frequency (GHz)	44	70	100	143	217	353
Flux limit (mJy [1])	300	300	100	100	100	150

around 10% of the sky. The component maps were averaged over the nine trials and their error maps were estimated as the standard deviation map of the same set. These maps were finally masked with the mask computed as we previously specified. To obtain the CMB power spectrum and its error, we computed the power spectra of each of the nine CMB maps outside the above mask and computed their unbiased estimators. In particular we had to correct for the bias of the Wiener filtering (see § 5.3) and for the mode-mode coupling kernel due to the mask. The latter was accounted for following the MASTER approach (Hivon et al. 2002). We finally computed the mean of the nine spectra (which we provided as final CMB spectrum) and the standard deviation (which we provided as its error excluding cosmic variance).

4.5.2 Results and conclusion

In Figure 4.5 we show two plots regarding the quality of the reconstruction of the CMB map. In the upper panel the power spectrum of the residuals between the true and the estimated CMB are shown for each method and compared to the input CMB spectrum. In particular, those spectra are computed at low Galactic latitude, where the foreground contamination is stronger. As we can see, the quality of the reconstruction obtained with CCA is very good and competitive with that of the other methods. Despite the complexity of this simulation, we managed to get an error of the order of 1% on a wide range of multipoles, as already found in the previous test. However, while our previous results indicated that the error decreases with increasing multipole, now we find an opposite behaviour. This is simply due to the fact that in the previous case we only considered diffuse foregrounds, whose spectra vanish at high multipoles, while in this case we also have point sources, whose spectra D_ℓ increase as $\ell(\ell+1)$.

In the lower panel of Figure 4.5 we show the residual map of CCA smoothed to a resolution of 20 arcmins. The residual on the Plane, where Galactic foregrounds are stronger, is very low. Thus, the contamination due to diffuse components, which is the objective of CCA, proved to be significantly reduced. We have instead noisy spots uniformly distributed in the map, mainly due to SZ clusters and point sources. As mentioned above, this was the first test of our method in presence of such sources, so it is very likely that they were not treated in the best possible way. A better solution would be probably to apply our algorithm after a separation of the strongest sources has been performed, for example with one of the methods described in § 3.2 and § 3.3. This was not feasible in our case, as the short deadline did not allow us to perform our analysis after that of point source extraction.

As we mentioned, we estimated the error in the CMB map as the standard deviation of the maps we reconstructed starting from mixing matrices estimated in different patches of the sky. The results of the test demonstrated that this

procedure leads to an underestimation of the true error, unless the patches are selected in distant regions of the sky. In fact, selecting all patches in the Galactic plane the mixing matrices are all similar to each other, and do not represent the true spatial variability of the foreground spectra.

The result obtained on the CMB power spectrum with CCA is shown in Fig. 4.6. The power spectrum estimation is correct until $\ell \sim 2000$, which is almost the limit set by the 5 arcmins beam of PLANCK. The error bars, comprehensive of both reconstruction errors and cosmic variance, are a good estimation of the true errors.

Regarding foreground components, we only delivered a dust map for each PLANCK channel, obtained by adding the maps reconstructed to first and second order, scaled with the corresponding spectral behavior. The reconstruction of synchrotron and free-free maps were in fact not satisfactory, as reported below. In figure 4.7 we show the relative errors in the reconstruction of the dust component at 143 GHz. We can see that such error is minimum across the Galactic plane, where we performed the mixing matrix estimation, and is maximum near the poles, where the component has very low signal to noise ratio. The quality of the estimated dust maps is competitive with that of the maps delivered by the other groups.

Concerning synchrotron and free-free, we did not manage to properly disentangle these components from each other. This was largely due to our inability to properly deal with strong radio sources like HII regions and SN remnants across the Galactic plane. We checked that applying a Galactic cut of $\pm 7^\circ$ the results were greatly improved; however such a cut is a relevant limitation to the reconstruction of Galactic components. This aspect then requires more study, as well as the separation of the SZ component, which we did not address in this test. In conclusion, this blind comparative test allowed us to apply for the first time the CCA method combined with an harmonic WF, obtaining very good results, especially in terms of the CMB component. Despite the presence of additional complications, like point sources, SZ effect, and non-stationary noise, we obtained for this component results comparable with those expected on the basis of the simpler test described in § 4.4. The reconstruction of foreground components is still sub-optimal; however substantial improvements are likely to be achieved once the issue of point sources has been more properly addressed.

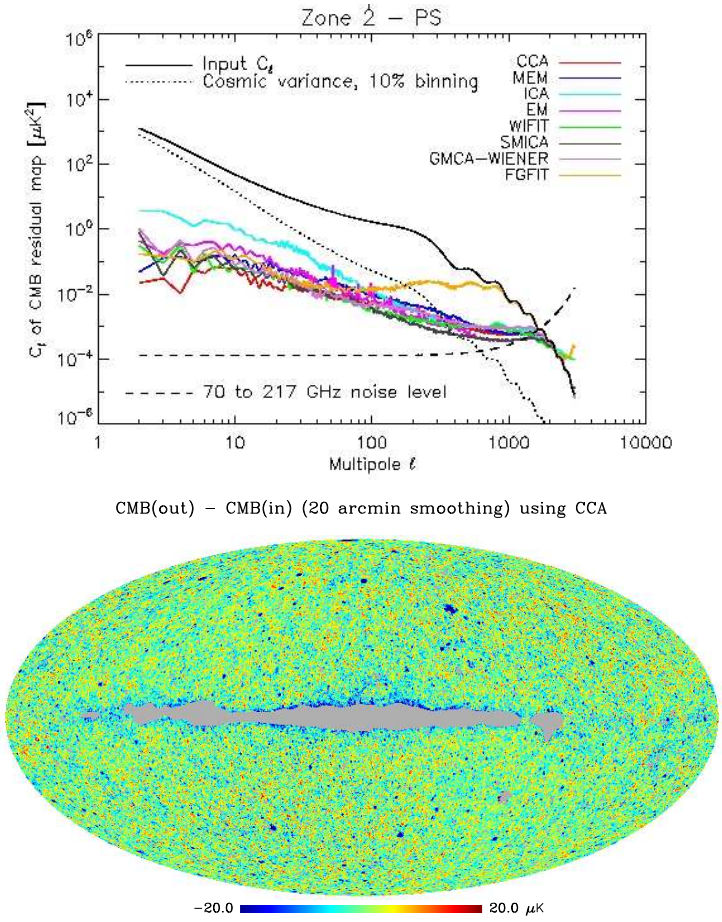

Figure 4.5: Upper panel: power spectra of residual between true and estimated CMB map at low Galactic latitude for each component separation method, compared to the true CMB model. Lower panel: residual map for CCA smoothed to a resolution of 20 arcmins.

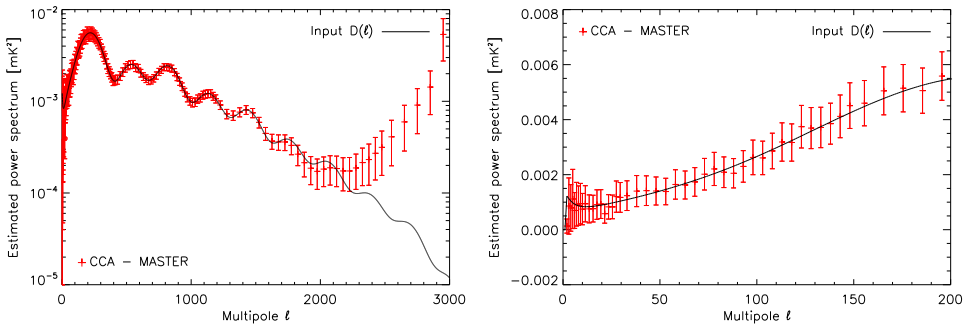

Figure 4.6: CMB power spectrum estimated with CCA compared to the model. In the right panel we zoom on of the lowest multipoles, which are not clearly visible in the left one due to the logarithmic scale.

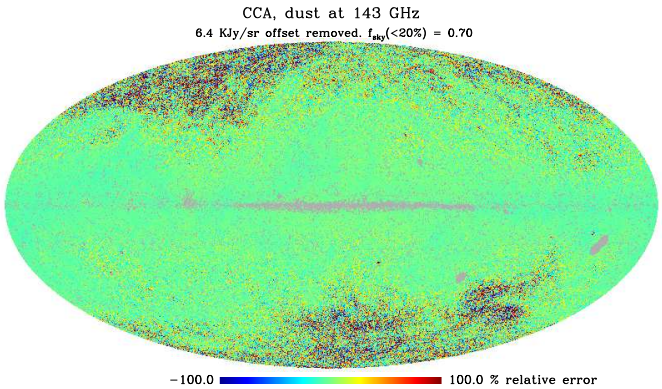

Figure 4.7: Relative error on reconstructed dust map at 143 GHz.

Chapter 5

WMAP 3yr data with CCA

5.1 Introduction

In this Chapter we report on an application of CCA to the three-year data of the WMAP mission. This is an important test of the method, as it allows us to check its performances against instrumental systematics. These effects cannot be easily included in a simulated data set but can affect the quality of component separation and in general of all data reduction processes. However, the major difficulty in working with real data is probably the fact that we have to deal with our imperfect knowledge of the components. When we constructed our model of the microwave sky (see § 4.3.1), the lack of information on the astrophysical emissions at the frequencies of interest forced us to make a lot of assumptions, most of which may not reflect the reality. These preconceptions are also applied to component separation, so that working with simulated data has some degree of circularity. Conversely, when dealing with real data we have to keep our mind open to the possibility that our foreground model is flawed.

The WMAP data provide a good example of how limited our knowledge of the foreground components actually is. Bennett et al. (2003) fitted the first year data with the usual components: CMB, thermal dust, free-free and synchrotron emission. Finkbeiner (2004), De Oliveira-Costa et al. (2004) and Davies et al. (2005) however reported evidences for the presence in the data of an additional, dust-correlated microwave emission, dubbed "anomalous emission" and interpreted as due to small, fast spinning dust grains. A low frequency, dust correlated emission was identified by analyzing the three-year data (Hinshaw et al. 2006). This component may also be interpreted as flat-spectrum synchrotron emission which locally correlates with dusty active star-forming regions.

In conclusion, the topic of the diffuse components in the WMAP data remains unsettled. Nevertheless, these data are playing a dominant role in determining the reference cosmological model. It is therefore important to have an in depth understanding of all the uncertainties stemming from our poor knowledge of Galactic foregrounds and of their effects on estimates of the angular power spectrum of the CMB, from which the values of the fundamental cosmological parameters are derived.

Our analysis is aimed at investigating these aspects. As CCA requires to

Table 5.1: Properties of the WMAP channels relevant for noise simulations.

Channel	K	Ka	Q	V	W
Frequency (GHz)	23	33	41	61	94
Resolution (degrees)	0.93	0.68	0.53	0.35	<0.23
σ_0(mK)	1.42	1.45	2.21	3.11	6.50
Mean pixel RMS (mK)	0.07	0.07	0.07	0.09	0.1

parametrise the mixing matrix, we need to specify a priori which foreground components are contributing to the maps. A preliminary analysis including only the standard components has picked somewhat odd properties of the "synchrotron" component, hinting at the presence of an additional emission with a flattish spectrum in the WMAP frequency range. We have tested various spectral shapes for such a component, the "anomalous emission" as described in the next section.

The mixing matrix estimated with CCA for each of the above models is then exploited to reconstruct maps of astrophysical components using an inversion algorithm that, in our case, is the harmonic Wiener Filter. In § 5.4 we perform several quality tests on the separated components in order to select the best models. This allows us to infer some constraints on the anomalous emission, and to present a first, albeit preliminary, template of it.

Finally, in § 5.6 we analyze the uncertainties on the derived CMB power spectrum ensuing from those on foreground properties, especially in relation to the reported deviations from predictions of the "concordance" cosmological model (Spergel et al. 2006).

5.2 Mixing matrix estimation with CCA

5.2.1 Input data

The basic data are the three-year WMAP maps in the K, Ka, Q, V and W bands, whose main characteristics are summarized in Table 5.1. As already mentioned, when working with CCA we must adopt for all channels a common resolution, which we set to 1°. In fact, following Bennett et al. (2003), even if the nominal resolution is 0.93 degrees in the worst case, such a smoothing is useful suggestable in order to avoid the complications due to beam asymmetries.

The values of σ_0 reported for every channel allow us to calculate a noise map at each frequency as $\sigma = \sigma_0 N_{\rm obs}^{-1/2}$, where $N_{\rm obs}$ is the map of the effective number of observations, provided with the data. The maps were then smoothed to the common resolution of 1° (Bennett et al. 2003). Since we do not have an exact formula to associate an RMS noise level to each map after smoothing, we simulated a set of ten WMAP noise maps at each WMAP frequency using the corresponding σ_0 and $N_{\rm obs}$. We then smoothed them to the 1° resolution, and computed the mean RMS for each channel.

If correlations in the instrumental noise among different channels induced by smoothing can be neglected, $\mathbf{C}_n(\tau, \psi)$ is a diagonal matrix whose elements

are the empirical variances for $(\tau, \psi) = (0, 0)$. The simulations carried out by Bonaldi et al. (2006) showed that such approximation does not significantly affect the quality of the mixing matrix estimation.

Strong point sources can contribute substantially to the mean surface brightness in some pixels and since their frequency dependence is generally different from those of diffuse components, they may bias the mixing matrix estimates. Source fluxes are highly diluted in the relatively low resolution maps used here and we find that the point source effects become negligible once we mask a region of 1° radius around each source contained in the three-year point source catalogue provided with the WMAP data. In addition, based our previous analyses, we applied a Galactic cut of $\pm 3^\circ$. Finally, we masked a few highly contaminated regions, namely Cen A, the Large Magellanic Cloud, ρ Oph, Orion A, Orion B and Tau A.

To get a better leverage for foreground differentiation we complemented the WMAP data with a "thermal dust" and a "synchrotron" map. The former was obtained extrapolating to 850 GHz the dust map by Schlegel et al. (1998) using the best-fit model of Finkbeiner et al. (1999). Such model comprises two dust components at different temperatures. Since the warmer dust component is irrelevant at WMAP frequencies, the use of the extrapolated dust map rather than the original $100\,\mu$m IRAS map has the advantage of allowing us to use a single temperature dust model.

The synchrotron map is based on the Haslam et al. (1982) 408 MHz map. Even if the Haslam map is often assumed to be pure synchrotron, contributions from the free-free emission can be important, especially on the Galactic plane (Paladini et al. 2005). Our "synchrotron" map was then obtained by subtracting from the Haslam map the free-free contribution estimated from the Hα map corrected for dust absorption (Dickinson et al. 2003).

5.2.2 Analysis

As we already explained, CCA requires to parameterize the mixing matrix $\mathbf{H}$. This means that we have to exploit our knowledge of foregrounds to model the WMAP data in terms of a small number of parameters. On the other hand, as mentioned in § 1, we are not even sure about the number of foreground components that need to be taken into account.

Also, foreground spectral parameters vary across the sky. Therefore we would ideally want a map of the values of such parameters with sufficiently high resolution. However, CCA needs a large number of independent pixels in order to derive them. As discussed in the previous Chapter, a good compromise is to apply CCA to patches of about $1500\,\mathrm{deg}^2$. The spectral parameters may still vary within each patch, and CCA yields their flux-weighted average. We worked with patches of $(\Delta l, \Delta b) = (50^\circ, 30^\circ)$ on the Galactic plane, and increased Δl with increasing $|b|$ as necessary to roughly preserve the patch area. We centered our patches at longitudes $l_c = \{0^\circ, 40^\circ, 80^\circ, ...320^\circ\}$ and latitudes $b_c = \{0^\circ, \pm 15^\circ, \pm 25^\circ, \pm 35^\circ\}$. The 63 different sky patches partially overlap, but the overlap is small enough for them to be taken as independent of each other. In fact, the covariance matrices [eq. (4.5)] of adjacent patches turn out to be all

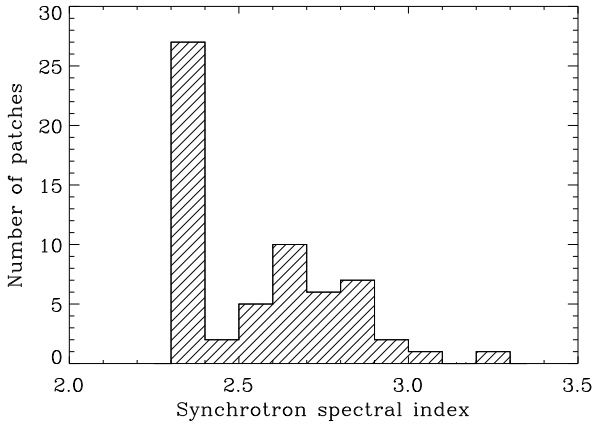

Figure 5.1: Distribution of the synchrotron spectral index β_s obtained by CCA for model **M1**.

substantially different from one another. For any given input model CCA has then yielded the mixing matrix for each patch. In general, there are no indications of strong variations across single patches. Should such strong variations happen, the resulting mixing matrices would depend on the choice of the patch shape and boundaries. However, the number of patches is sufficiently large to ensure that the inferred distributions of spectral parameters are stable.

The standard foreground model, M1

We start our analysis by adopting the most conservative model, which will be referred to as **M1**, containing the standard mixture of CMB, synchrotron, thermal dust and free-free. Since the thermal dust spectrum is only very poorly constrained by the WMAP data, the results are very weakly dependent on the assumed dust temperature and emissivity index. We then fixed these quantities to the commonly used values $T_{\rm dust} = 18\,{\rm K}$ and $\beta_d = 1.67$ in eq. (4.4), so that we are left with only one free parameter, the synchrotron spectral index β_s.

The distribution of β_s obtained with CCA and shown in Figure 5.1 has two peaks. To determine the position and width of the peaks we divided the distribution in two parts, $\beta_s \leq 2.4$ and $\beta_s > 2.4$, and fitted them with Gaussian distributions. One peak is at $\beta_s \simeq 2.7$ and has a dispersion $\sigma \simeq 0.2$, which is roughly what is expected for synchrotron. The second one, at $\beta_s = 2.3852$, is extremely narrow $\sigma \simeq 0.0004$, hinting at a different component. We explicitly checked that this distribution is unaffected by different choices of the thermal dust parameters. This immediately leads to the question: what is this second flatter component?

In Figure 5.2 we show the map of the recovered synchrotron spectral indices. The mean value is adopted in the regions where different patches overlap. The flattish component is mainly located at low Galactic latitudes, more than $\sim 40^\circ$ away from the Galactic center, and is not well correlated with the synchrotron template. In the following we investigate different possible spectral shapes for

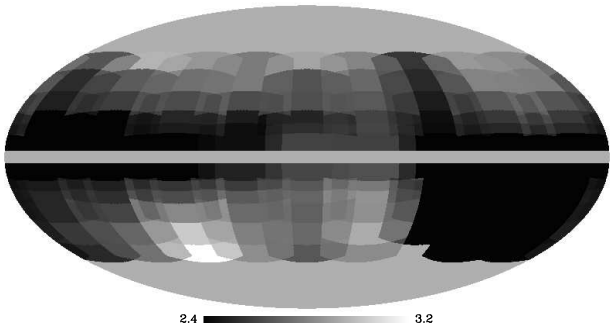

Figure 5.2: Map of the synchrotron spectral indices recovered by the CCA for model **M1**.

Table 5.2: Summary of the models investigated. S=synchrotron, AE=anomalous emission, TD+AE=thermal dust+anomalous emission.

Model	Investigated component	Parametrization	Free parameters and ranges
M1	S	Equation (4.3)	$2.0 \leq \beta_s \leq 3.5$
M2	AE	Equation (5.1); $\nu_{\rm max} = 20\,{\rm GHz}$	$1.0 \leq m_{60} \leq 5.0$
M3	AE	$T_{\rm A,X}(\nu) \propto \nu^{-\beta_2}$	$2.0 \leq \beta_2 \leq 2.6$
M4	AE	$T_{\rm A,X}(\nu) \propto [\nu^{\beta_x+1}]/[e^{h\nu/kT_x} - 1]$; $\beta_x = 2.4$	$0.2\,{\rm K} \leq T_x \leq 0.7\,{\rm K}$
M5	TD+AE	Equation (5.5); $\nu_{\rm max} = 20\,{\rm GHz}$	$1.0 \leq m_{60} \leq 5.0$, $0.1 \leq R_{60} \leq 2.0$

this "anomalous" component.

5.2.3 Models for the "anomalous" component

As pointed out by many authors (e.g. de Oliveira-Costa et al. 2004; Watson et al. 2005), the spectral behavior of the anomalous emission clearly differs from free-free and synchrotron at 10–15 GHz (where we don't have all-sky maps), but is similar to them in the 20–40 GHz range. This means that any attempt to estimate simultaneously the spectral parameters of synchrotron and of the anomalous emission from WMAP data only is liable to strong aliasing effects. We have therefore chosen to estimate the spectral parameters of the anomalous emission keeping β_s fixed, and repeating the analysis for several values in the range $2.8 \leq \beta_s \leq 3.1$. Specifically we ran CCA over all sky patches for $\beta_s = \{2.80, 2.86, 2.92, 2.98, 2.04, 3.10\}$.

As for the anomalous emission spectrum, we have investigated the models whose free parameters are summarized in Table 5.2, and are described below. The proposed frequency scalings for the anomalous emission are also shown in Figure 5.3.

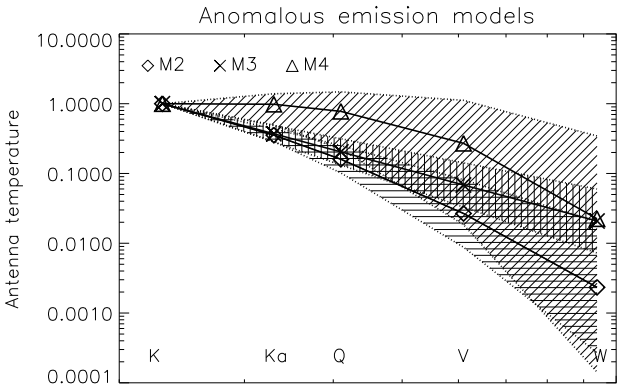

Figure 5.3: Frequency spectra of the anomalous emission for the models **M2**, **M3** and **M4**. The curves are normalized at the K band. For each model, the shaded area shows the range of values allowed for the estimation, while the symbols refer to the central values.

Model M2

The results by de Oliveira-Costa et al. (2004), Watson et al. (2005), and Davies et al. (2006) suggest that the spectrum of the anomalous emission for $\nu > 20\,\mathrm{GHz}$ may be represented by a parabola in the $(\log\nu, \log S)$ plane

$$\begin{aligned} \log T_{\mathrm{A,X}}(\nu) &= \mathrm{const} - \left(\frac{m_{60} \log \nu_{\mathrm{max}}}{\log(\nu_{\mathrm{max}}/60\,\mathrm{GHz})} + 2 \right) \log\nu \\ &+ \frac{m_{60}}{2\log(\nu_{\mathrm{max}}/60\,\mathrm{GHz})} (\log\nu)^2, \end{aligned} \tag{5.1}$$

with ν in GHz and $\nu_{\mathrm{max}} = 20\,\mathrm{GHz}$. The free parameter, m_{60}, is the angular coefficient at a frequency of 60 GHz in the $(\log\nu, \log S)$ plane.

By running CCA for the above set of values for β_s we found that the mean values of m_{60} over the sky patches are in the range $3.8 \leq m_{60} \leq 4.5$, and correlate with β_s. The linear best-fit relation, shown in Figure 5.4, is:

$$m_{60} = (2.1101 \pm 0.0005)\beta_s - (2.073 \pm 0.002). \tag{5.2}$$

The corresponding spectral shape is compatible with the anomalous emission detected by Davies et al. (2006). In particular, our scaling between the K and Ka bands is almost the same they found, and the one between Ka and Q is very similar. Our model decreases more rapidly than theirs at higher frequencies, but is still inside their error bars.

Model M3

Alternatively, the anomalous emission might be interpreted as flat-spectrum synchrotron, possibly highly self absorbed, associated with strong magnetic fields

local to star-forming regions (and thus dust-correlated). To investigate this possibility we parametrize this component as a power law, with a spectral index β_2.

As before, we obtained the distribution of β_2 over the sky patches for each value of β_s, which turned out to be quite narrow, with a dispersion $\sigma = 0.003$, and independent of β_s. The mean value of the spectral index,

$$\langle \beta_2 \rangle = 2.144, \tag{5.3}$$

turns out to be remarkably close to that of free-free, hinting at the possibility of aliasing effects. We return to this possibility in § 5.4.

Model M4

For this model we adopt the spectrum used by Tegmark et al. (2000) for the anomalous component: a grey body of the form of equation (4.4), with temperature $T_x = 0.25\,\mathrm{K}$ and emissivity index $\beta_x = 2.4$. We checked that a simultaneous estimation of both β_x and T_x was not feasible, as the algorithm failed to converge. Thus, we fixed $\beta_x = 2.4$ and allowed T_x to vary in the range $0.2\,\mathrm{K} \leq T_x \leq 0.7\,\mathrm{K}$.

As can be seen from Fig. 5.3, **M2** and **M4** give quite different frequency scalings. In fact, the latter has been proposed to fit typical Draine & Lazarian (1998) spinning dust models, but it is not suited to reproduce the results by Davies et al. (2006). Given the slope between the K and Ka bands, **M4** decreases more rapidly.

The results of Figure 5.5 can be summarized as

$$T_x = \begin{cases} 0.43 \pm 0.01\,\mathrm{K} & \text{if } \beta_s \leq 3.0 \\ 0.47 \pm 0.01\,\mathrm{K} & \text{if } \beta_s > 3.0. \end{cases} \tag{5.4}$$

The spectrum rises from the K to the Ka band, and slowly decreases towards higher frequencies. The slope between 60 and 94 GHz is consistent with what was found for **M2**.

Model M5

We tested the possibility that there is a perfect correlation between thermal dust and anomalous emission, so that they can be treated as a single component parameterized as

$$T_{\mathrm{A,dust+X}}(\nu) \propto T_{\mathrm{A,dust}}(\nu) + R_{60} \cdot T_{\mathrm{A,X}}(\nu), \tag{5.5}$$

where $T_{\mathrm{A,dust}}$ is given by equation (4.4) and $T_{\mathrm{A,X}}$ by equation (5.1). The factor R_{60} quantifies the relative intensity of the two emissions at 60 GHz. The free parameters of this model are R_{60} and m_{60}, with the other parameters fixed as in **M2**.

The recovered values of the parameters are shown in Figure 5.6. The values of m_{60} are within the range found for model **M2**, which did not assume any correlation with thermal dust, but the correlation with β_s is now weaker. The

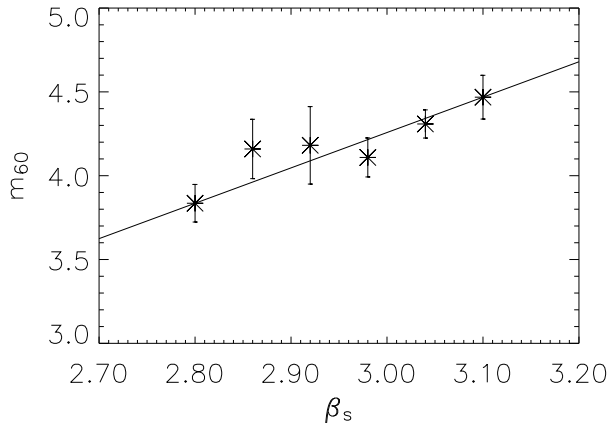

Figure 5.4: Mean estimated values of m_{60}, with their errors, plotted against the assumed values of the synchrotron spectral index β_s (model **M2**).

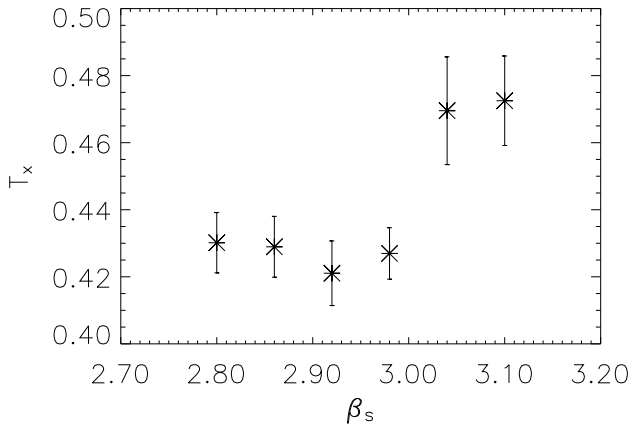

Figure 5.5: Mean estimated values of T_x, with their errors, plotted against the assumed values of the synchrotron spectral index β_s (model **M4**).

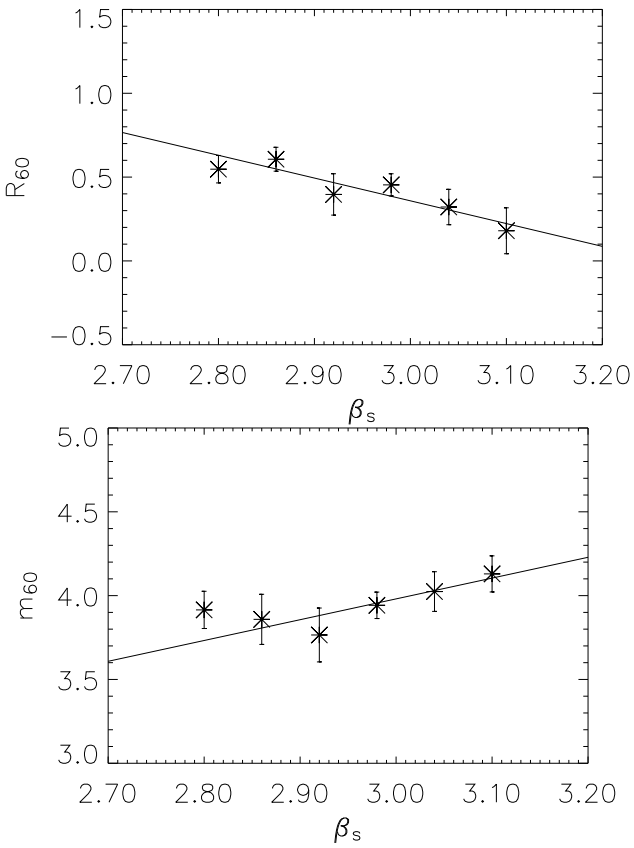

Figure 5.6: Mean estimated values of R_{60} and m_{60}, with their errors, plotted against the assumed values of the synchrotron spectral index β_s (model **M5**).

linear best-fit relations of m_{60} and R_{60} with β_s, shown as solid lines in Figure 5.6, are

$$R_{60} = (-1.4 \pm 0.4)\beta_s + (4.4 \pm 1.2) \tag{5.6}$$

$$m_{60} = (1.3 \pm 0.3)\beta_s + (0.3 \pm 0.1). \tag{5.7}$$

This is again consistent with Davies et al. (2006), both for the slope m_{60} and the ratio of the intensity of the anomalous component with respect to thermal dust, R_{60}.

5.3 Source reconstruction with the Wiener Filter

Once the mixing matrices of the diffuse components in the WMAP data were estimated for the different models, we performed the source reconstruction with harmonic Wiener Filter (WF). For the noise and the source power spectra required to perform the WF we proceeded as described in section 4.5.1. This approach uses a minimum number of priors: in practice, the components are

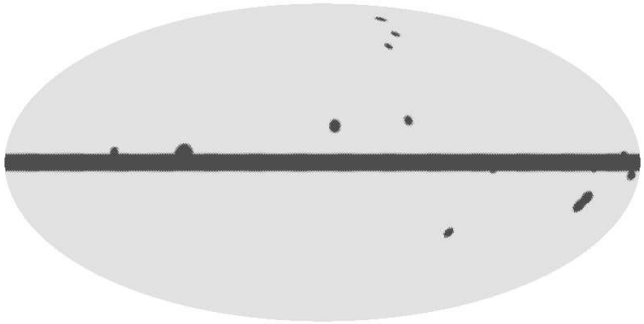

Figure 5.7: Apodized mask used to preprocess the input maps for the Wiener filter. The minimum (dark grey) and maximum (light grey) values are zero and one respectively.

identified only by their frequency scalings. The lack of prior covariance information certainly limits the quality of the reconstruction, but in this way we avoid biasing the results.

5.3.1 The Wiener filter data set

For the matrix inversion we used the WMAP K, Ka, Q, V, and W bands at their original resolutions. Since we now are working in the harmonic domain, a frequency-dependent beamwidth can be naturally accounted for. We assumed circularly symmetric Gaussian beams with the FWHM values reported in Table 5.1. Even if this may not be a good approximation of the real beams, the effect of beam asymmetries is not likely to be relevant on the relatively large angular scales we are considering here. The noise processes have been assumed to be uniform over the whole sky: to compute the noise levels, we averaged the standard deviations of a set of simulated WMAP noise maps.

Algorithms working in harmonic space require data maps defined over the whole sky. On the other hand, cutting out highly contaminated regions is generally necessary to recover the CMB map. Similarly to what done in section 4.5.1, we filled in the masked areas with a noise realization at the nominal level for the considered channel. To reduce edge effects the maps were weighted with the apodized mask shown in Figure 5.7. This mask excludes the strip at $|b| < 3°$, the LMC, the Cen A region, and regions of $1°$ radius centered on the brightest point sources. All pixels which have been modified are excluded from the analysis of the final output maps.

To take advantage of all the available information we complemented the WMAP data with the synchrotron, dust and free-free maps adopted for the mixing matrix estimation (see § 5.2). These maps have resolutions of $60'$, $5'$ and $60'$ respectively. While the inversion is performed by adopting everywhere the mean values obtained with CCA, we have allowed for the effect of variations of spectral indices of synchrotron and dust across the sky by attributing to the corresponding maps uncertainties much larger than the measurements errors. In particular, we computed the standard deviation of each prior map outside

the apodized mask of Figure 5.7 and assumed a constant RMS level of 20% for the 408 MHz synchrotron map and of 10% for the 850 GHz thermal dust map. The spread of spectral indices may induce even larger uncertainties, but we have checked that increasing the uncertainties by up to a factor of two has a negligible impact on the reconstruction of the CMB and a small effect on the foregrounds. This problem does not affect the free-free for which we have adopted the nominal RMS error of 7% (Dickinson et al. 2003).

5.3.2 Analysis

For each model, CCA gives the distribution of spectral parameters found in different sky patches. These distributions reflect, besides estimation errors, the spatial variability of the spectra. On the other hand, harmonic Wiener Filtering is applied using a single mixing matrix over the full sky, i.e. with the assumption of spatially uniform spectra. To investigate the effect of this simplification we generated a set of thirty mixing matrices for each model, drawing the spectral parameters at random from CCA distributions. For each matrix, we performed a full-sky source reconstruction up to $\ell = 300$.

In the cases of models **M2**, **M3**, **M4** and **M5**, we adopted for the synchrotron spectral index a uniform distribution in the range $2.8 \leq \beta_s \leq 3.1$. This is the hypothesis we initially made for these models, and corresponds to the values of β_s assumed by CCA. Then for models **M2** and **M5** we derived the value of m_{60} or of R_{60} and m_{60} from equation (5.2) or from equations (5.6) and (5.7) respectively. In the case of **M4** we derived T_x according to equation (5.4), while for the parameter β_2 of **M3** we used a Gaussian distribution according to equation (5.3).

The results obtained with CCA for the the standard foreground model, **M1**, indicate that generating a set of synchrotron spectral indices drawn at random from the distribution shown in Figure 5.1 would not be meaningful unless we assume two synchrotron components, but this would replicate model **M3**. For this reason we used this model for reference, adopting for the synchrotron spectral index a uniform distribution in the range $2.8 \leq \beta_s \leq 3.1$.

5.4 Reconstructed components

In Figure 5.8 we show the RMS in the WMAP bands of the components reconstructed using each model. Only pixels outside the apodized mask of Figure 5.7 have been taken into account. In this plot, the CMB component shows tiny variations from one iteration to another (the shaded regions are too narrow to be visible) and also from a model to another, suggesting that the choice of the foreground model, among those considered here, has little influence on the CMB reconstruction. This will be discussed further in § 5.6, where we will focus our analysis on the CMB component. Variations are very small also for the reconstructed thermal dust and free-free components. This is due to the fixed frequency scaling and the use of prior maps.

As expected, we have a substantial spread in the reconstructed synchrotron component, reflecting the wide range of synchrotron spectral indices used for the

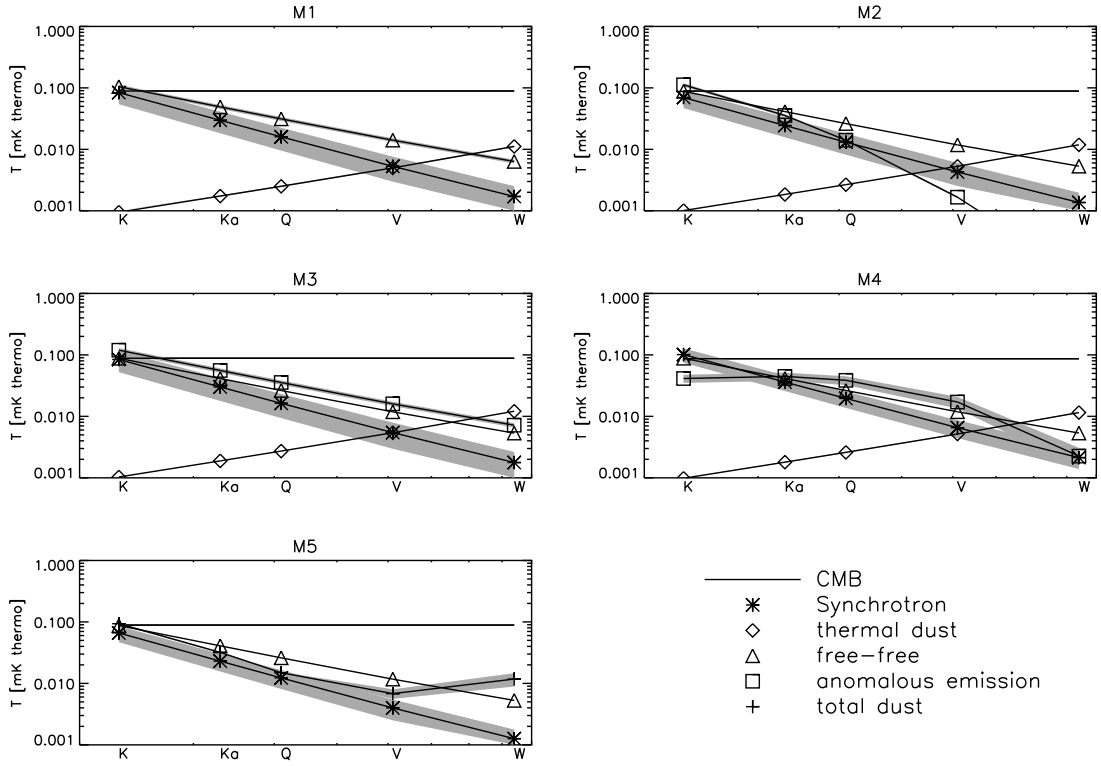

Figure 5.8: Frequency dependence of the RMS fluctuations of the components reconstructed with each model. The shaded areas, shown only for components whose spectral parameters are allowed to vary, represent the dispersion obtained from the 30 reconstructions per model, and the lines show the mean spectra.

separation. This component is found to be generally sub-dominant compared to the free-free, except possibly in the K band, in agreement with the results by Hinshaw et al. (2006).

The results for the anomalous emission components are also quite stable. If we force this component to have a power-law spectrum (model **M3**) we find that it dominates over both synchrotron and free-free in all the WMAP channels. In the case of model **M4**, the anomalous emission is found to dominate in the Ka, Q and V bands. Models **M2** and **M5** are consistent with each other, as the summed intensity of thermal dust and anomalous emission of model **M2** is close to that of the "total dust" emission of model **M5**. Moreover, they yield similar intensities for the remaining components. As previously stressed, models **M2** and **M5** yield results on the anomalous emission which are consistent with Davies et al. (2006).

5.4.1 Quality tests

Before proceeding with the analysis of the results we try to evaluate the quality of the decomposition for each model. A standard method is to analyze the residual between the data and the reconstructed sources combined by means of the estimated mixing matrix

$$\mathbf{r} \equiv \mathbf{x} - \hat{\mathbf{H}}\hat{\mathbf{s}}. \tag{5.8}$$

The analysis of the residuals allows us to check if, given a certain mixing matrix, our algorithm has succeeded in finding a plausible decomposition of the data. In the case of a perfect reconstruction of the channels, $\mathbf{r}$ contains maps of pure noise, characterized by Gaussian statistics. Foreground residuals bring in non-Gaussianities. A visual inspection of the residuals show that some non-Gaussian features are present in the maps. In particular, we can discern traces of anisotropic noise, point sources and diffuse emissions, particularly at low Galactic latitudes. The first two features are related to effects that are not accounted for in our analysis. The last one is more interesting, because it reflects our modeling and estimation errors.

Each model shows the worst contamination in the K band, even if the models including the anomalous emission are generally cleaner: see for example the comparison between **M1** and **M2** in Figure 5.9. The "residual excess" at low latitudes decreases at higher frequencies. The models **M1** and **M4** are generally worse; however this strongly depends on the synchrotron spectral index that was used for each separation.

More quantitative analyses of the residuals, for instance power spectra, standardized moments of the distributions, mainly confirm these general findings, but turned out to be not very effective in discriminating among the models, as the results were comparable.

This means that, in our case, each model allows a satisfactory decomposition of the data, at least for a subset of synchrotron spectral indices. Nevertheless, some of the models could still give incorrect descriptions of the data. In fact, the analysis of the residuals is not very informative about the reliability of the individual reconstructed components. For example, they may be affected by

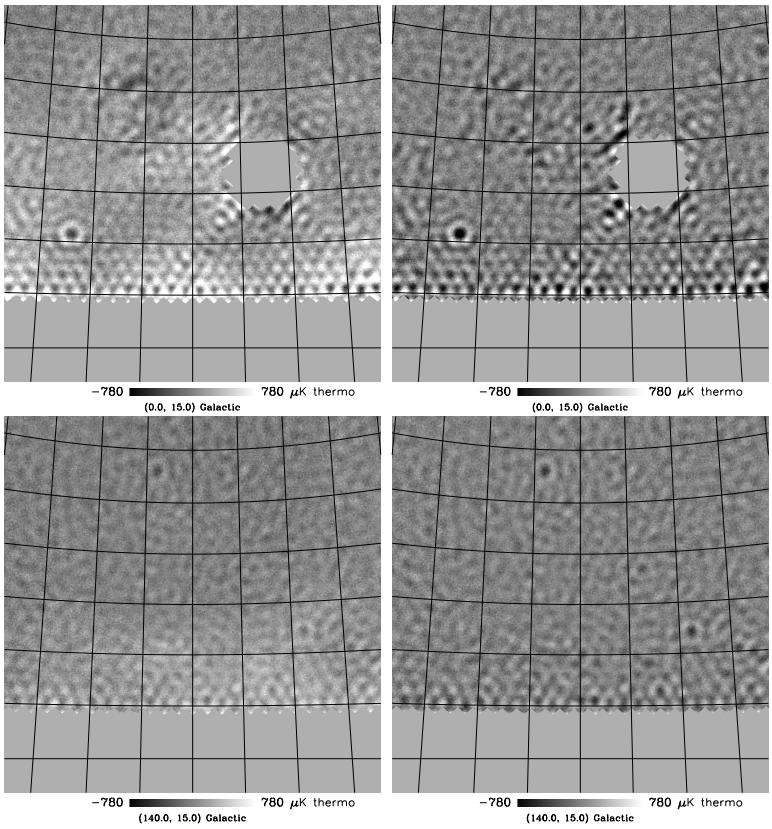

Figure 5.9: Residual at K band for model **M1** (left) and **M2** (right) assuming $\beta_s \sim 3$ in two regions of $\sim 40\times40$ degrees. Central coordinates of the patches are $l = 0°$, $b = 15°$ (up) and $l = 140°$, $b = 15°$ (down).

aliasing which does not show up in the residuals. To investigate this possibility, we applied other quality tests to the reconstructed components directly.

Correlation among the components

Independent observations have highlighted positive correlations of varying strengths among synchrotron, free-free and dust emissions, ensuing from the physical processes producing them. Therefore, the reliability of the recovered components can be tested by investigating their mutual correlations.

We have worked with pixels of area $0.84\,\mathrm{deg}^2$ (Nside = 64). We trimmed all pixels preprocessed through the apodized mask of Figure 5.7 as well as pixels within a radius of 1° around each point source listed in the WMAP three-year catalogue. We also excluded a region with a radius of $\sim 15^\circ$ around the Gum Nebula, as in this region the separations are always very noisy. High Galactic latitude regions ($|b| > 50^\circ$), where foregrounds are weak and therefore recovered with low signal to noise ratios, have also been excluded from the analysis. Around $3 \cdot 10^4$ pixels remain.

For each model we have computed the correlation coefficients, r, among the recovered Galactic components for each of the thirty separations. Whenever one of those coefficients was found to be negative, the corresponding separation was discarded. The percentages of discarded separations for each model are reported in Table 5.3. They are generally low ($\leq 10\%$), except in the case of **M3** (30%). All the models including the anomalous component feature very strong positive correlations of it with thermal dust ($r \sim 0.8$), somewhat less strong but still highly significant positive correlations with synchrotron ($r \sim 0.6$), and weak positive correlations with free-free ($r \sim 0.25$).

For the large number of pixels we are dealing with, $N \simeq 3 \times 10^4$, the correlation coefficient, r, for samples of uncorrelated quantities has a normal distribution with zero mean and $\sigma_r = 1/\sqrt{N}$. CMB and Galactic foregrounds are intrinsically uncorrelated; therefore, the presence of a statistically significant correlation among them indicates a poor component separation. Thus, a good criterion to evaluate the quality of the separations is to compute the correlation coefficient between the reconstructed CMB and foreground maps. The latter have been obtained as the sum of the reconstructed components scaled to the Q and V bands. As in these bands the foreground contamination has a minimum, those correlations are expected to be low and, hopefully, not statistically significant. Once computed for each separation and each model, the correlation coefficients can be used as figures of merit for comparing different models and, for a given model, to identify the best separations.

In Figure 5.10 we show the absolute values of the correlation coefficients as a function of the assumed synchrotron spectral index. The horizontal dashed line is the 3σ significance level. Model **M3** always features highly significant correlations ($r > 0.1$) between the CMB and the reconstructed foreground contribution in both bands, much stronger than found for the other models. This result, together with the high number of samples we had to discard due to aliasing effects, indicates that this model is not able to correctly describe the data. It was therefore discarded together with model **M4** which also yields values of

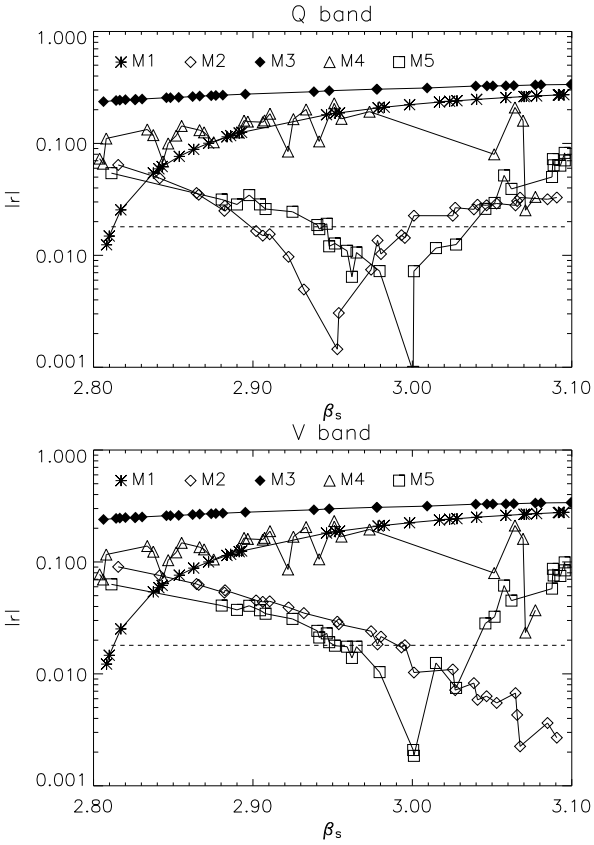

Figure 5.10: Absolute values of the correlation coefficient between the recovered CMB and the total foreground map for the Q (up) and V (down) bands as a function of the synchrotron spectral index. Values above dashed line correspond to correlations formally significant at $\geq 3\sigma$.

Table 5.3: Percentage of discarded separations because of negative correlation coefficients.

Model	Discarded separations
M1	0%
M2	6%
M3	30%
M4	10%
M5	3%

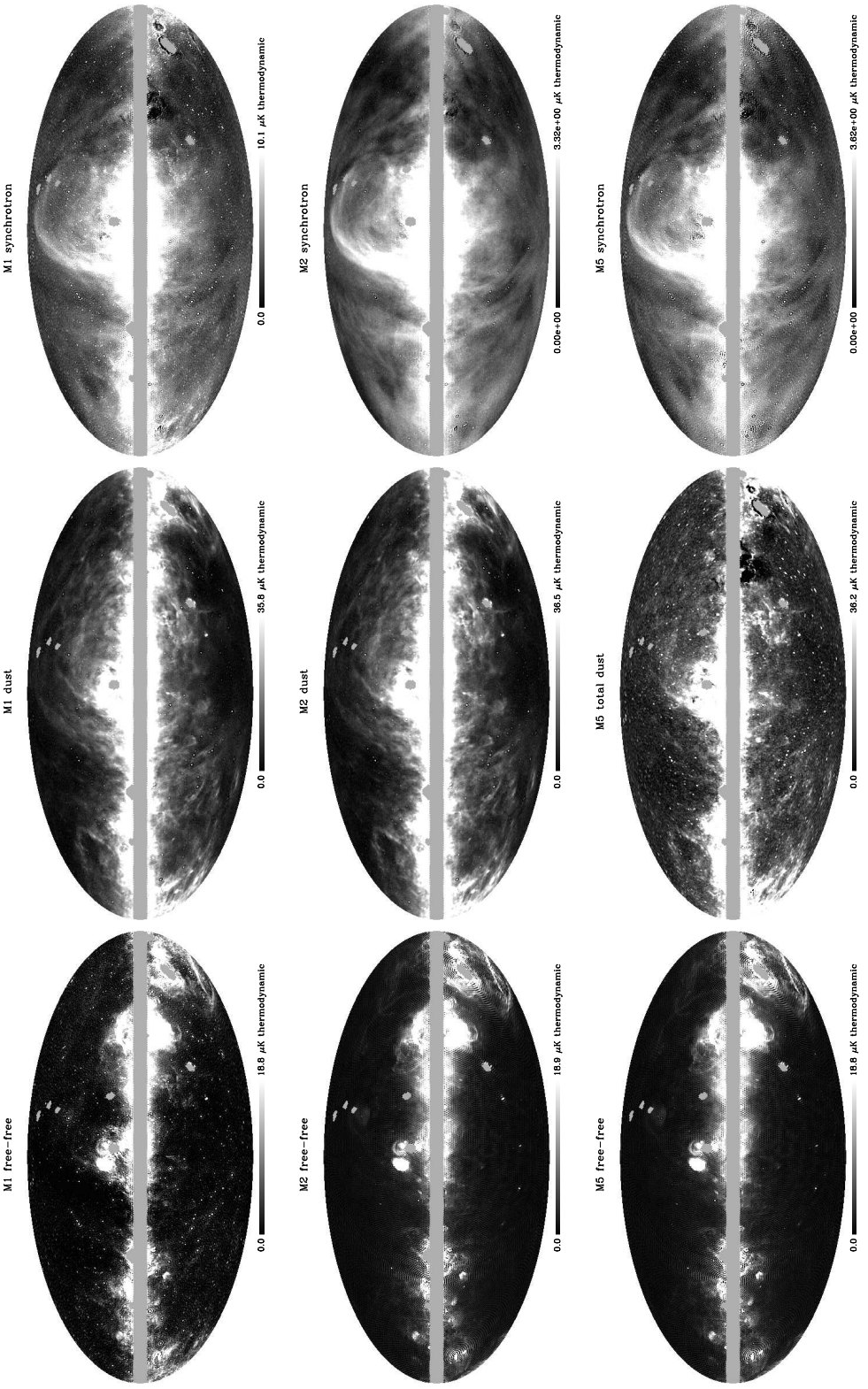

Figure 5.11: Foreground components recovered for models **M1**, **M2** and **M5**.

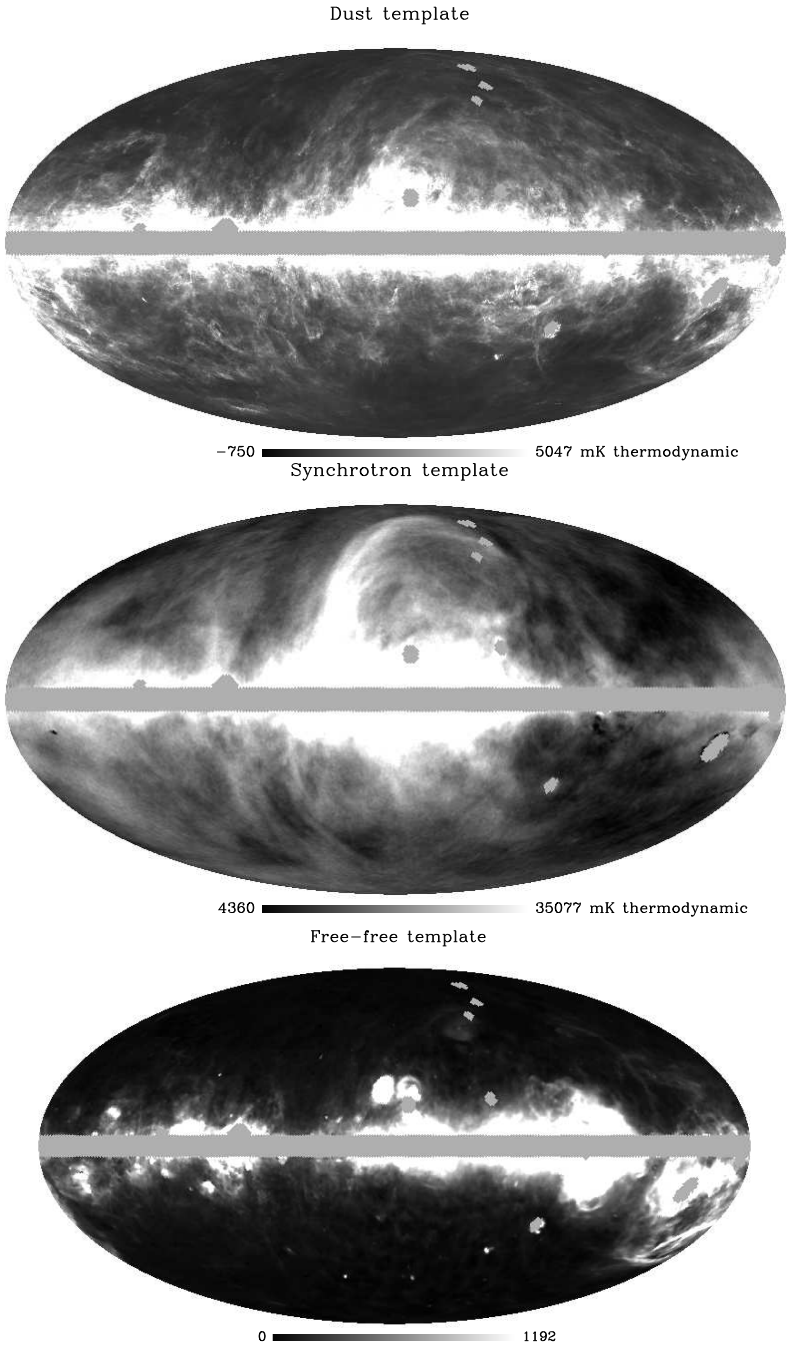

Figure 5.12: Dust (850 GHz), synchrotron (408 MHz) and free-free (408 MHz) templates exploited for the WF source reconstruction. The maximum value of the color scales is the mean of the map plus one standard deviation.

Table 5.4: Correlation coefficients of the reconstructed CMB components with the foreground templates: minimal mask, (kp2 mask)

Template	**M1**	**M2**	**M5**
Thermal dust	0.027 (0.015)	0.029 (0.023)	0.025 (-0.023)
Synchrotron	-0.054 (-0.046)	-0.016 (-0.012)	-0.015 (-0.010)
Free-free	-0.035 (-0.021)	-0.035 (-0.0003)	-0.044 (-0.011)

Table 5.5: Correlation coefficients of the synchrotron, thermal dust and free-free maps with the corresponding templates. We recall that for **M5** the dust component includes both the thermal and the anomalous contributions.

Template	**M1**	**M2**	**M5**
Thermal dust	0.966	0.967	0.883
Synchrotron	0.865	0.858	0.851
Free-free	0.957	0.984	0.984

$|r|$ always well above the 3σ limit, although somewhat below those found for **M3**.

In the case of models **M1**, **M2** and **M5**, the test shows that the correlations are not statistically significant for well defined ranges of the synchrotron spectral index. Model **M1** requires relatively low values of β_s, below that expected, in the WMAP frequency range, from the locally measured energy spectrum of relativistic electrons which would yield $\beta_s \simeq 3$ (Banday & Wolfendale 1990, 1991), as indeed found for models **M2** and **M5**.

We have built reference maps of each reconstructed component for each of the three surviving models by averaging those reconstructions with foreground–CMB correlations at less than 3σ level. For model **M2** we find somewhat different allowed ranges of β_s for the Q and the V bands, and we have kept the reconstructions in the union of the 2 ranges, i.e. with $2.9 \leq \beta_s \leq 3.1$. In Table 5.4 we list the correlation coefficients of the reference CMB map for each model with the foreground templates. The correlations computed with the minimal mask are formally statistically significant, indicating the presence of residual foreground contamination. The major contributions to the correlation coefficients come from regions close to the Galactic plane. If we adopt the WMAP kp2 mask, in place of our minimal mask, the correlation coefficients decrease, sometimes going close to or below the 3σ significance level, especially for free-free. More details on the reconstructed CMB will be given in § 5.6.

Table 5.6: Correlation coefficients of the anomalous emission (**M2**) and of the total dust component (**M5**) with all the foreground templates.

Template	**M2**	**M5**
Thermal dust	0.823	0.883
Synchrotron	0.664	0.711
Free-free	0.294	0.221

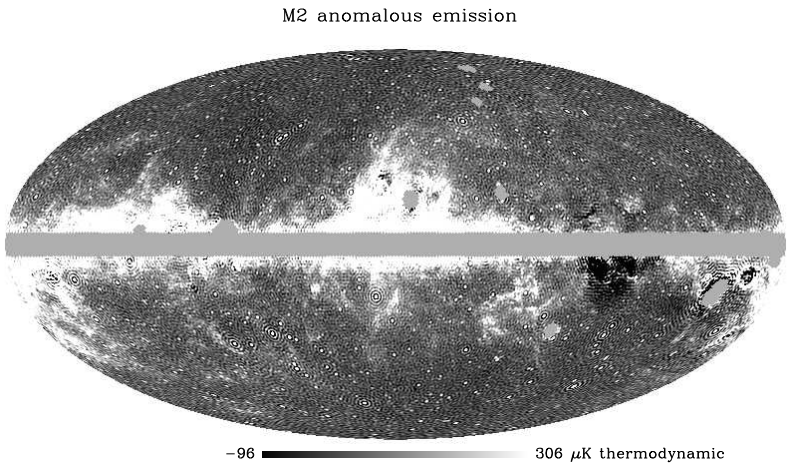

Figure 5.13: Map of the anomalous emission recovered with model **M2** in the K band. The color scale has been restricted to the mean of the map plus/minus one standard deviation.

In Fig. 5.11 we show the foreground components recovered for models **M1**, **M2** and **M5**, which can be compared with the templates shown in Fig. 5.12. The correlations of the recovered maps with the corresponding templates are reported in Table 5.5. In general, the match between the prior and reconstructed maps is good but not perfect, as expected given the spatial variations of the spectral properties. We note however that in the case of **M1**, for which no anomalous emission component has been assumed, the recovered synchrotron and free-free maps appear to be less clean and less similar to the corresponding templates. This may be due to the fact that in this case the anomalous component mixes with synchrotron and free-free in the reconstructed maps. As shown by both the visual inspection and the correlation analysis, the total dust map recovered for **M5** differs from the other reconstructed dust maps and from the corresponding template. This indicates that the low frequency component of total dust is likely to be relevant in the WMAP bands.

5.5 Results on the anomalous emission

Given the astrophysical interest of this subject, in this section we provide more details on the results obtained on the anomalous emission. Table 5.6 gives the correlation coefficients between the anomalous emission recovered with model **M2**, and the thermal dust plus anomalous emission recovered with model **M5** (which treats them as a single component with a complex spectrum), and the foreground templates. The additional component turns out to be always tightly correlated with thermal dust although, if its spatial distribution is unconstrained, the correlation is not perfect, with a correlation coefficient $r \simeq 0.8$. This reminds us of the suggestion by Davies et al. (2006) that, if this component is due to spinning dust, it should be better correlated with the small

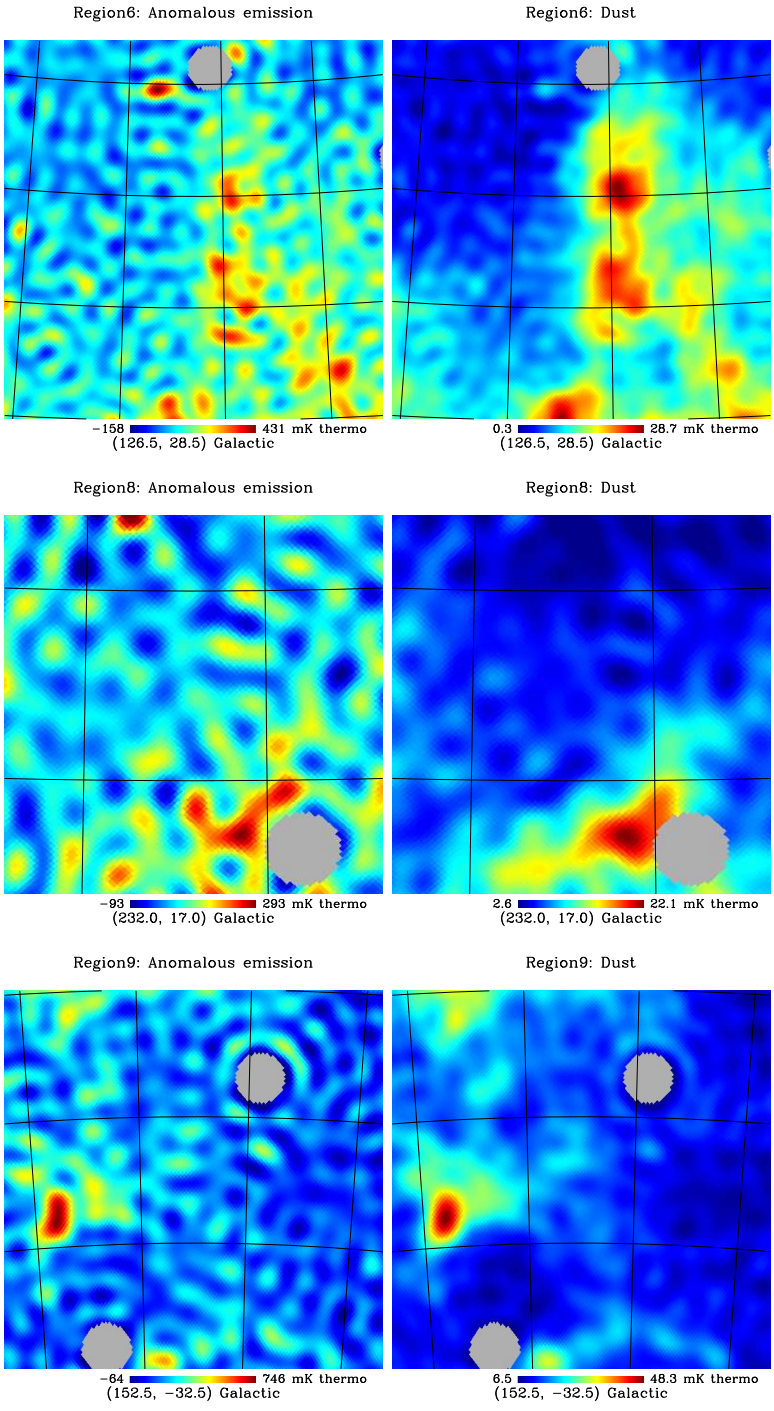

Figure 5.14: Morphological comparison between recovered components in three dust dominated regions of Davies et al. (2006). Left: anomalous emission at K band; right: dust at W band. The graticule spacing is 5 degrees.

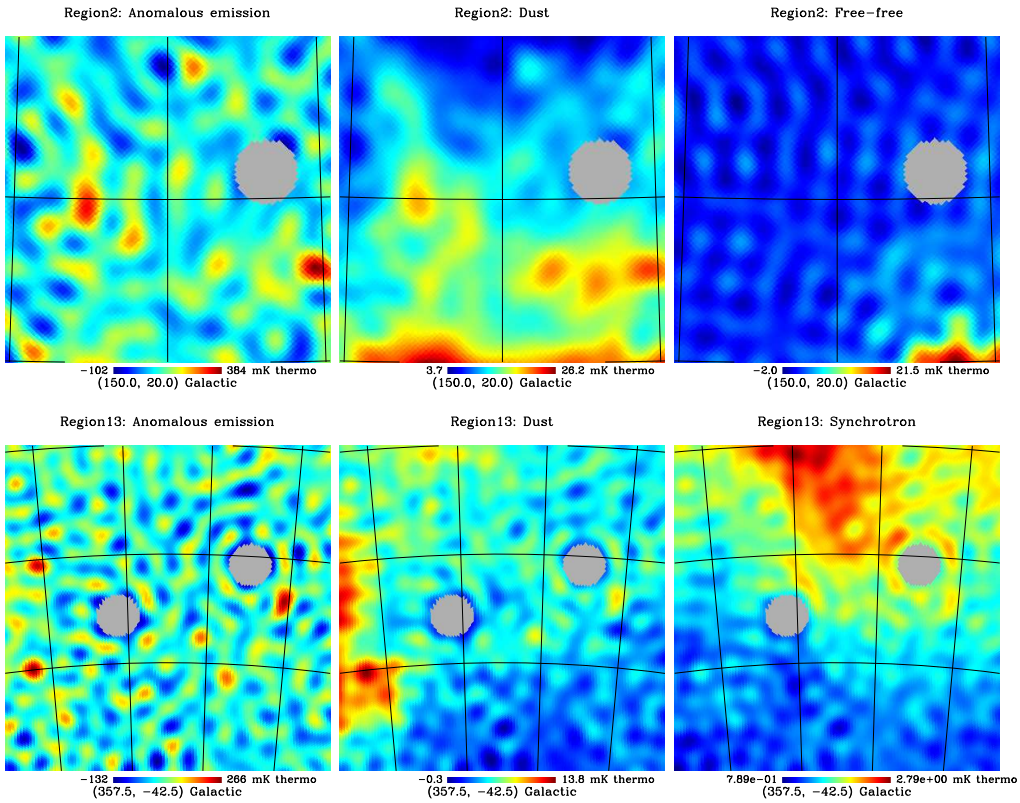

Figure 5.15: Morphological comparison between recovered components in two regions of Davies et al. (2006) dominated by free-free and synchrotron respectively. Left: anomalous emission at K band; center: dust at W band; right: dominant component at W band. The graticule spacing is 5 degrees.

grains dominating the mid-IR emission than with the big grains dominating at far-IR to sub-mm wavelengths. The additional component is also well correlated with synchrotron, with a correlation coefficient $r \simeq 0.6$, and more weakly correlated with the free-free, although the free-free is strongly correlated with thermal dust, with a correlation coefficient $r = 0.4 - 0.6$.

As already explained, models **M2** and **M5** adopt an identical model for the frequency scaling of the anomalous emission. However, in the latter case this component is included in the dust parametrization and has therefore exactly the same spatial distribution of thermal dust. The map of the anomalous emission yielded by model **M2** could then constitute its first, albeit preliminary all-sky template. The proposed frequency scaling for this component is given by eq. (5.1), with m_{60} given by the best fit values of eq. (5.2).

The final map of the anomalous component recovered with model **M2** is shown in Figure 5.13. Traces of imperfect component separation can be discerned by eye: negative imprints in correspondence of the Gum Nebula, of the Orion region and of the north Polar Spur, as well as several point-like sources. Nevertheless, the similarity with the thermal dust map is evident; we recall that no prior correlation of the anomalous emission with thermal dust was imposed. Differences with the spatial distribution of synchrotron are also clear: the anomalous emission is relatively stronger towards the outskirts of the Galaxy, where the first application of CCA found flat "synchrotron" spectral indices, and less prominent near the Galactic center.

To go in more details on the morphological properties of the reconstructed anomalous emission map, we analysed it in the 15 fields of Davies et al. (2006). These regions, having sizes ranging from $\sim$60 to $\sim$1000 square degrees, were selected requiring that only one of the three foregrounds (free-free, dust and synchrotron) was dominant in each field. This criterion can be satisfied at intermediate Galactic latitudes, well away from the Galactic plane where foregrounds are all strong.

The approach of Davies et al. (2006) was to compare the emission at each WMAP frequency with the foreground templates in each field. A first analysis, based on scatter plots (T-T analysis), showed a strong correlation between the WMAP K and Ka bands with the thermal dust template in most of the fields. They also used a cross-correlation method (C-C analysis) to fit more templates simultaneously to the WMAP data, thus estimating the mean amplitude of each identified foreground component in the WMAP bands. The low-frequency dust-correlated emission is found to be the dominant foreground at K band.

In Figure 5.14 we show a comparison between the thermal dust and anomalous emission maps recovered with **M2** in three of the five fields that were selected to be dust-dominated. These regions are found to produce the most significant correlations by Davies et al. (2006). In agreement with their results, the anomalous emission is detected in these regions, and appears to be dust correlated.

In Figure 5.15 we show a free-free dominated region and a synchrotron dominated one. The comparison is between the reconstructed anomalous emission, dust and the dominant component. These regions are poorly contaminated by dust and we expect that the same holds also for the anomalous emission, as it is

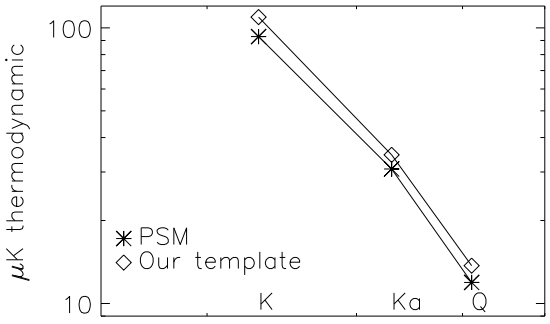

Figure 5.16: Comparison of intensities of the anomalous emission component implemented in the PSM and the results by our analysis on the WMAP data.

dust correlated. Although the anomalous emission is reconstructed with lower signal to noise, the similarity with dust is still present, even if it is less evident. Moreover we note that the dominant component always shows a distinct morphology, indicating that the reconstructed anomalous emission is not strongly contaminated.

5.5.1 Anomalous emission in the PSM

The first exploitation of our results on the anomalous emission has been to help implementing a model for this component in the PSM. Despite the presence of this emission were broadly accepted within the PLANCK group, it has not been included yet in the sky model, given the lack of information necessary for a plausible description. The situation has improved after the release of the three-year WMAP data. As mentioned above, the results of our analysis (Bonaldi et al. 2007a) provided the first observationally constrained almost all-sky template of this emission. Our results are in agreement with some findings of Hinshaw et al. (2006), in particular with the fact that the anomalous component is remarkably well correlated with thermal dust and more longitudinally extended than the Haslam et al. (1989) synchrotron template. Moreover, as already mentioned, our best fit relation is consistent with Davies et al. (2006).

Despite these successes, the direct exploitation of our recovered anomalous emission model in the PSM was not straightforward. The problems are in particular related to our template. First of all, it is not a full-sky map, as we miss, together with other small regions, a strip on the Galactic Plane. Then a direct visual inspection shows that this map is affected by contamination due to synchrotron (especially in the north Polar Spur region) and free-free (especially in the Gum region). The contamination introduces local spurious correlations between the anomalous emission and the other foregrounds, which can affect

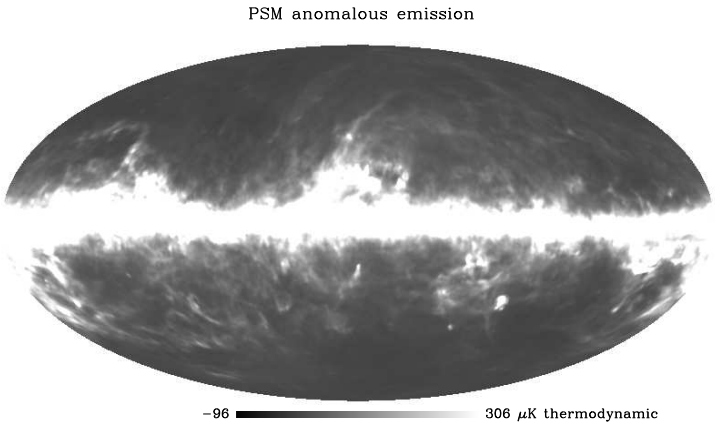

Figure 5.17: PSM anomalous emission at the K band; the color scale is the same of fig. 5.13.

the component separation. Finally, point sources should be removed from the map, and doing it properly requires an accurate work. For this reason, the PSM group agreed to rely on a theoretical model to provide a template and a frequency dependence for the anomalous emission, and to validate the model through the comparison with our findings. As discussed in § 4.3.1, the anomalous emission PSM model, developed by C. Dickinson, exploits the Schlegel et al. (1998) thermal dust map modulated by the dust reddening E(B-V) as a template, and the Warm Neutral Medium (WNM) spinning dust model by Draine & Lazarian (1998) for the frequency scaling. The intensity of the component was estimated by calculating the power spectrum of the spinning dust map at K-band, scaled to match the correlation analysis of Davies et al. (2006) for the Kp2 mask.

In Fig. 5.16 we compare the intensity of the PSM model at the K, Ka and Q band with that of our best fit model, computed for a mean synchrotron spectral index $\beta_s = 2.8$, as assumed in the PSM. It can be seen that, even if both the amplitude and the frequency dependence have been obtained independently, they are in very good agreement. We computed the correlation coefficient between the two maps in the same way described in § 5.4.1, and found $r \sim 0.85$. As the PSM anomalous emission template is only slightly different from the thermal dust template, this value is close to what reported in Table 5.6. However we note, as a confirmation of the model, that the correlation of our anomalous emission map with the PSM map is slightly higher than what found with the thermal dust template. In Fig. 5.17 we show the PSM anomalous emission template at the K band. The morphology of the PSM template appears to be very similar to that of our anomalous emission, reported in Fig. 5.13. The higher discrepancies are in correspondence to the Gum Nebula and to the Ophiuchus complex, where we know that our reconstruction is bad. Our template then exhibits an excess power near the Galactic center. In this region, our map resembles more the thermal dust template than the anomalous emission one.

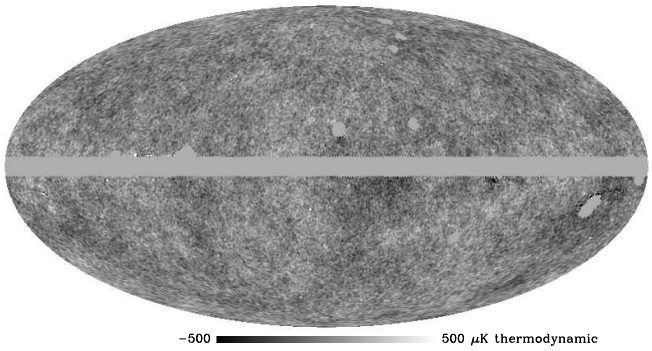

Figure 5.18: CMB map reconstructed with model **M2**.

In conclusion, the analysis we just described validates the anomalous emission model implemented in the PSM, which is a good starting point for the modeling of this emission.

5.6 The CMB power spectrum

After a discussion on the anomalous emission, in this section we focus on the CMB component, which is the main target of component separation. The analysis reported in § 5.4 allowed us to discard some of the foreground models we introduced for the WMAP data (**M3** and **M4**), but showed that we cannot discriminate between other ones, even if they are quite different. In particular, models **M1**, **M2** and **M5** provided CMB maps of comparable quality. As an example, in Fig. 5.18 we show the CMB map recovered for **M2**, which appears to be clean even at low latitudes.

Now, we wish to address the following question: to what extent do the different foreground models affect the estimates of the CMB power spectrum on large scales, where possible inconsistencies with predictions of the standard cosmological paradigm have been reported? We will focus our analysis on $\ell \leq 70$, where the effect of fluctuations due to unresolved point sources, not included in our study, can be neglected. On large scales, however, the CMB maps reconstructed through matrix inversion of the WMAP data complemented with the three template foreground maps, keep trace of the spurious structure due to the latter maps being mosaics of observations. This is clearly visible in Figure 5.19 showing the power spectra of the templates at low multipoles. While for $\ell \geq 10$ the power spectra are smooth, at lower multipoles there are conspicuous spikes, particularly for the free-free and the synchrotron. To avoid this problem, the CMB power spectrum for $\ell < 10$ was computed using only the WMAP data for the Wiener Filter reconstruction of the CMB, still using the same ranges of optimal spectral parameters for each model. For larger ℓ's the inversion is carried out including the foreground templates. An error analysis, carried out as described in Bonaldi et al. (2006), confirms that this approach significantly decreases the errors on the power spectrum at low ℓ's. The power spectra obtained with the two methods are very close to each other for $\ell \simeq 10$, so that

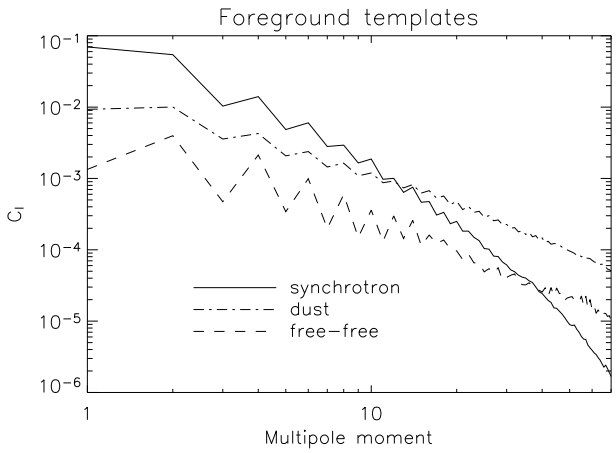

Figure 5.19: Full-sky power spectra of the foreground templates at low multipoles (arbitrary normalizations.)

they smoothly join and the choice of the boundary multipole does not need to be fine tuned.

In these calculations we used two sky masks. The first one, a minimal mask, excludes all pixels having non unit value in the apodized mask used to preprocess the data (Figure 5.7); the cut region amounts to about 10% of the sky. The second is the minimal mask multiplied by the WMAP kp2 mask; it excludes around 20% of the sky. The latter is less liable to residual foreground contamination, while the former is less liable to biases due to incomplete sky coverage. The power spectrum was binned with the same scheme adopted by the WMAP team and we applied the MASTER approach (Hivon et al. 2002) to obtain unbiased estimates.

The results for each model are shown in Figure 5.20, where we have plotted the power spectra computed with the minimal mask for $\ell \leq 8$ and those computed with the other mask for higher multipoles. Again the results are weakly dependent on the choice of the mask, but the minimal mask yields smaller oscillations at low ℓ's. We generally find good agreement with the WMAP power spectrum, shown by the solid line. However there are significant differences among the various models at the lowest multipoles, especially evident for $\ell = 2$. This result shows that the choice of the model for the Galactic components used to perform component separation can affect the CMB power spectrum on large scales. As an estimate of uncertainties associated to foreground modeling, we can take the spread of our three CMB power spectra.

In the upper panel of Figure 5.21 we compare our results with the WMAP three year power spectrum and with the best fit ΛCDM model based on WMAP data only (Spergel et al. 2006). The mean quadrupole moment resulting from our analysis is higher than the WMAP estimate, and the difference with the prediction of the ΛCDM model is within the uncertainty due to cosmic variance. The spread of estimates of the quadrupole moment from different models is around $\pm 200 \mu \mathrm{K}^2$.

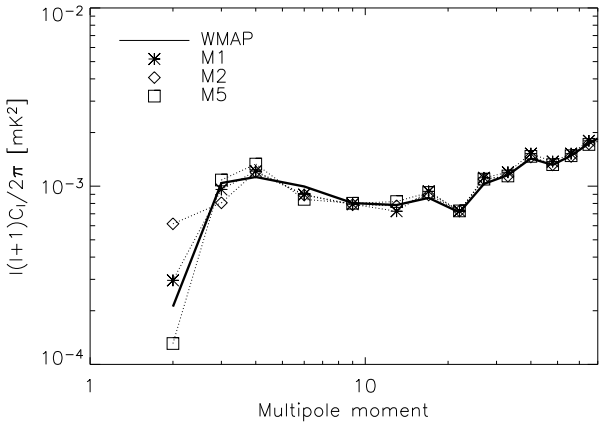

Figure 5.20: Binned CMB power spectra obtained from all models compared to the WMAP three-year power spectrum.

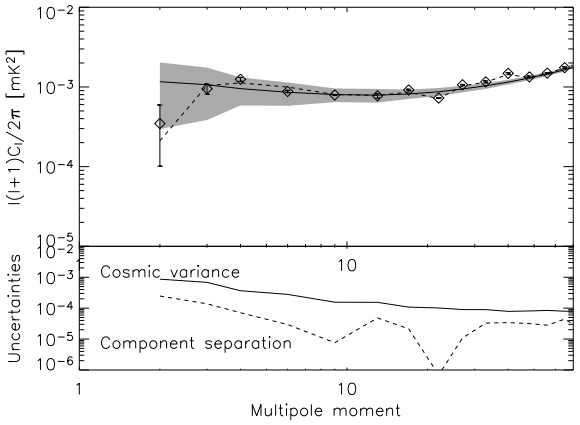

Figure 5.21: Upper panel: best fit ΛCDM model (smooth solid line) compared to the WMAP CMB power spectrum (dashed line) and to the mean final power spectrum resulting from our analysis (open diamonds; the error bars show the spread of results for different models). The shaded area shows the cosmic variance. Lower panel: uncertainties associated to foreground modeling (dashed line) compared to the cosmic variance (solid line).

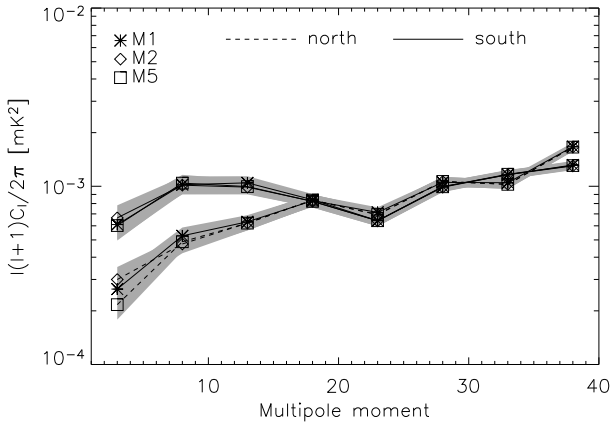

Figure 5.22: North-south asymmetry. The bins adopted have central multipoles $\ell = \{3, 8, 13, 18, 23, 28, 33, 38\}$ and equal width $\Delta\ell = 5$.

Summing in quadrature the cosmic variance and the modeling errors, we find no large scale power spectrum "anomalies" significant at $\geq 1.5\sigma$, except for the excess power at $\ell \simeq 40$, which is significant at around the 4σ level.

We also checked whether the modelization errors could have a significant role on the north-south asymmetry at $\ell \leq 20$. We computed for each model the power spectra for the north and the south hemisphere separately in a way analogous to the one we previously described, except for the different binning scheme adopted. As shown in Figure 5.22, the north-south asymmetry remains, independent of the foreground model adopted.

Chapter 6

Discussion and conclusions

6.1 Introduction

The work described in this Thesis is related to the PLANCK mission, scheduled for launch in october 2008, which will observe the microwave sky with unprecedent resolution and sensitivity. The PLANCK collaboration involves hundreds of scientists. Our group is deeply involved in the development and testing of algorithms for component separation. This is a crucial step of the data reduction process, as it aims at getting separated maps of the different astrophysical components which are mixed in the nine observational channels of PLANCK. The main target is to provide a map as clean as possible of the Cosmic Microwave background (CMB) radiation, from which the relevant cosmological information will be derived. Moreover, there is a lot of scientific information contained in the maps of the other astrophysical components, mainly diffuse emissions due to our own Galaxy and point-like emissions due to extragalactic objects. It is obvious that none of the scientific objectives of PLANCK can be achieved without a component separation process, whose accuracy will ultimately set that of the final results PLANCK will provide.

Our work is mainly dedicated to the development and testing of a new method for the separation of diffuse foregrounds, the Correlated Component Analysis (CCA), proposed by Bedini et al. (2005). After having implemented the method, we tested it on simulated PLANCK data with good results. We also applied our method to the three year data of the WMAP mission, with very interesting findings on the diffuse components present in the data and the impact of modelization errors on the determination of the CMB power spectrum.

A minor part of this Thesis is devoted to the study of the SZ effect from galaxy clusters, which is part of the CMB signal and is one of the main scientific motivations of the PLANCK mission. In particular we investigated how different modelizations for the physics acting in the intra-cluster medium affect the observable properties of SZ clusters.

In this Chapter we present a summary and a critical discussion of this work, which highlights the main conclusions and future developements.

6.2 Development and testing of CCA for PLANCK.

The Correlated Component Analysis (CCA), proposed by Bedini et al. (2005), is a technique which estimates the spectral parameters of the diffuse components mixed in the data exploiting second-order statistics. As discussed in Chapter 3, the spectral behavior of the components is the key ingredient to perform component separation of multi-frequency experiments. Once we have this information, the components can be reconstructed with different inversion methods, such as Wiener Filtering (WF) and Maximum Entropy Method (MEM).

We worked out a suitable implementation of the method and tested it on simulated PLANCK data, as discussed in Chapter 4. Our first tests, reported in Bonaldi et al. (2006), were aimed at assessing the performances of CCA and at defining suitable strategies for its exploitation on PLANCK data. We considered simulated observations of the microwave sky with angular resolution and white stationary noise at the nominal levels for the PLANCK satellite, and realistic foreground emissions, with a position dependent synchrotron spectral index. We worked with two sets of PLANCK frequency channels: the low frequency (LF) set, from 30 to 143 GHz, complemented with the Haslam 408 MHz map, and the high frequency (HF) set, from 217 to 545 GHz. As CCA works in pixel domain, all maps must be at the same resolution, which is necessarily the worst of the considered channel set. In particular, we worked with a beam of 33' for the LF set and of 5' for the HF set. For each channel set we applied CCA to sky patches and estimated the spectral indices of the synchrotron and dust emission. The main conclusions of this test are listed below:

- The best choice for the size of the patches is a trade-off between the spatial variability of the spectral dependencies, which calls for small patches, and the number of independent pixels needed to have a good statistics, which requires big patches. We found that when working with the LF set a suitable patch size is around $1500\,\mathrm{deg}^2$, while for the full PLANCK resolution allowed by the HF set we can work with a size of $400\,\mathrm{deg}^2$.

- Since the synchrotron and free-free spectral indices are not widely different, their separation is poor if we use only PLANCK data whose lower frequency channel is 30 GHz. Much better results are obtained taking into account the low-frequency map by Haslam et al. (1998).

- The concentration of intense free-free emission on the Galactic plane introduces a steep dependence of the spectral index of the global Galactic emission with Galactic latitude, close to the Galactic equator. This feature makes difficult for the CCA to recover the synchrotron spectral index in this region, given the limited angular resolution of PLANCK, especially at low frequencies. A cut of a narrow strip around the Galactic equator ($|b| < 3^\circ$), however, allows us to overcome this problem.

- The most accurate estimates of the spectral dependencies of foregrounds are obtained in the latitude range $[-30^\circ, +30^\circ]$, where these components are relatively strong.

We showed that, exploiting the above configuration, CCA allows an effective foreground subtraction, as illustrated by Fig. 4.4.

We then partecipated in a blind comparative test of component separation methods coordinated by the PLANCK working group on "component separation". The simulated maps contained, besides diffuse foregrounds with spatially varying spectral dependences, also point-like sources and SZ clusters. For this work we tested the strategy of estimating the mixing matrix with CCA and performing the source reconstruction with harmonic WF. One of the main issues was the presence of point sources, which we never addressed before. Given the short deadline for providing the results of the test, we could not perform our analysis after other groups had performed the source extraction. We found that a suitable strategy in this case is to mask only the brightest spots before the separation, and to apply a mask for point sources on the separated components. We estimated the frequency scaling of the diffuse components with CCA in nine different patches of the sky, selected at low latitude, where the foreground signal is strong enough. We then performed a set of full-sky reconstructions of the components with WF, one per patch, thus obtaining a set of maps for each separated component. We adopted as our best estimates for the maps of each component the average over the set of maps and estimated the associated error maps as their standard deviations. We focused on the reconstruction of the CMB map and on the power spectrum estimation, and obtained in both cases very good results, highly competitive with those obtained with the other methods (see § 4.5.2). We also provided good reconstructed dust maps at each PLANCK channel. The reconstruction of synchrotron and free-free maps was instead not satisfactory. This aspect certainly needs more work, as the presence of strong radio sources concentrated along the Galactic Plane made the separation of these components very noisy. We did not attempt to recover an SZ map. Even if the typical spectral signature of the SZ effect allows us in principle to disentangle this component using multi-frequency data, the signal is faint, so it is necessary to reduce all sources of contamination to get a reasonable signal-to-noise ratio.

The work reported so far demonstrates the validity of the method we developed. CCA allows effective foreground subtraction from temperature maps for the PLANCK mission, and is very competitive with the best techniques used so far. Of course, these encouraging results triggered more work on this subject, besides the investigation of the aspects we mentioned above. In the next section we report on recent developments of our work, which are now in progress.

6.2.1 Recent developments

Application to polarization data

Besides total intensity, PLANCK will also provide maps of the polarized signal. Component separation on polarized maps is in principle similar to that on temperature maps; however, it becomes in practice a different problem. First of all, the polarized signal has lower signal-to-noise ratio, which is often a critical quantity for component separation methods. Also, PLANCK will not provide

polarization for the two highest frequencies, so we are left with 7 channels, from 30 to 353 GHz. Polarization is also different from the point of view of the astrophysical components. Since free-free emission is intrinsically unpolarized, we have only two diffuse foregrounds to be removed, namely synchrotron and thermal dust emission. However, foregrounds are very poorly known in polarization, especially for what concerns the morphology of the emissions. Finally, the polarized CMB is very faint, at least one order of magnitude fainter than the temperature signal, so its detection is really challenging.

A first test of the method on simulated PLANCK polarized maps is currently in progress. This simulation obtains the PLANCK channel maps from the simulated time ordered data (TOD) through a mapmaking process. This allows in particular a more realistic treatement of the noise and the inclusion of some instrumental systematics. The simulation of the sky emissions is similar to what used in the previous tests, described in § 4.3.1.

The approach to component separation is similar to the one we adopted for temperature data: we first estimate the frequency dependence of the foreground components and then perform a source reconstruction exploiting the recovered information. On the other hand, given the weakness of the signal, a direct estimate of its frequency dependence is affected by large uncertainties. An alternative approach that we plan to test relies on the assumption that the frequency dependence in polarization is the same as in temperature.

Harmonic version of CCA

A frequency domain version of CCA, FD-CCA, has been recently proposed by Bedini et al. (2007). It can be applied both to little plane patches, exploiting the Fourier transforms, or to the full-sky, exploiting the spherical harmonics transforms. The formalization of the problem is similar to the one we presented in § 3.6.4. Eq. (3.57) becomes:

$$\tilde{\mathbf{C}}_{\mathbf{x}}(\ell) = \tilde{\mathbf{B}}(\ell)\mathbf{H}\tilde{\mathbf{C}}_{\mathbf{s}}(\ell)\mathbf{H}^T\tilde{\mathbf{B}}^{\dagger}(\ell) + \tilde{\mathbf{C}}_{\mathbf{n}}(\ell). \tag{6.1}$$

The matrices $\tilde{\mathbf{C}}_{\mathbf{x}}(\ell)$, $\tilde{\mathbf{C}}_{\mathbf{x}}(\ell)$ and $\tilde{\mathbf{C}}_{\mathbf{x}}(\ell)$ contain the cross-spectra of data, sources and noise respectively. The matrix $\mathbf{H}$ contains the frequency dependence of the mixed components, expressed as a function of a small set of parameters $\mathbf{p}$, and $\tilde{\mathbf{B}}(\ell)$ is the convolutional kernel that models the telescope angular response pattern for each measurement channel. After some manipulations, the previous relation can be rewritten as

$$\mathbf{d}(\ell) = \mathbf{H}_{\mathbf{k}}(\ell)\mathbf{c}(\ell), \tag{6.2}$$

where $\mathbf{H}_{\mathbf{k}} = [\tilde{\mathbf{B}}(\ell)\mathbf{H}] \otimes [\tilde{\mathbf{B}}(\ell)\mathbf{H}]$ and the symbol "$\otimes$" denotes the Kronecker product. For each ℓ, the left-hand side of eq. (6.2) can be estimated from the measured data and the known noise power spectrum. The right-hand side depends on the unknown spectral dependences through the matrix $\mathbf{H}_{\mathbf{k}} = \mathbf{H}_{\mathbf{k}}(\mathbf{p})$ and on the unknown source cross-spectra through the matrix $\mathbf{c}(\ell)$. The unknowns are estimated by solving the optimization problem:

$$[\hat{\mathbf{c}}(\ell), \hat{\mathbf{p}}] = \operatorname{argmin} \mathbf{\Phi}[\hat{\mathrm{c}}(\ell), \hat{\mathbf{p}}], \tag{6.3}$$

with

$$\mathbf{\Phi}[\hat{\mathbf{c}}(\ell), \mathbf{p}] = \sum_{\ell=1}^{\ell_{max}} [\mathbf{d}(\ell) - \mathbf{H_k}(\ell, \mathbf{p})\mathbf{c}(\ell)]^T \cdot [\mathbf{d}(\ell) - \mathbf{H_k}(\ell, \mathbf{p})\mathbf{c}(\ell)] + \lambda\Gamma[\mathbf{c}(\ell)]. \quad (6.4)$$

In the above expression, Γ is a regularization term included as the reconstruction of the power spectra is an ill-posed problem; λ is the usual regularization parameter.

A clear advantage of this version of CCA with respect to the original one is the possibility to handle frequency-dependent beamwidths, thus exploiting the full PLANCK resolution. Another advantage is that FD-CCA directly estimates the source power spectra, and in particular the CMB power spectrum, which is one of the mean targets of the CMB experiments.

In Bedini et al. (2007) a first extensive test of FD-CCA on a prototype code is presented. These preliminary results are found to be comparable to the ones obtained via the pixel-domain CCA; however a more systematic testing is needed to find definitive answers. We thus have implemented a code for this purpose and we plan to begin soon a testing phase.

6.3 Scientific results

In addition to the development and testing of component separation methods for PLANCK, an important part of this Thesis work dealt with a re-analysis of WMAP data (§ 6.3.1 and § 6.3.2) and with a study of one of the main sources of secondary anisotropies, i.e. the SZ effect (§ 6.3.3).

6.3.1 CMB power spectrum from WMAP data: impact of component separation

As already mentioned, the CMB power spectrum is exploited to derive all the main cosmological parameters. Thus, a correct estimation of the uncertainties affecting our power spectrum estimates is of the outmost importance. One source of error is related to the component separation process. In fact, component separation is never perfect, and this may result in systematic errors in the CMB power spectrum, thus limiting our ability to constrain the cosmological parameters.

In particular, we considered the errors on the CMB power spectrum inferred from WMAP data, due to our imperfect knowledge of the foreground components.

The analyses performed by the WMAP team (Bennett et al. 2003, Hinshaw et al. 2006) rely on the standard set of diffuse foreground components, namely synchrotron, thermal dust and free-free emission. Discrepancies are found between the synchrotron component as measured by WMAP and the 408 MHz map by Haslam et al. (1998), which are explained with an a strong spatial variability of the synchrotron spectral index. Moreover, synchrotron is found to be dust correlated at WMAP frequencies, and this is explained with association of synchrotron emission to dusty, star-forming regions.

Other analyses of the WMAP data (Finkbeiner 2004, de Oliveira-Costa et al. 2004, Davies et al. 2006) supported a different interpretation: an additional, dust-correlated component, the so-called "anomalous emission", is present at frequencies ≤ 40 GHz. One explanation of this emission is related to fast rotation of very small dust grains ("spinning dust" emission, Draine & Lazarian 1998). Once this component is accounted for in the data, the synchrotron emission in the WMAP bands is more similar to the 408 MHz template.

The subject we just described has certainly a great interest from the point of view of Galactic science, as we will discuss in § 6.3.2. For the moment we focus on the impact on the CMB component. The WMAP team performed component separation fitting templates of the Galactic emissions to the data, exploiting their model for such components. As we saw, however, other models are equally possible. Thus, it is likely that the choice of the foreground model reflects on the reconstructed CMB and on its power spectrum.

As we explained in the previous Chapter, in Bonaldi et al. (2007a) we performed such an analysis, especially in relation to the reported deviations from predictions of the "concordance" cosmological model (Spergel et al. 2006). Our approach was to perform component separation of the WMAP data with CCA combined with harmonic Wiener Filtering. The first step provides a model for the foreground components, in particular yields estimates of the parameters describing their spectral dependences. To account for modelization errors we tested more than one model: a standard one, without the anomalous emission, and four including different parameterizations for the additional component. After getting the reconstructed CMB for each model, we performed several quality tests in order to evaluate the compatibility of each of them with the data. This analysis allowed us to discard two of the models, so that we are left with the standard model and two models including the anomalous emission. We then compared the results obtained for the three surviving models in terms of the CMB power spectrum. In particular our analysis covers the range $\ell \leq 70$, where the effect of fluctuations due to unresolved point sources, not included in our study, can be neglected. The results are generally consistent with the WMAP estimates. However, the spread of values, that can be taken as an estimate of modelization uncertainties, is substantial for the lowest multipoles and becomes progressively smaller as ℓ increases. In particular, a substantial spread is found for the quadrupole moment, which is anomalously low according to the WMAP data. Combining the cosmic variance with the modeling errors, we find that the quadrupole amplitude is less than 1σ below that expected from the standard ΛCDM model. Also the other reported deviations from model predictions are found not to be statistically significant, except for the excess power at $\ell \simeq 40$. On the other hand, the north-south asymmetry is found to be unrelated to foreground modeling.

6.3.2 The microwave anomalous emission in the WMAP data

As previously mentioned, the analysis we just described also provided interesting results on the anomalous emission. For our analysis of the WMAP data with CCA we adopted different models for its frequency scaling. Following Ben-

nett et al. (2003) and Hinshaw et al. (2006), the anomalous emission might be interpreted as flat-spectrum synchrotron, possibly highly self absorbed, associated with strong magnetic fields local to star-forming regions (and thus dust-correlated). To investigate this possibility we parametrized this component as a power law. We then adopted the parametrization proposed by Tegmark et al. (2000) to fit typical Draine & Lazarian models: a grey body of the form of equation (2.3), with temperature around 0.25 K and emissivity index around 2.4. We also proposed a further parametrization, which is able to fit the results by de Oliveira-Costa et al. (2004), Watson et al. (2005) and Davies et al. (2006): a parabola in the $(\log\nu, \log S)$ plane with a maximum at 20 GHz. We finally tested the possibility that there is a perfect correlation between thermal dust and anomalous emission, so that they can be treated as a single component. The latter is parametrized as the standard thermal dust plus another term, with the same parabolic parametrization, multiplied by an additional free parameter, the relative amplitude of the two contributions.

After the estimation of the free parameters for each model and the source reconstruction with WF, our quality tests showed that the latter two models for the anomalous emission should be preferred to the previous ones. Thus, the frequency dependence of the anomalous emission in the CMB range is found to be different from a power law but also from typical Draine & Lazarian models. For both the "good" models the WF reconstruction allowed us to get, besides the CMB maps we analysed in the previous section, also the foreground maps. In particular, while one model provided a map of thermal plus anomalous dust, the other one allowed us to obtain a separate map of the anomalous component. This constitutes the first, albeit preliminary, template of this emission, which by now has been directly detected only in limited regions of the sky. Traces of imperfect component separation can be discerned by eye in this map (see Fig. 5.13), especially in correspondence of the Gum Nebula, of the Orion region and of the north Polar Spur. Nevertheless, the similarity with the thermal dust map is evident, and this is remarkable since no prior correlation of the anomalous emission with thermal dust was imposed. In particular, the correlation coefficient between the thermal dust map and the anomalous emission turned out to be around 0.8. As noted by Davies et al. (2006), if this component is due to spinning dust, it should be even more tightly correlated with the emission from small grains dominating in the mid-IR. We also compared our findings on the anomalous emission with the theoretical model of this component recently developed by C. Dickinson to be included in the PLANCK sky model (see § 4.3.1 and § 5.5.1). Our findings are in good agreement with the PSM model, for what concerns both the template and the frequency scaling. In conclusion, our analysis allowed us to shade light on the anomalous microwave emission, and our results are likely to be useful for subsequent research on this component.

6.3.3 SZ effect from galaxy clusters

Another important scientific motivation of PLANCK is related to the detection of galaxy clusters through the SZ effect. As we discussed in § 2.5, the number distribution of these objects in mass sensitively depends on the dark matter

density fluctuations of the Universe. Moreover, galaxy clusters trace the large scale structure of the Universe, and thus can give important insights on structure formation. Another important research field related to the study of the SZ emission from galaxy clusters is to probe the physics of the intra-cluster gas. Galaxy clusters contain a gas component which has a temperature around 10^8 K. In a simplified picture, the potential energy lost by the gas when falling into the dark matter potential well is converted into thermal energy. In reality, the situation is more complicated, as during the compression of the gas other processes, like dissipation, thermal conduction, cooling and energy feedback are likely to operate. Such processes can be investigated in a statistic sense through the analysis of the "scaling relations" for a large sample of clusters. Assuming that the intra-cluster medium is in hydrostatic equilibrium in the dark matter potential well, a set of relations between various cluster properties, like mass, cluster temperature, X-ray and SZ flux can be derived. Discrepancies between the predicted and observed scaling relations can thus be used to investigate processes acting in the intra-cluster medium.

Given its full sky coverage and sensitivity, PLANCK is expected to detect thousands of clusters. Combining the PLANCK data on SZ clusters with other data, for example in the X-ray band, it will be possible to accurately investigate the gas physics through the study of the scaling relations. In order to correctly interpret the data, however, it is necessary to calibrate all these observables.

As described in § 2.5.2, in Bonaldi et al. (2007b) we investigated the effect of different modelizations of the gas physics on the scaling relations between the SZ flux and other intrinsic properties of clusters. For this purpose, we used a set of high-resolution hydrodynamical simulations, where clusters were re-simulated including different physical processes, from radiative cooling, to star formation, energy feedback from supernovae, and thermal conduction. We find that the scaling relations between cluster SZ emission and cluster X-ray luminosity and the cluster temperature evolve with redshift almost self-similarly out to $z = 1$; this result is consistent with previous works (Da Silva et al. 2004, Motl et al. 2005, Nagai 2006). Some deviations from self-similarity were found. However, in agreement with previous studies (White et al. 2002, Nagai 2006), the ICM physics has little effect on the slopes of the scaling relations. The main effect introduced in the scaling relations by radiative cooling is a lower normalization, by at least $20 - 30$ per cent, as also found by Nagai (2006).

Another research project in which we were involved (Dolag et al. 2006) concerns the possibility of detecting through the SZ effect the so-called cosmic web, the filamentary network of density enhancements present in the primordial field that are sharpened by the gravitational collapse. These anisotropic structures are confirmed to produce SZ signals; however the level is low, so that a firm detection will be challenging for future observations. However, projection of the filamentary network is found to bias the observational properties of galaxy clusters. In particular, the observed intensity of clusters can increase by up to 30%.

Publications

- K. Dolag, M. Meneghetti, L. Moscardini, E. Rasia, A. Bonaldi (2006) "Simulating the physical properties of dark matter and gas inside the cosmic web", MNRAS, 370, 656-672.
- A. Bonaldi, L. Bedini, E. Salerno, C. Baccigalupi, G. De Zotti, (2006)"Estimating the spectral indices of correlated astrophysical foregrounds by a second-order statistical approach", MNRAS,373, 271-279
- A. Bonaldi, G. Tormen, K. Dolag, L. Moscardini (2007b) "SZ profiles and scaling relations: modelling effects and observational biases", MNRAS, 378, 1248-1258
- A. Bonaldi, S. Ricciardi, S. Leach, F. Stivoli, C. Baccigalupi, G. De Zotti (2007a) "WMAP 3yr data with CCA: anomalous emission and impact of component separation on the CMB power spectrum", MNRAS, 382, 1791-1803

Bibliography

[Aarts and Korst, 1989] Aarts, E. H. L. and Korst, J. (1989). *Simulated annealing and Boltzmann machines. A stochastic approach to combinatorial optimization.* Chichester, New York: Wiley, 1989.

[Aghanim and Forni, 1999] Aghanim, N. and Forni, O. (1999). Searching for the non-Gaussian signature of the CMB secondary anisotropies. *A&A*, 347:409–418.

[Allen et al., 1987] Allen, T. J., Grinstein, B., and Wise, M. B. (1987). NonGaussian density perturbations in inflationary cosmologies. *Physics Letters B*, 197:66–70.

[Alton et al., 1998] Alton, P. B., Davies, J. I., and Trewhella, M. (1998). The distribution of far-infrared emission from edge-on galaxies. *MNRAS*, 296:773–784.

[Amendola et al., 2002] Amendola, L., Gordon, C., Wands, D., and Sasaki, M. (2002). Correlated Perturbations from Inflation and the Cosmic Microwave Background. *Physical Review Letters*, 88(21):211302–+.

[Antonucci, 1993] Antonucci, R. (1993). Unified models for active galactic nuclei and quasars. *ARA&A*, 31:473–521.

[Baccigalupi et al., 2000] Baccigalupi, C., Bedini, L., Burigana, C., De Zotti, G., Farusi, A., Maino, D., Maris, M., Perrotta, F., Salerno, E., Toffolatti, L., and Tonazzini, A. (2000). Neural networks and the separation of cosmic microwave background and astrophysical signals in sky maps. *MNRAS*, 318:769–780.

[Bahcall et al., 1999] Bahcall, N. A., Ostriker, J. P., Perlmutter, S., and Steinhardt, P. J. (1999). The Cosmic Triangle: Revealing the State of the Universe. *Science*, 284:1481–+.

[Banday et al., 1996] Banday, A. J., Gorski, K. M., Bennett, C. L., Hinshaw, G., Kogut, A., and Smoot, G. F. (1996). Noncosmological Signal Contributions to the COBE DMR 4 Year Sky Maps. *ApJ*, 468:L85+.

[Banday and Wolfendale, 1990] Banday, A. J. and Wolfendale, A. W. (1990). Fluctuations in the cosmic microwave background. *MNRAS*, 245:182–191.

[Banday and Wolfendale, 1991] Banday, A. J. and Wolfendale, A. W. (1991). Fluctuations in the galactic synchrotron radiation. I - Implications for searches for fluctuations of cosmological origin. *MNRAS*, 248:705–714.

[Bardeen et al., 1983] Bardeen, J. M., Steinhardt, P. J., and Turner, M. S. (1983). Spontaneous creation of almost scale-free density perturbations in an inflationary universe. *Physical Review D*, 28:679–693.

[Bardelli et al., 2000] Bardelli, S., Zucca, E., Zamorani, G., Moscardini, L., and Scaramella, R. (2000). A study of the core of the Shapley Concentration - IV. Distribution of intercluster galaxies and supercluster properties. *MNRAS*, 312:540–556.

[Barker et al., 2006] Barker, R. et al. (2006). High-significance Sunyaev-Zel'dovich measurement: Abell 1914 seen with the Arcminute Microkelvin Imager. *MNRAS*, 369:L1–L4.

[Bedini et al., 2005] Bedini, L., Herranz, D., Salerno, E., Baccigalupi, C., Kuruoğlu, E. E., and Tonazzini, A. (2005). Separation of correlated astrophysical sources using multiple-lag data covariance matrices. *EURASIP Journal on Applied Signal Processing*, 2005(15):2400–2412. doi:10.1155/ASP.2005.2400.

[Begelman, 1996] Begelman, M. C. (1996). *Baby Cygnus A's*, pages 209–+. Cygnus A – Studay of a Radio Galaxy.

[Belouchrani et al., 1997] Belouchrani, A., Abed-Meraim, K., Cardoso, J., and Moulines, E. (1997). A blind source separation technique using second orser statistics. *IEEE Transactions on Signal processing*, 45:434.

[Bennett et al., 2003] Bennett, C. L. et al. (2003). The WMAP First Year Source Catalog (WMAP1) (Bennett+, 2003). *VizieR Online Data Catalog*, 214:80097–+.

[Benoît et al., 2004] Benoît, A. et al. (2004). First detection of polarization of the submillimetre diffuse galactic dust emission by Archeops. *A&A*, 424:571–582.

[Bernardeau, 1997] Bernardeau, F. (1997). Weak lensing detection in CMB maps. *A&A*, 324:15–26.

[Bharadwaj and Pandey, 2004] Bharadwaj, S. and Pandey, B. (2004). Using the Filaments in the Las Campanas Redshift Survey to Test the ΛCDM Model. *ApJ*, 615:1–6.

[Birkinshaw and Gull, 1983] Birkinshaw, M. and Gull, S. F. (1983). A test for transverse motions of clusters of galaxies. *Nat*, 302:315–317.

[Blain et al., 2002] Blain, A. W., Smail, I., Ivison, R. J., Kneib, J.-P., and Frayer, D. T. (2002). Submillimeter galaxies. *Phys. Rep.*, 369:111–176.

[Bonaldi et al., 2006] Bonaldi, A., Bedini, L., Salerno, E., Baccigalupi, C., and de Zotti, G. (2006). Estimating the spectral indices of correlated astrophysical foregrounds by a second-order statistical approach. *MNRAS*, 373:271–279.

[Bonaldi et al., 2007a] Bonaldi, A., Ricciardi, S., Leach, S., Stivoli, F., Baccigalupi, C., and de Zotti, G. (2007a). WMAP 3-yr data with Correlated Component Analysis: anomalous emission and impact of component separation on the CMB power spectrum. *MNRAS*, 382:1791–1803.

[Bonaldi et al., 2007b] Bonaldi, A., Tormen, G., Dolag, K., and Moscardini, L. (2007b). Sunyaev-Zel'dovich profiles and scaling relations: modelling effects and observational biases. *MNRAS*, 378:1248–1258.

[Bond et al., 1980] Bond, J. R., Efstathiou, G., and Silk, J. (1980). Massive neutrinos and the large-scale structure of the universe. *Physical Review Letters*, 45:1980–1984.

[Bond et al., 1997] Bond, J. R., Efstathiou, G., and Tegmark, M. (1997). Forecasting cosmic parameter errors from microwave background anisotropy experiments. *MNRAS*, 291:L33–L41.

[Bond et al., 1996] Bond, J. R., Kofman, L., and Pogosyan, D. (1996). How filaments of galaxies are woven into the cosmic web. *Nat*, 380:603–+.

[Borgani, 2006] Borgani, S. (2006). Cosmology with clusters of galaxies. *preprint, astro-ph/0605575*.

[Bouchet and Gispert, 1999] Bouchet, F. R. and Gispert, R. (1999). Foregrounds and CMB experiments I. Semi-analytical estimates of contamination. *New Astronomy*, 4:443–479.

[Brandt et al., 1994] Brandt, W. N., Lawrence, C. R., Readhead, A. C. S., Pakianathan, J. N., and Fiola, T. M. (1994). Separation of foreground radiation from cosmic microwave background anisotropy using multifrequency measurements. *ApJ*, 424:1–21.

[Bregman et al., 2004] Bregman, J. N., Dupke, R. A., and Miller, E. D. (2004). Cosmic Filaments in Superclusters. *ApJ*, 614:31–36.

[Cen et al., 1993] Cen, R., Ostriker, J. P., and Peebles, P. J. E. (1993). A Hydrodynamic Approach to Cosmology: The Primeval Baryon Isocurvature Model. *ApJ*, 415:423–+.

[Cole and Efstathiou, 1989] Cole, S. and Efstathiou, G. (1989). Gravitational lensing of fluctuations in the microwave background radiation. *MNRAS*, 239:195–200.

[Davies et al., 2006] Davies, R. D., Dickinson, C., Banday, A. J., Jaffe, T. R., Górski, K. M., and Davis, R. J. (2006). A determination of the spectra of Galactic components observed by the Wilkinson Microwave Anisotropy Probe. *MNRAS*, 370:1125–1139.

[de Oliveira-Costa et al., 1997] de Oliveira-Costa, A., Kogut, A., Devlin, M. J., Netterfield, C. B., Page, L. A., and Wollack, E. J. (1997). Galactic Microwave Emission at Degree Angular Scales. *ApJ*, 482:L17.

[de Oliveira-Costa et al., 2004] de Oliveira-Costa, A., Tegmark, M., Davies, R. D., Gutiérrez, C. M., Lasenby, A. N., Rebolo, R., and Watson, R. A. (2004). The Quest for Microwave Foreground X. *ApJ*, 606:L89–L92.

[de Oliveira-Costa et al., 2002] de Oliveira-Costa, A., Tegmark, M., Finkbeiner, D. P., Davies, R. D., Gutierrez, C. M., Haffner, L. M., Jones, A. W., Lasenby, A. N., Rebolo, R., Reynolds, R. J., Tufte, S. L., and Watson, R. A. (2002). A New Spin on Galactic Dust. *ApJ*, 567:363–369.

[de Oliveira-Costa et al., 1999] de Oliveira-Costa, A., Tegmark, M., Gutierrez, C. M., Jones, A. W., Davies, R. D., Lasenby, A. N., Rebolo, R., and Watson, R. A. (1999). Cross-Correlation of Tenerife Data with Galactic Templates-Evidence for Spinning Dust? *ApJ*, 527:L9–L12.

[de Oliveira-Costa et al., 1998] de Oliveira-Costa, A., Tegmark, M., Page, L. A., and Boughn, S. P. (1998). Galactic Emission at 19 GHZ. *ApJ*, 509:L9–L12.

[de Zotti et al., 2005] de Zotti, G., Ricci, R., Mesa, D., Silva, L., Mazzotta, P., Toffolatti, L., and González-Nuevo, J. (2005). Predictions for high-frequency radio surveys of extragalactic sources. *A&A*, 431:893–903.

[de Zotti et al., 1999] de Zotti, G., Toffolatti, L., Argüeso, F., Davies, R. D., Mazzotta, P., Partridge, R. B., Smoot, G. F., and Vittorio, N. (1999). The Planck Surveyor Mission: Astrophysical Prospects. In Maiani, L., Melchiorri, F., and Vittorio, N., editors, *3K cosmology*, volume 476 of *American Institute of Physics Conference Series*, pages 204–+.

[Delabrouille and Cardoso, 2007] Delabrouille, J. and Cardoso, J. . (2007). Diffuse source separation in CMB observations. *ArXiv Astrophysics e-prints*.

[Dickinson et al., 2003] Dickinson, C., Davies, R. D., and Davis, R. J. (2003). Towards a free-free template for CMB foregrounds. *MNRAS*, 341:369–384.

[Dolag et al., 2006] Dolag, K., Meneghetti, M., Moscardini, L., Rasia, E., and Bonaldi, A. (2006). Simulating the physical properties of dark matter and gas inside the cosmic web. *MNRAS*, 370:656–672.

[Doroshkevich et al., 1980] Doroshkevich, A. G., Zeldovich, Y. B., Syunyaev, R. A., and Khlopov, M. Y. (1980). Astrophysical implications of the neutrino rest mass. II - The density-perturbation spectrum and small-scale fluctuations in the microwave background. III - Nonlinear growth of perturbations and the missing mass. *Pis ma Astronomicheskii Zhurnal*, 6:457–469.

[Draine and Lazarian, 1998] Draine, B. T. and Lazarian, A. (1998). Electric Dipole Radiation from Spinning Dust Grains. *ApJ*, 508:157–179.

[Dupac et al., 2003] Dupac, X., Bernard, J.-P., Boudet, N., Giard, M., Lamarre, J.-M., Mény, C., Pajot, F., Ristorcelli, I., Serra, G., Stepnik, B., and Torre, J.-P. (2003). Inverse temperature dependence of the dust submillimeter spectral index. *A&A*, 404:L11–L15.

[Ebeling et al., 2004] Ebeling, H., Barrett, E., and Donovan, D. (2004). Discovery of a Large-Scale Filament Connected to the Massive Galaxy Cluster MACS J0717.5+3745 at z=0.551,. *ApJ*, 609:L49–L52.

[Efstathiou and Bond, 1999] Efstathiou, G. and Bond, J. R. (1999). Cosmic confusion: degeneracies among cosmological parameters derived from measurements of microwave background anisotropies. *MNRAS*, 304:75–97.

[Eisenstein et al., 1999] Eisenstein, D. J., Hu, W., and Tegmark, M. (1999). Cosmic Complementarity: Joint Parameter Estimation from Cosmic Microwave Background Experiments and Redshift Surveys. *ApJ*, 518:2–23.

[Eke et al., 1996] Eke, V. R., Cole, S., and Frenk, C. S. (1996). Cluster evolution as a diagnostic for Omega. *MNRAS*, 282:263–280.

[Eriksen et al., 2006] Eriksen, H. K., Dickinson, C., Lawrence, C. R., Baccigalupi, C., Banday, A. J., Górski, K. M., Hansen, F. K., Lilje, P. B., Pierpaoli, E., Seiffert, M. D., Smith, K. M., and Vanderlinde, K. (2006). Cosmic Microwave Background Component Separation by Parameter Estimation. *ApJ*, 641:665–682.

[Falk et al., 1993] Falk, T., Rangarajan, R., and Srednicki, M. (1993). The angular dependence of the three-point correlation function of the cosmic microwave background radiation as predicted by inflationary cosmologies. *ApJ*, 403:L1–L3.

[Fanti et al., 1995] Fanti, C., Fanti, R., Dallacasa, D., Schilizzi, R. T., Spencer, R. E., and Stanghellini, C. (1995). Are compact steep-spectrum sources young? *A&A*, 302:317–+.

[Finkbeiner, 2003] Finkbeiner, D. P. (2003). A Full-Sky Hα Template for Microwave Foreground Prediction. *ApJ*, 146:407–415.

[Finkbeiner, 2004] Finkbeiner, D. P. (2004). Microwave Interstellar Medium Emission Observed by the Wilkinson Microwave Anisotropy Probe. *ApJ*, 614:186–193.

[Finkbeiner et al., 1999] Finkbeiner, D. P., Davis, M., and Schlegel, D. J. (1999). Extrapolation of Galactic Dust Emission at 100 Microns to Cosmic Microwave Background Radiation Frequencies Using FIRAS. *ApJ*, 524:867–886.

[Gangui et al., 1994] Gangui, A., Lucchin, F., Matarrese, S., and Mollerach, S. (1994). The three-point correlation function of the cosmic microwave background in inflationary models. *ApJ*, 430:447–457.

[Geller and Huchra, 1989] Geller, M. J. and Huchra, J. P. (1989). Mapping the universe. *Science*, 246:897–903.

[Giardino et al., 2002] Giardino, G., Banday, A. J., Górski, K. M., Bennett, K., Jonas, J. L., and Tauber, J. (2002). Towards a model of full-sky Galactic synchrotron intensity and linear polarisation: A re-analysis of the Parkes data. *A&A*, 387:82–97.

[González-Nuevo et al., 2006] González-Nuevo, J., Argüeso, F., López-Caniego, M., Toffolatti, L., Sanz, J. L., Vielva, P., and Herranz, D. (2006). The Mexican hat wavelet family: application to point-source detection in cosmic microwave background maps. *MNRAS*, 369:1603–1610.

[Górski et al., 2005] Górski, K. M., Hivon, E., Banday, A. J., Wandelt, B. D., Hansen, F. K., Reinecke, M., and Bartelmann, M. (2005). HEALPix: A Framework for High-Resolution Discretization and Fast Analysis of Data Distributed on the Sphere. *ApJ*, 622:759–771.

[Granato et al., 2000] Granato, G. L., Lacey, C. G., Silva, L., Bressan, A., Baugh, C. M., Cole, S., and Frenk, C. S. (2000). The Infrared Side of Galaxy Formation. I. The Local Universe in the Semianalytical Framework. *ApJ*, 542:710–730.

[Guth, 1981] Guth, A. H. (1981). Inflationary universe: A possible solution to the horizon and flatness problems. *Physical Review D*, 23:347–356.

[Guth and Pi, 1985] Guth, A. H. and Pi, S.-Y. (1985). Quantum mechanics of the scalar field in the new inflationary universe. *Physical Review D*, 32:1899–1920.

[Haslam et al., 1982] Haslam, C. G. T., Salter, C. J., Stoffel, H., and Wilson, W. E. (1982). A 408 MHz all-sky continuum survey. II - The atlas of contour maps. *A&AS*, 47:1–+.

[Herranz et al., 2002a] Herranz, D., Sanz, J. L., Barreiro, R. B., and Martínez-González, E. (2002a). Scale-adaptive Filters for the Detection/Separation of Compact Sources. *ApJ*, 580:610–625.

[Herranz et al., 2002b] Herranz, D., Sanz, J. L., Hobson, M. P., Barreiro, R. B., Diego, J. M., Martínez-González, E., and Lasenby, A. N. (2002b). Filtering techniques for the detection of Sunyaev-Zel'dovich clusters in multifrequency maps. *MNRAS*, 336:1057–1068.

[Hinshaw et al., 2006] Hinshaw, G. et al. (2006). Three-Year Wilkinson Microwave Anisotropy Probe (WMAP) Observations: Temperature Analysis. *submitted to ApJ(astro-ph/0603451)*.

[Hivon et al., 2002] Hivon, E., Górski, K. M., Netterfield, C. B., Crill, B. P., Prunet, S., and Hansen, F. (2002). MASTER of the Cosmic Microwave Background Anisotropy Power Spectrum: A Fast Method for Statistical Analysis of Large and Complex Cosmic Microwave Background Data Sets. *ApJ*, 567:2–17.

[Hobson et al., 1998] Hobson, M. P., Jones, A. W., Lasenby, A. N., and Bouchet, F. R. (1998). Foreground separation methods for satellite observations of the cosmic microwave background. *MNRAS*, 300:1–29.

[Hobson and Lasenby, 1998] Hobson, M. P. and Lasenby, A. N. (1998). The entropic prior for distributions with positive and negative values. *MNRAS*, 298:905–908.

[Howk and Savage, 1999] Howk, J. C. and Savage, B. D. (1999). Dust in the Ionized Medium of the Galaxy: GHRS Measurements of AL III and S III. *ApJ*, 517:746–766.

[Hu, 2001] Hu, W. (2001). Angular trispectrum of the cosmic microwave background. *Physical Review D*, 64(8):083005–+.

[Hu and Dodelson, 2002] Hu, W. and Dodelson, S. (2002). Cosmic Microwave Background Anisotropies. *ARA&A*, 40:171–216.

[Hu and White, 1997] Hu, W. and White, M. (1997). The Damping Tail of Cosmic Microwave Background Anisotropies. *ApJ*, 479:568–+.

[Hummel et al., 1991] Hummel, E., Dahlem, M., van der Hulst, J. M., and Sukumar, S. (1991). The large-scale radio continuum structure of the edge-on spiral galaxy NGC 891. *A&A*, 246:10–20.

[Hyvarinen, 1999] Hyvarinen, A. (1999). Fast and Robust Fixed-Point Algorithms for Independent Component Analysis. *IEEE Transactions on Neural Networks*, 10:626–634.

[Inoue, 2001] Inoue, K. T. (2001). Exploring Topology of the Universe in the Cosmic Microwave Background. *astro-ph/0103158*.

[Knox, 1995] Knox, L. (1995). Determination of inflationary observables by cosmic microwave background anisotropy experiments. *Physical Review D*, 52:4307–4318.

[Kogut, 1999] Kogut, A. (1999). Anomalous Microwave Emission. In de Oliveira-Costa, A. and Tegmark, M., editors, *Microwave Foregrounds*, volume 181 of *Astronomical Society of the Pacific Conference Series*, pages 91–+.

[Kogut et al., 1996] Kogut, A., Banday, A. J., Bennett, C. L., Gorski, K. M., Hinshaw, G., Smoot, G. F., and Wright, E. I. (1996). Microwave Emission at High Galactic Latitudes in the Four-Year DMR Sky Maps. *ApJ*, 464:L5+.

[Komatsu, 2003] Komatsu, E. (2003). Wilkinson Microwave Anisotropy Probe constraints on non-Gaussianity. *New Astronomy Review*, 47:797–803.

[Lagache, 2003] Lagache, G. (2003). The large-scale anomalous microwave emission revisited by WMAP. *A&A*, 405:813–819.

[Leitch et al., 1997] Leitch, E. M., Readhead, A. C. S., Pearson, T. J., and Myers, S. T. (1997). An Anomalous Component of Galactic Emission. *ApJ*, 486:L23+.

[Liguori et al., 2007] Liguori, M., Yadav, A., Hansen, F. K., Komatsu, E., Matarrese, S., and Wandelt, B. (2007). Temperature and Polarization CMB Maps from Primordial non-Gaussianities of the Local Type. *ArXiv e-prints*, 708.

[López-Caniego et al., 2006] López-Caniego, M., Herranz, D., González-Nuevo, J., Sanz, J. L., Barreiro, R. B., Vielva, P., Argüeso, F., and Toffolatti, L. (2006). Comparison of filters for the detection of point sources in Planck simulations. *MNRAS*, 370:2047–2063.

[Magliocchetti et al., 2000] Magliocchetti, M., Maddox, S. J., Wall, J. V., Benn, C. R., and Cotter, G. (2000). The redshift distribution of FIRST radio sources at 1mJy. *MNRAS*, 318:1047–1067.

[Maino et al., 2002] Maino, D., Farusi, A., Baccigalupi, C., Perrotta, F., Banday, A. J., Bedini, L., Burigana, C., De Zotti, G., Górski, K. M., and Salerno, E. (2002). All-sky astrophysical component separation with Fast Independent Component Analysis (FASTICA). *MNRAS*, 334:53–68.

[Massardi, 2006] Massardi, M. (2006). Realistic point source maps at Planck frequencies. In *CMB and Physics of the Early Universe*.

[Mather et al., 1999] Mather, J. C., Fixsen, D. J., Shafer, R. A., Mosier, C., and Wilkinson, D. T. (1999). Calibrator Design for the COBE Far-Infrared Absolute Spectrophotometer (FIRAS). *ApJ*, 512:511–520.

[McCullough et al., 1999] McCullough, P. R., Gaustad, J. E., Rosing, W., and Van Buren, D. (1999). Implications of Hα Observations for Studies of the CMB. In de Oliveira-Costa, A. and Tegmark, M., editors, *Microwave Foregrounds*, volume 181 of *Astronomical Society of the Pacific Conference Series*, pages 253–+.

[Melin et al., 2006] Melin, J.-B., Bartlett, J. G., and Delabrouille, J. (2006). Catalog extraction in SZ cluster surveys: a matched filter approach. *A&A*, 459:341–352.

[Metcalf and Silk, 1997] Metcalf, R. B. and Silk, J. (1997). Gravitational Magnification of the Cosmic Microwave Background. *ApJ*, 489:1–+.

[Moscardini et al., 1998] Moscardini, L., Coles, P., Lucchin, F., and Matarrese, S. (1998). Modelling galaxy clustering at high redshift. *MNRAS*, 299:95–110.

[Mukherjee et al., 2001] Mukherjee, P., Jones, A. W., Kneissl, R., and Lasenby, A. N. (2001). On dust-correlated Galactic emission in the Tenerife data. *MNRAS*, 320:224–234.

[Nagai, 2006] Nagai, D. (2006). The Impact of Galaxy Formation on the Sunyaev-Zel'dovich Effect of Galaxy Clusters. *ApJ*, 650:538–549.

[Page et al., 2006] Page, L. et al. (2006). Three Year Wilkinson Microwave Anisotropy Probe (WMAP) Observations: Polarization Analysis. *submitted to ApJ(astro-ph/0603450)*.

[Paladini et al., 2005] Paladini, R., De Zotti, G., Davies, R. D., and Giard, M. (2005). Analysis of the thin layer of Galactic warm ionized gas in the range. *MNRAS*, 360:1545–1552.

[Pandey and Bharadwaj, 2005] Pandey, B. and Bharadwaj, S. (2005). A two-dimensional analysis of percolation and filamentarity in the Sloan Digital Sky Survey Data Release One. *MNRAS*, 357:1068–1076.

[Peebles, 1979a] Peebles, P. J. E. (1979a). The mean mass density estimated from the Kirshner, Oemler, Schechter galaxy redshift sample. *AJ*, 84:730–734.

[Peebles, 1979b] Peebles, P. J. E. (1979b). The problems of cosmology. In *Scientific research with the Space Telescope (IAU Colloq. No. 54), p. 295 - 312*, pages 295–312.

[Pimbblet et al., 2004] Pimbblet, K. A., Drinkwater, M. J., and Hawkrigg, M. C. (2004). Intercluster filaments of galaxies programme: abundance and distribution of filaments in the 2dFGRS catalogue. *MNRAS*, 354:L61–L65.

[Plionis et al., 2003] Plionis, M., Benoist, C., Maurogordato, S., Ferrari, C., and Basilakos, S. (2003). Galaxy Alignments as a Probe of the Dynamical State of Clusters. *ApJ*, 594:144–153.

[Polatidis et al., 1999] Polatidis, A., Wilkinson, P. N., Xu, W., Readhead, A. C. S., Pearson, T. J., Taylor, G. B., and Vermeulen, R. C. (1999). Compact Symmetric Objects in a complete flux density limited sample. *New Astronomy Review*, 43:657–661.

[Polnarev, 1985] Polnarev, A. G. (1985). Polarization and Anisotropy Induced in the Microwave Background by Cosmological Gravitational Waves. *Soviet Astronomy*, 29:607–+.

[Ponthieu et al., 2005] Ponthieu, N. et al. (2005). Temperature and polarization angular power spectra of Galactic dust radiation at 353 GHz as measured by Archeops. *A&A*, 444:327–336.

[Porter and Raychaudhury, 2005] Porter, S. C. and Raychaudhury, S. (2005). The Pisces-Cetus supercluster: a remarkable filament of galaxies in the 2dF Galaxy Redshift and Sloan Digital Sky surveys. *MNRAS*, 364:1387–1396.

[Press and Schechter, 1974] Press, W. H. and Schechter, P. (1974). Formation of Galaxies and Clusters of Galaxies by Self-Similar Gravitational Condensation. *ApJ*, 187:425–438.

[Readhead et al., 1996] Readhead, A. C. S., Taylor, G. B., Xu, W., Pearson, T. J., Wilkinson, P. N., and Polatidis, A. G. (1996). The Statistics and Ages of Compact Symmetric Objects. *ApJ*, 460:612–+.

[Rees and Sciama, 1968] Rees, M. J. and Sciama, D. W. (1968). Larger scale Density Inhomogeneities in the Universe. *Nat*, 217:511–+.

[Reich and Reich, 1988] Reich, P. and Reich, W. (1988). A map of spectral indices of the Galactic radio continuum emission between 408 MHz and 1420 MHz for the entire northern sky. *A&AS*, 74:7–20.

[Rosati et al., 2002] Rosati, P., Borgani, S., and Norman, C. (2002). The Evolution of X-ray Clusters of Galaxies. *ARA&A*, 40:539–577.

[Sachs and Wolfe, 1967] Sachs, R. K. and Wolfe, A. M. (1967). Perturbations of a Cosmological Model and Angular Variations of the Microwave Background. *ApJ*, 147:73–+.

[Sanz et al., 2001] Sanz, J. L., Herranz, D., and Martínez-Gónzalez, E. (2001). Optimal Detection of Sources on a Homogeneous and Isotropic Background. *ApJ*, 552:484–492.

[Schlegel et al., 1998] Schlegel, D. J., Finkbeiner, D. P., and Davis, M. (1998). Maps of Dust Infrared Emission for Use in Estimation of Reddening and Cosmic Microwave Background Radiation Foregrounds. *ApJ*, 500:525–+.

[Seljak, 1996] Seljak, U. (1996). Rees-Sciama Effect in a Cold Dark Matter Universe. *ApJ*, 460:549–+.

[Silk, 1968] Silk, J. (1968). Cosmic Black-Body Radiation and Galaxy Formation. *ApJ*, 151:459–+.

[Skilling, 1989] Skilling, J., editor (1989). *Maximum entropy and bayesian methods : 8 : 1988*.

[Smoot, 1998] Smoot, G. F. (1998). Galactic Free-free and H-alpha Emission. *ArXiv Astrophysics e-prints*.

[Snellen et al., 2000] Snellen, I. A. G., Schilizzi, R. T., Miley, G. K., de Bruyn, A. G., Bremer, M. N., and Röttgering, H. J. A. (2000). On the evolution of young radio-loud AGN. *MNRAS*, 319:445–456.

[Spergel et al., 2006] Spergel, D. N. et al. (2006). Wilkinson Microwave Anisotropy Probe (WMAP) Three Year Results: Implications for Cosmology. *submitted to ApJ(astro-ph/0603449)*.

[Stolyarov et al., 2002] Stolyarov, V., Hobson, M. P., Ashdown, M. A. J., and Lasenby, A. N. (2002). All-sky component separation for the Planck mission. *MNRAS*, 336:97–111.

[Stolyarov et al., 2005] Stolyarov, V., Hobson, M. P., Lasenby, A. N., and Barreiro, R. B. (2005). All-sky component separation in the presence of anisotropic noise and dust temperature variations. *MNRAS*, 357:145–155.

[Sunyaev and Zeldovich, 1972] Sunyaev, R. A. and Zeldovich, Y. B. (1972). The Observations of Relic Radiation as a Test of the Nature of X-Ray Radiation from the Clusters of Galaxies. *Comments on Astrophysics and Space Physics*, 4:173–+.

[Takada and Futamase, 2001] Takada, M. and Futamase, T. (2001). Detectability of the Gravitational Lensing Effect on the Two-Point Correlation Function of Hot Spots in Cosmic Microwave Background Maps. *ApJ*, 546:620–634.

[Taylor et al., 2000] Taylor, G. B., Marr, J. M., Pearson, T. J., and Readhead, A. C. S. (2000). Kinematic Age Estimates for Four Compact Symmetric Objects from the Pearson-Readhead Survey. *ApJ*, 541:112–119.

[Tegmark and de Oliveira-Costa, 1998] Tegmark, M. and de Oliveira-Costa, A. (1998). Removing Point Sources from Cosmic Microwave Background Maps. *ApJ*, 500:L83+.

[Tegmark and Efstathiou, 1996] Tegmark, M. and Efstathiou, G. (1996). A method for subtracting foregrounds from multifrequency CMB sky maps**. *MNRAS*, 281:1297–1314.

[Tegmark et al., 2000] Tegmark, M., Eisenstein, D. J., Hu, W., and de Oliveira-Costa, A. (2000). Foregrounds and Forecasts for the Cosmic Microwave Background. *ApJ*, 530:133–165.

[The Planck Collaboration, 2005] The Planck Collaboration (2005). The Scientific Programme of Planck. *ESA-SCI(2005)1 (astro-ph/0604069)*.

[Tschager et al., 2000] Tschager, W., Schilizzi, R. T., Röttgering, H. J. A., Snellen, I. A. G., and Miley, G. K. (2000). The GHz-peaked spectrum radio galaxy 2021+614: detection of slow motion in a compact symmetric object. *A&A*, 360:887–895.

[Urry and Padovani, 1995] Urry, C. M. and Padovani, P. (1995). Unified Schemes for Radio-Loud Active Galactic Nuclei. *PASP*, 107:803–+.

[Valls-Gabaud, 1998] Valls-Gabaud, D. (1998). Cosmological applications of H-alpha surveys. *Publications of the Astronomical Society of Australia*, 15:111–17.

[Verde et al., 2000] Verde, L., Wang, L., Heavens, A. F., and Kamionkowski, M. (2000). Large-scale structure, the cosmic microwave background and primordial non-Gaussianity. *MNRAS*, 313:141–147.

[Viana and Liddle, 1996] Viana, P. T. P. and Liddle, A. R. (1996). The cluster abundance in flat and open cosmologies. *MNRAS*, 281:323–+.

[Voit, 2005] Voit, G. M. (2005). Tracing cosmic evolution with clusters of galaxies. *Reviews of Modern Physics*, 77:207–258.

[Watson et al., 2005] Watson, R. A., Rebolo, R., Rubiño-Martín, J. A., Hildebrandt, S., Gutiérrez, C. M., Fernández-Cerezo, S., Hoyland, R. J., and Battistelli, E. S. (2005). Detection of Anomalous Microwave Emission in the Perseus Molecular Cloud with the COSMOSOMAS Experiment. *ApJ*, 624:L89–L92.

[White et al., 2002] White, M., Hernquist, L., and Springel, V. (2002). Simulating the Sunyaev-Zeldovich Effect(s): Including Radiative Cooling and Energy Injection by Galactic Winds. *ApJ*, 579:16–22.

[White et al., 1993] White, S. D. M., Efstathiou, G., and Frenk, C. S. (1993). The amplitude of mass fluctuations in the universe. *MNRAS*, 262:1023–1028.

[Winitzki and Kosowsky, 1998] Winitzki, S. and Kosowsky, A. (1998). Minkowski functional description of microwave background Gaussianity. *New Astronomy*, 3:75–100.

[Zaldarriaga, 2000] Zaldarriaga, M. (2000). Lensing of the CMB: Non-Gaussian aspects. *Physical Review D*, 62(6):063510–+.

[Zaldarriaga et al., 1997] Zaldarriaga, M., Spergel, D. N., and Seljak, U. (1997). Microwave Background Constraints on Cosmological Parameters. *ApJ*, 488:1–+.

[Zavarise, 2007] Zavarise, P. (2007). Component separation for cosmic microwave background experiments. Master's thesis, University of Padova, Italy.

Appendix A

Useful units and conversions

Here we present the definitions and conversion factors between the units we used throughout this Thesis. The constants used in the conversions are:

$$\begin{aligned} h &= 6.626176 \cdot 10^{-27}\ \mathrm{erg\,s} \\ k_B &= 1.380662 \cdot 10^{-16}\ \mathrm{erg/K} \\ c &= 2.99792458 \cdot 10^{10}\ \mathrm{cm/s} \\ T_{CMB} &= 2.726\ \mathrm{K} \end{aligned}$$

In the microwave range, the unit of flux which is commonly used is the Jansky (Jy):

$$1\mathrm{Jy} = 10^{-23}\mathrm{erg\,s^{-1}cm^{-2}Hz^{-1}}. \tag{A.1}$$

A generic source fluctuation is commonly expressed in units of brightness, i.e. flux per unit area. Thus, a common unit of brightness in the CMB range is Jy/sterad (or multiples). An alternative unit is antenna temperature. The conversion to brightness is:

$$1\mathrm{Jy/sterad} = 2\mathrm{k_B}\left(\frac{\nu}{\mathrm{c}}\right)^2 \cdot 10^{23}\,\mathrm{K\,(antenna)}, \tag{A.2}$$

with the frequency ν in Hz.

CMB fluctuations are often expressed in thermodynamic temperature, which is the temperature of a blackbody which emits a certain flux at a given frequency. This unit is useful as the frequency spectrum of CMB fluctuations is a blackbody, so a certain fluctuation has the same thermodynamic temperature at all frequencies. The conversion to antenna temperature is:

$$1\mathrm{K\,(antenna)} = \left(\frac{\mathrm{h}\nu}{\mathrm{kT_{CMB}}}\right)^2 \frac{\exp(\mathrm{h}\nu/\mathrm{kT_{CMB}})}{[\exp(\mathrm{h}\nu/\mathrm{kT_{CMB}})-1]^2}\,\mathrm{K\,(thermodynamic)}. \tag{A.3}$$

In table A.1 we report the conversions for the Planck channels. The conversion from brightness (Jy/sterad) to flux (Jy) is obtained multiplying for the solid angle of the experimental beam at that frequency (For a Gaussian beam of FWHM= Θ rad, the solid angle is $\Omega = \pi(\Theta/2)^2/\ln 2$ sterad).

Table A.1: Antenna temperature, brightness and flux at the PLANCK channels corresponding to a fluctuation of 1K in thermodynamic temperature.

Frequency [GHz]	Antenna temperature [K]	Brightness [MJy/sterad]	Flux [10^3Jy]
30	0.97707402	27.017549	2.8209186
44	0.95145921	56.594141	3.1254365
70	0.88249613	132.85712	2.4966498
100	0.77729534	238.81524	2.0664550
143	0.60483320	379.99996	1.8366099
217	0.33441687	483.81974	1.1596857
353	0.077544524	296.87693	0.71159548
545	0.0062673491	57.194317	0.13709121
857	6.3773948e-05	1.4390665	0.0034493527